Contributions to Geophysics and Geodesy Vol. 50/2, 2020 (161–199)

# Minerals and ore deposits exploration using meta-heuristic based optimization on magnetic data

Mohamed GOBASHY[1], Maha ABDELAZEEM[2,*], Mohamed ABDRABOU[1]

[1] Cairo University, Faculty of Science, Geophysics Department, Giza, Egypt

[2] National Research Institute of Astronomy and Geophysics (NRIAG), Helwan, Cairo, Egypt

**Abstract:** The difficulties in unravelling the tectonic structures, in some cases, prevent the understanding of the ore bodies' geometry, leading to mistakes in mineral exploration, mine planning, evaluation of ore deposits, and even mineral exploitation. For that reason, many geophysical techniques are introduced to reveal the type, dimension, and geometry of these structures. Among them, electric methods, self-potential, electromagnetic, magnetic and gravity methods. Global meta-heuristic technique using Whale Optimization Algorithm (WOA) has been utilized for assessing model parameters from magnetic anomalies due to a thin dike, a dipping dike, and a vertical fault like/shear zone geological structure. These structures are commonly associated with mineralization. This modern algorithm was firstly applied on a free-noise synthetic data and to a noisy data with three different levels of random noise to simulate natural and artificial anomaly disturbances. Good results obtained through the inversion of such synthetic examples prove the validity and applicability of our algorithm. Thereafter, the method is applied to real case studies taken from different ore mineralization resembling different geologic conditions. Data are taken from Canada, United States, Sweden, Peru, India, and Australia. The obtained results revealed good correlation with previous interpretations of these real field examples.

**Key words:** magnetic anomaly, ore deposits, whale algorithm, artificial intelligence, inversion, mineralization

## 1. Introduction

Magnetic prospecting method has been used to investigate a broad diversity of geological structures varying in size and depth from shallow ore bodies to deep basement structures. For detecting areas of large thickness of high potentially oil-bearing sedimentary rocks in oil exploration and, for mapping

*corresponding author: e-mail: maazeem03@hotmail.com

doi: 10.31577/congeo.2020.50.2.1

and outlining ore deposits (e.g., iron, and copper) in ore prospection, magnetic survey is still in use as a powerful geophysical technique in tracking mineralized zones. The general target of the magnetic surveys is, consequently, to investigate minerals or rocks having contrast in the magnetic properties (i.e., magnetic susceptibility) with the surroundings to discover them as anomalies in the magnetic field intensity of the earth. Occasionally, a single magnetic anomaly can be isolated from the regional trend and dealt with as an individual magnetized source. However, in such cases, the interpretation of magnetic data is normally exposed to ambiguity. Variant geometric shapes below can give similar magnetic response at the earth's surface. A single solution, although, can be obtained immediately from magnetic data if the shape of the buried body is known and a constant contrast in the magnetic susceptibility is present. This point was numerically confirmed through numerous researchers by categorizing nearly all of the magnetic source bodies in exploration studies into four simple stationary shapes: the horizontal cylinder, the sphere, the geologic contact and the thin sheet (*Nettleton, 1976; Abdelazeem, 2001; Li, 2003*). These simple geologic sources are frequently acceptable approximations to familiar geologic bodies included in the process of interpretation of magnetic field data quantitatively.

For these kinds of structures, numerous methods have been developed and utilized for explanation of magnetic field anomalies resulted from simple shaped bodies aiming to estimate the depth to the subsurface body, location of body, the amplitude coefficient, and the index parameter from magnetic anomalies. Among these techniques for example are: monograms (*Prakasa Rao et al., 1986*), theoretical matching standard curves (*Gay, 1963, 1965; Atchuta Rao and Ram Babu,1983*), characteristic curves methods (*Bruckshaw and Kunaratnam, 1963; Grant and West, 1965; Koulomzine et al., 1970; Telford et al., 1976; Rao and Murthy, 1978*), correlation factors between successive least-squares residual anomalies (*Abdelrahman et al., 1989*), Hilbert transforms (*Mohan et al., 1982*), Euler deconvolution approach (*Reid et al., 1990; Gerovska and Araúzo-Bravo, 2003; Salem and Ravat, 2003; Pasteka, 2006*) analytic signal derivatives (*Salem, 2005*), Werner deconvolution approach (*Hartman et al., 1971;* and *Ku and Sharp, 1983*), and fair function minimization (*Tlas and Asfahani, 2011*). Global optimization techniques like very fast simulated annealing (VFSA), simulated

annealing, higher-order horizontal derivative methods and particle swarm optimization (PSO) (*Sweilam et al., 2007, 2008; Göktürkler and Balkaya, 2012; Biswas and Sharma, 2014a,b; Biswas, 2015; Biswas and Acharya, 2016; Ekinci, 2016; Singh and Biswas, 2016*) have been successfully used to obtain model parameters from nonlinear inversion problems.

Though, mainly, the assessment of model unknowns, namely amplitude coefficient, depth, dip angle of the dike and effective magnetization angle of the subsurface model (e.g. thin dike, dipping dike and vertical fault), is achieved by inversion approaches as referred above. Consequently, the precision of the outcomes acquired by the above- referred techniques depends on the accuracy by which the anomaly can be isolated from the measured magnetic anomaly.

Whale Optimization Algorithm (WOA) has been recently used in solving the ill-posed inverse problem in geophysics. WOA inversion has been utilized to invert Self-Potential anomalies due to 2D inclined sheet and simple geometric bodies like (sphere, vertical cylinder, and horizontal cylinder) (*Gobashy et al., 2020; Abdelazeem et al., 2019*).

In this work, a rapid and effective modeling technique based on the Whale Optimization Algorithm (WOA) global meta-heuristic algorithm (*Mirjalili and Lewis, 2016*) was applied for inverting the highly ill-posed magnetic field due to thin dike, dipping dike and vertical fault. For a thin dike model, this method was applied to solve for four parameters, namely the depth ($h$), effective magnetization intensity ($A_e$), horizontal location ($x_0$), and effective magnetization inclination of the dike ($\theta$); for a dipping dike model, it was applied to extract five unknowns, namely the depth ($h$), half-width ($b$), intensity of magnetization ($I$), inclination of the magnetic vector ($\psi$), and dip angle of the dike ($\theta$), and for a vertical fault it was applied to estimate five unknowns, namely the effective magnetization intensity ($K$), horizontal location ($x_0$), effective magnetization inclination ($\theta$), depth to the upper edge ($z$), and depth to the lower edge of the fault ($z_b$).

The accuracy of this meta-heuristic optimization algorithm is practically examined via synthetic examples, using simulated data created from three models (i.e. thin dike, dipping dike, and vertical fault) with three different levels of random noise. As it is theoretically proved, the suggested algorithm is afterwards applied to real magnetic profiles over mineralized zones resembling different geologic structures and geometries taken from Canada,

United States, Sweden, Peru, India, and Australia. There is an excellent correlation between the outcomes attained from the suggested algorithm and those obtained by other techniques.

## 2. Methodology

### 2.1. Magnetic problem formulation

#### 2.1.1. Thin dike-like structure

For a magnetic effect $F(x)$ generated by a thin dike model of infinite depth extent (Fig. 1) that may be either in total, vertical, or horizontal magnetic components, the general formula is given by (*Gay, 1963*) as:

$$F(x) = A_e \frac{h\cos\theta + (x - x_0)\sin\theta}{(x - x_0)^2 + h^2}\,, \tag{1}$$

where $A_e = K{\cdot}\, h$, and $K$ refers to the effective magnetization intensity or the amplitude coefficient, $h$ defines the depth to the top of the buried thin

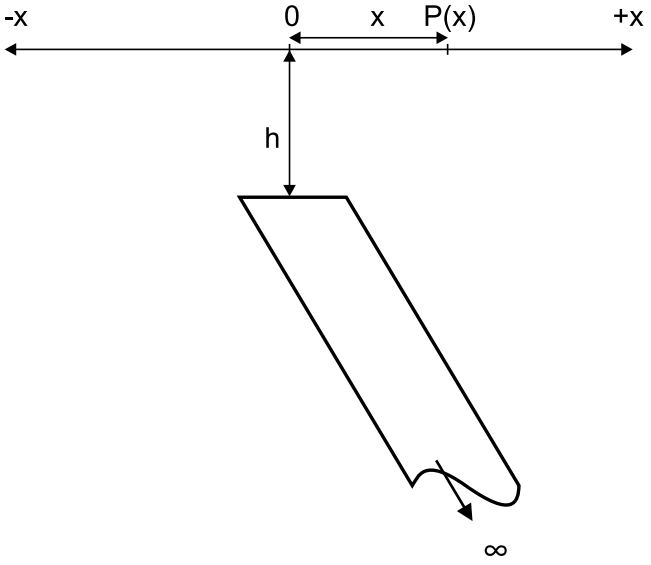


Fig. 1. Cross-sectional view of a two-dimensional thin dike model (*Tlas and Asfahani, 2011*).

dike-like structure, $x$ is the horizontal coordinate along the profile, $\theta$ refers to the index parameter or the effective magnetization angle, and $x_0$ defines the true origin of the observed magnetic anomaly.

### 2.1.2. Dipping dike-like structure

The vertical magnetic anomaly $V(x)$ generated from an infinitely dipping dike model with a uniform magnetization (Fig. 2) is expressed by (*Grant and West, 1965*) as:

$$V(x) = 2I \sin\theta \left[\cos\psi \left(\tan^{-1}\frac{x+b}{h} - \tan^{-1}\frac{x-b}{h}\right) + \right. \\ \left. + \frac{1}{2}\sin\psi \left(\ln\frac{h^2+(x+b)^2}{h^2+(x-b)^2}\right)\right], \tag{2}$$

where $I = k \cdot F_e$, $I$ is the intensity of magnetization (nT), $k$ refers to the magnetic susceptibility contrast, $F_e$ is the vertical component of the local ambient field (nT), $b$ is the half width of the dike (m), $h$ defines depth of the upper surface (m), $\theta$ refers to the dip angle of the dike (degree), and $\psi$ is the inclination of the magnetization vector (degree).

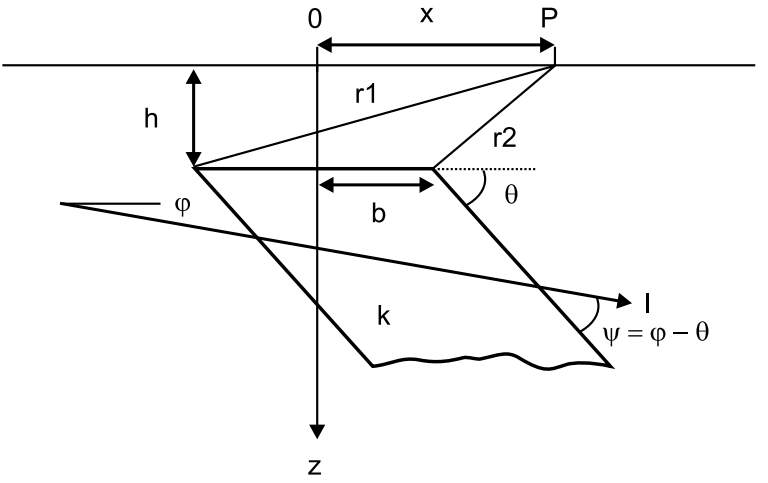


Fig. 2. Geometry of a thick dipping dike model.

### 2.1.3. Vertical fault model

The magnetic effect $F(x)$ of a two-dimensional magnetized fault model that could be in total, horizontal or vertical field at a discrete point $\boldsymbol{x_i}$ along the horizontal coordinate $(x)$ (Fig. 3) is expressed by the following equation (*Atchuta Rao and Ram Babu, 1983*, and *Tlas and Asfahani, 2011*) as:

$$F(x) = k\frac{z}{z_b - z}\left[\cos\theta\left(\ln\left|\sin\left(\tan^{-1}\frac{x_i - x_0}{z}\right)\right| - \ln\left|\sin\left(\tan^{-1}\frac{x_i - x_0}{z_b}\right)\right|\right) + \sin\theta\left(\tan^{-1}\frac{x_i - x_0}{z} - \tan^{-1}\frac{x_i - x_0}{z_b}\right)\right], \quad (i = 1, 2, 3, ...., N) \tag{3}$$

where $\theta$ refers to the effective magnetization inclination or (the index parameter), $k$ is the effective magnetization intensity or (the amplitude coefficient), $z$ is the depth to the upper edge of the fault directly underneath the horizontal position $(x_0)$ of the edge of the fault, $x_i$ is an individual point through the horizontal coordinate location $(x)$ where the measured magnetic anomaly is located, and $z_b$ defines the depth to the lower edge of the fault as shown in (Fig. 3).

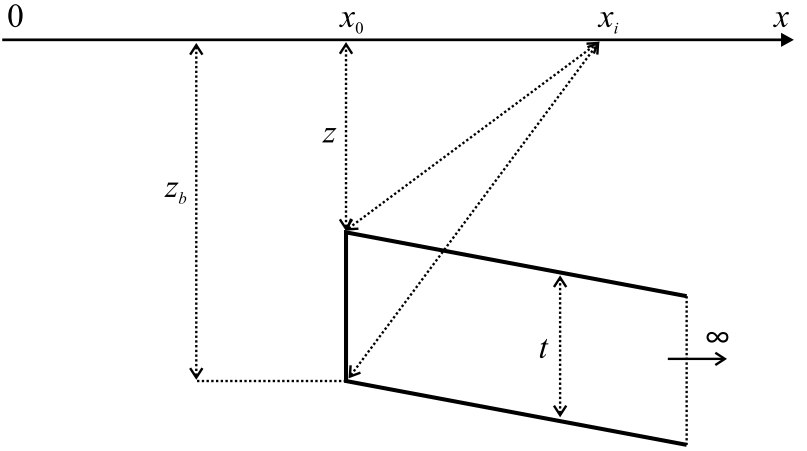


Fig. 3. Cross-sectional view of a two-dimensional vertical fault model (*Tlas and Asfahani, 2011*).

### 2.2. Inversion

Several global optimization techniques have been evolved in the past decades based upon various important concepts as mentioned above. The principal goal of geophysical inversion is to optimize a cost function or an objective function in the modeling of geophysical data. Numerous optimization approaches like genetic algorithms (GA), very fast simulated annealing (VFSA), particle swarm optimization (PSO), artificial neural networks (ANN), differential evolution (DE), black hole algorithm (BHA) and Simplex algorithm (*Abdelazeem and Gobashy, 2006; Biswas and Sharma, 2015, 2016; Monteiro Santos, 2010; El-Kaliouby and Al-Garni, 2009; Li and Yin, 2012; Sungkono and Desa Warnana, 2018; Abdelrahman et al., 2019*) were successfully utilized to minimize an objective function of observed geophysical data to find model parameters (i.e. various geophysical information).

Whale Optimization Algorithm (WOA) is a recent optimization algorithm which was first proposed by (*Mirjalili and Lewis, 2016*). WOA was inspired from nature that imitates the humpback whale behavior. Unlike genetic algorithm (GA) and particle swarm optimization (PSO), the WOA is very fast, simple in its concept, reliable, does not need adjusting or tuning its parameters, and unlike modular neural network (MNN) technique (*El-Kaliouby and Al-Garni, 2009*), it does not require training which it takes longer time and represents an important step in neural network.

Briefly, WOA implements the following strategies used by the humpback whales such as bubble-net attacking and searching for the prey.

1. Bubble-net attacking:

When two or more whales swim in a shrinking ring or circle, bubbles are created to encircle the prey along a spiral path. Some search agents (whales) are pushing the prey to the surface while the others lead the prey to the net. The positions of the search agents are updated according to the position of the best search agent. In a mathematical form, this mechanism of encircling the prey can be expressed as follows (*Abdel-Basset et al., 2018*):

$$D = |C \cdot \omega^* - x^t| \,, \tag{4}$$

$$x^{t+1} = \omega^* - A \cdot D \,, \tag{5}$$

$$A = 2a \cdot r - a\,, \tag{6}$$

$$C = 2 \cdot r\,, \tag{7}$$

where, $D$ is the distance between the current search agent $x^t$ and the best search agent $\omega^*$ so far at $t$ iteration. $A$ and $C$ are coefficient vectors, $A$ is a random value in the range $[-a,\, a]$, $x^t$ is the position vector, $||$ is the absolute value, and $\cdot$ is an element-by-element multiplication. It is worth mentioning here that $\omega^*$ should be updated in each iteration if there is a better solution. $r$ is a random number in [0, 1]. $a$ is linearly decreased from 2 to 0 over the course of iterations (in both exploration and exploitation phases).

The value of $A$ decreases from 2 to 0 during iterations and $C$ is a coefficient. Different places around the best agent can be achieved with respect to the current position by adjusting the value of $A$ and $C$ vectors. The spiral shaped path's behavior can be given as (*Abdel-Basset et al., 2018*):

$$x^{t+1} = D' \cdot \mathrm{e}^{bi} \cdot \cos(2\pi l) + \omega^*\,, \tag{8}$$

$$D' = |\omega^* - x^t|\,, \tag{9}$$

where, $D'$ is the absolute value for the distance between $x^t$ and $\omega^*$. $b$ defines the shape of the logarithmic spiral, $l$ is a random value $\in [-1,\, 1]$. WOA implements the two behaviors of bubble-net attacking encircling: the prey circle and the spiral movement with equal probabilities as follows:

$$x^{t+1} = \begin{cases} \omega^* - A \cdot D & p < 0.5\,, \\ D' \cdot \mathrm{e}^{bi} \cdot \cos(2\pi l) + \omega^* & p \geq 0.5\,. \end{cases} \tag{10}$$

2. Searching for the prey:

WOA makes a tradeoff between the exploration, which can be done by selecting a random search agent $x_{rand}$, and the exploitation, which is done by selecting the best search agent:

$$D = |C \cdot x_{rand} - x^t|\,, \tag{11}$$

$$x^{t+1} = x_{rand} - A \cdot D\,. \tag{12}$$

A detailed explanation and more discussion of the stability of WOA can be found in *Mirjalili and Lewis (2016); Abdel-Basset et al. (2018); Gobashy et al. (2020); Abdelazeem et al. (2019).* Fig. 4a shows a flowchart for the WOA heuristic algorithm, Fig. 4b shows the Bubble-net search mechanism,

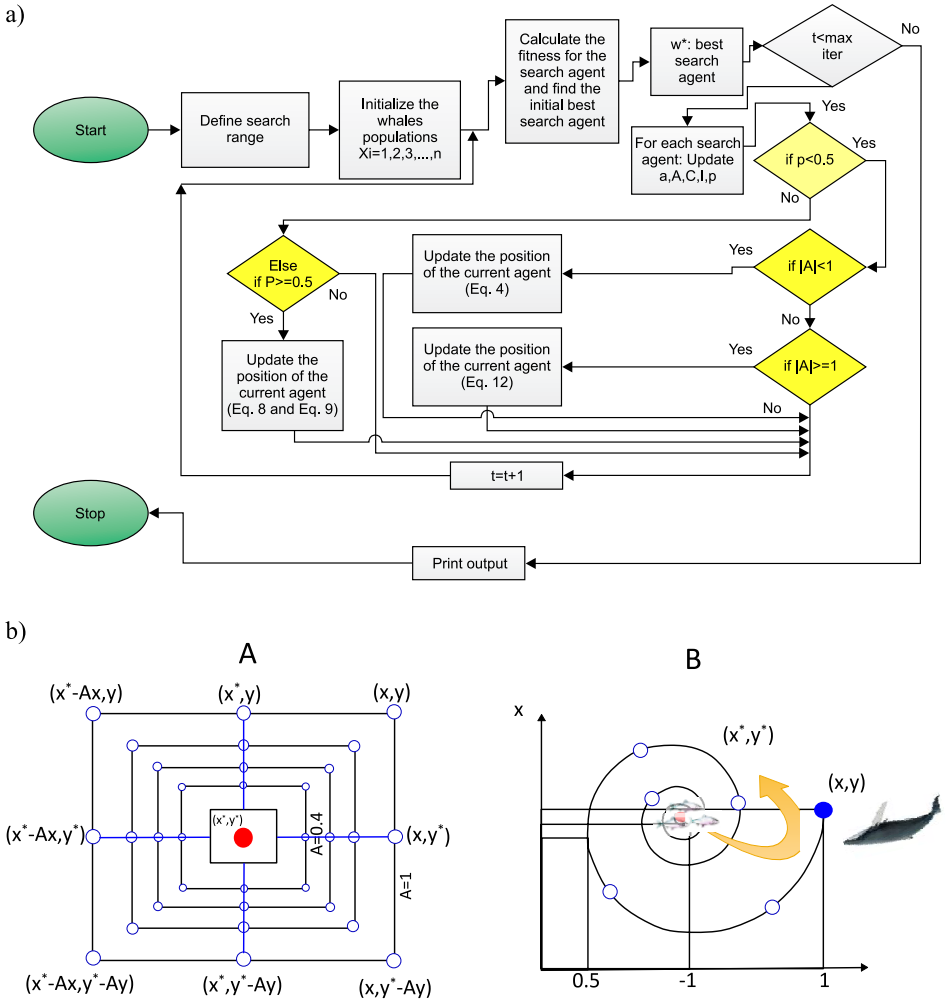


Fig. 4. a) A flowchart for the WOA heuristic algorithm, b) Bubble-net search mechanism (x* is the best solution obtained so far): (A) Shrinking encircling mechanism and (B) spiral updating position (modified after *Abdel-Basset et al., 2018*).

where x* is the best solution obtained so far and x, is the initial solution. Left panel is the shrinking encircling mechanism and right panel is spiral updating position (modified after *Abdel-Basset et al., 2018*).

The magnetic data in this paper were inverted using the misfit function ($\varphi$) given in Eq. (13), *Sharma and Biswas (2013)*. The misfit error between the measured and inverted magnetic data was evaluated utilizing the average relative error in percentage that was given by Eq. (14):

$$\varphi = \frac{1}{N}\sum_{i=1}^{N}\left(\frac{M_i^0 - M_i^c}{|M_i^0| + (M_{max}^0 - M_{min}^0)/2}\right)^2, \tag{13}$$

$$\textit{Misfit Error}\,(\%) = \left(\frac{100}{N}\right)\sqrt{\sum_{i=1}^{N}\left[\frac{M_i^0 - M_i^c}{M_i^0}\right]^2}, \tag{14}$$

where, $N$ is the number of the measured magnetic readings, $M_{min}^0$ and $M_{max}^0$ are the minimum and maximum values, respectively, of the observed data, $M_i^0$ and $M_c^0$ are the observed magnetic data and calculated one, respectively. In minimizing the ill-posed magnetic inverse problem utilizing the above expression, WOA was observed to be highly stable in the inversion process. A flowchart for the complete process of WOA is given in Fig. 4.

## 3. Theoretical examples

To check the above formulation, the WOA optimization algorithm was used for the optimization of Eq. (4) for synthetic magnetic data generated via three different models (thin dike, dipping dike, and vertical fault). Every theoretical model is tested with and without random error, and the highest random error added is 30%. The WOA inversion was executed utilizing two hundreds search agents and three hundreds iterations.

### 3.1. Thin dike model

Theoretical data were created for a thin dike model utilizing Eq. (1) with $A_e = 1000$ nT.m, $x_0 = 5$ m, $h = 8$ m, $\theta = -40°$. The number of points in this synthetic case is 61 data points with 1 meter separating between

each two successive points. Table 1 depicts the correct model parameters, search spaces for every parameter and the inverted model parameters after inversion process. For noise free data, the misfit error between observed and inverted data is 0.0214%. In Fig. 5a, the inverted magnetic data and synthetic one are depicted together. The convergence of the cost function with iteration number is presented in Fig. 5b. Residuals between synthetic magnetic data and inverted response are displayed in Fig. 5c. The suggested algorithm is additionally tested on a contaminated data with three different noise levels (10%, 20%, and 30%). The highest error observed is 1.1628% at 30% random noise.

Table 1. True and inverted model parameters using WOA algorithm due to a thin dike model. The search spaces for WOA are: $600:1500$ nT.m ($A$), $-3:10$ m ($x_0$), $-70:-30^\circ$ ($\theta$), and $4:12$ m ($h$).

| **Parameter** | $\boldsymbol{A_e}$ **(nT.m)** | $\boldsymbol{x_o}$ **(m)** | $\boldsymbol{\theta}$ **(°)** | $\boldsymbol{h}$ **(m)** | **Misfit error (%)** |
|---|---|---|---|---|---|
| true model | 1000 | 5 | −40 | 8 | – |
| noise free | 999.977 | 4.999 | −40.009 | 8.006 | **0.0214** |
| 10% noise | 989.813 | 5.024 | −39.981 | 7.946 | **0.4019** |
| 20% noise | 1008.087 | 4.972 | −40.431 | 8.272 | **1.0086** |
| 30% noise | 1003.015 | 4.848 | −39.212 | 7.992 | **1.1628** |

In the process of optimization of Eq. (4), each unknown parameter is constrained with lower and upper bounds according to the true values of these parameters, but in real field examples these bounds are controlled with the present geologic conditions in the study area. The inverted data and noisy ones of the three added levels of noise 10%, 20% and 30% are depicted in Fig. 6a,b and c, respectively. There is a good agreement between the correct model parameters and inverted solutions via WOA.

### 3.2. Dipping dike model

Alike the above theoretical example of the thin dike model, the true model parameters, the search spaces of the model parameters used during the inversion, and the estimated ones of a dipping dike model are given in Table 2. The dipping dike parameters are $b = 1$ m, $I = 100$ nT, $\theta = 50^\circ$, $h = 10$ m, $\psi = 30^\circ$ which were used to generate the synthetic data using

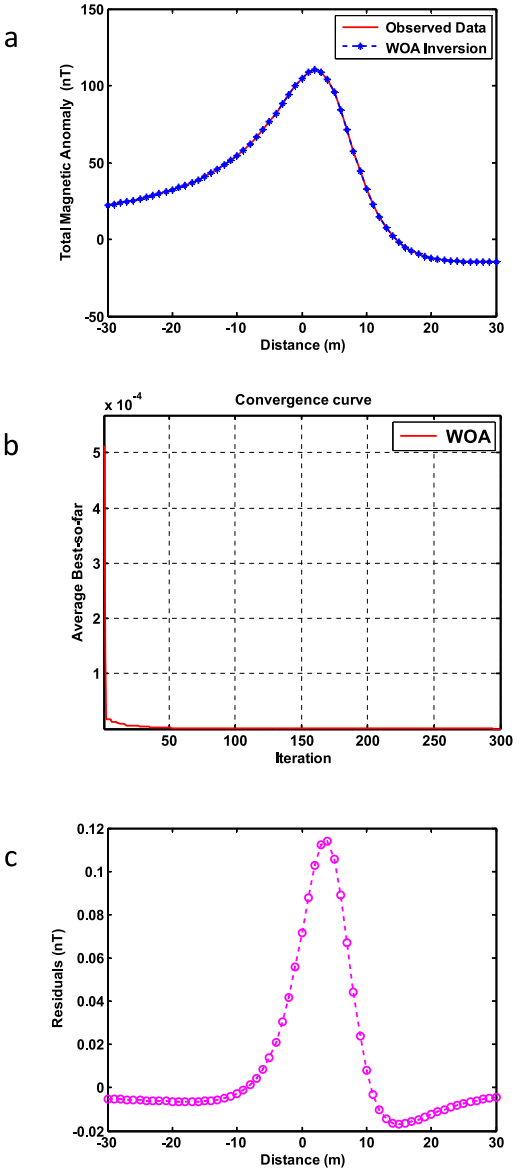


Fig. 5. WOA inversion results for synthetic magnetic anomaly of a noise free 2-D thin dike model. a) comparison between inverted response (blue) and synthetic data (red), b) convergence curve of the objective function with WOA iterations values, and c) residuals between synthetic magnetic data and inverted magnetic data from WOA.

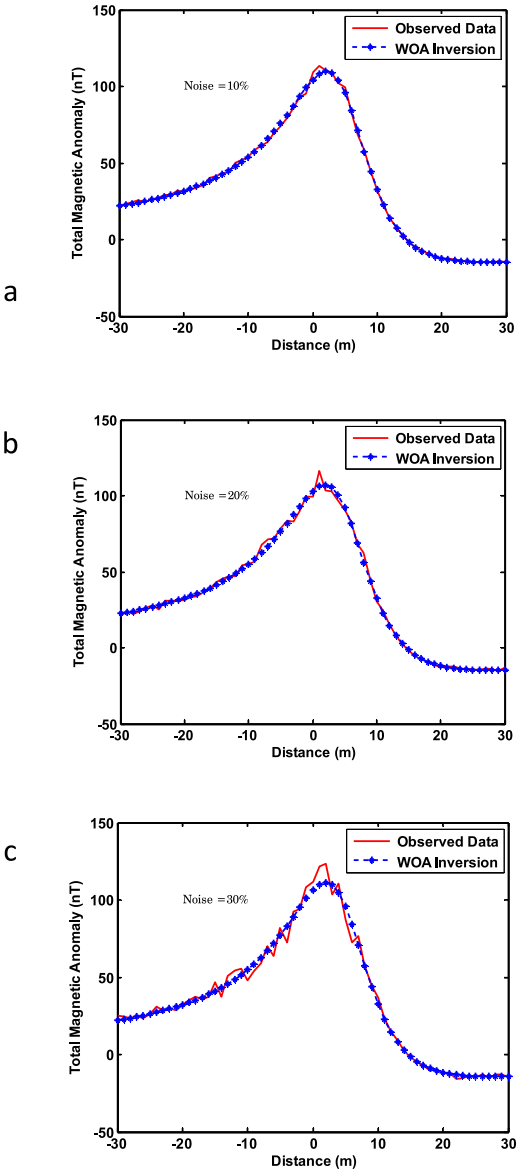


Fig. 6. Synthetic magnetic anomaly of 2-D thin dike model with their WOA inversion responses for a) with 10 % of random noise, b) with 20 % of random noise and c) with 30% of random noise.

Table 2. True and inverted model parameters using WOA algorithm due to a dipping dike model. The search spaces for WOA are: 5 : 15 m ($h$), 0.7 : 1.5 m ($b$), 80 : 120 nT ($I$), 40 : 60° ($\theta$), and 20 : 40° ($\psi$).

| **Parameter** | $h$ **(m)** | $b$ **(m)** | $I$ **(nT)** | $\theta$ (°) | $\psi$ (°) | **Misfit error (%)** |
|---|---|---|---|---|---|---|
| true model | 10 | 1 | 100 | 50 | 30 | – |
| noise free | 10 | 1.002 | 97.168 | 51.835 | 30 | **0.0029** |
| 10% noise | 10.045 | 0.980 | 104.448 | 48.496 | 30.096 | **0.2478** |
| 20% noise | 10.127 | 1.168 | 97.723 | 41.999 | 30.158 | **0.6793** |
| 30% noise | 10.031 | 1.035 | 89.261 | 55.900 | 29.909 | **0.8374** |

Eq. (2). The misfit error between observed and inverted data is 0.0029% for free noise case. Fig. 7a shows the synthetic magnetic data and the inverted one as resulted from WOA inversion. The behavior of the cost function is depicted in Fig. 7b. Differences between the synthetic magnetic data and computed one are displayed in Fig. 7c. The inversion of 30% noise, added to the synthetic data, produces a misfit error registered less than 0.9%. The computed magnetic data and synthetic noisy ones for (10%, 20% and 30%) are shown in Fig. 8a,b and c, respectively. There is a good correlation between the exact model parameters and the solutions obtained via WOA.

### 3.3. Vertical fault model

Table 3 contains the exact model parameters, the parameter spaces utilized in the WOA inversion and the calculated parameters. The vertical fault parameters used to create the theoretical magnetic data are $z = 10$ km,

Table 3. True and inverted model parameters using WOA algorithm due to a vertical fault model. The search spaces for WOA are: 1 : 15 km ($z$), 20 : 30 km ($z_b$), 0.1 : 0.9 km ($x_0$), −90 : 90° ($\theta$), and 50 : 150 nT ($K$).

| **Parameter** | $z$ **(km)** | $z_b$ **(km)** | $x_o$ **(km)** | $\theta$ (°) | $K$ **(nT)** | **Misfit error (%)** |
|---|---|---|---|---|---|---|
| true model | 10 | 25 | 0.5 | 30 | 100 | – |
| noise free | 9.843 | 25.741 | 0.266 | 30.502 | 102.568 | **0.0723** |
| 5% noise | 9.449 | 26.142 | 0.349 | 30.248 | 106.538 | **0.1609** |
| 10% noise | 10.637 | 24.394 | 0.328 | 30.459 | 93.987 | **0.3321** |
| 15% noise | 10.612 | 24.999 | 0.159 | 30.571 | 94.702 | **0.4344** |

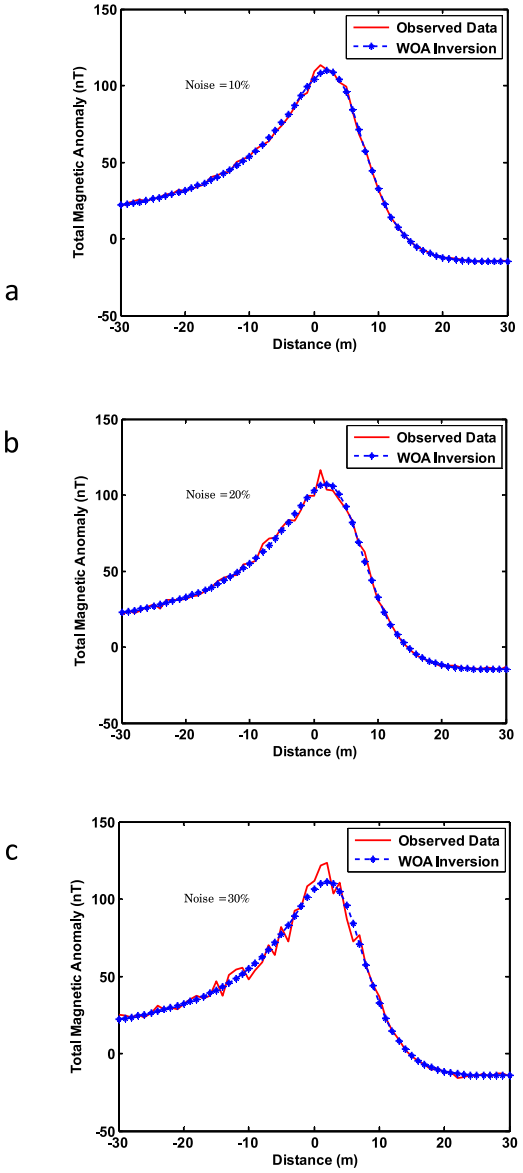


Fig. 7. WOA inversion results for synthetic magnetic anomaly of a noise free 2-D dipping dike model. a) comparison between inverted response (blue) and synthetic data (red), b) convergence curve of the objective function with WOA iterations values, and c) residuals between synthetic magnetic data and inverted magnetic data from WOA.

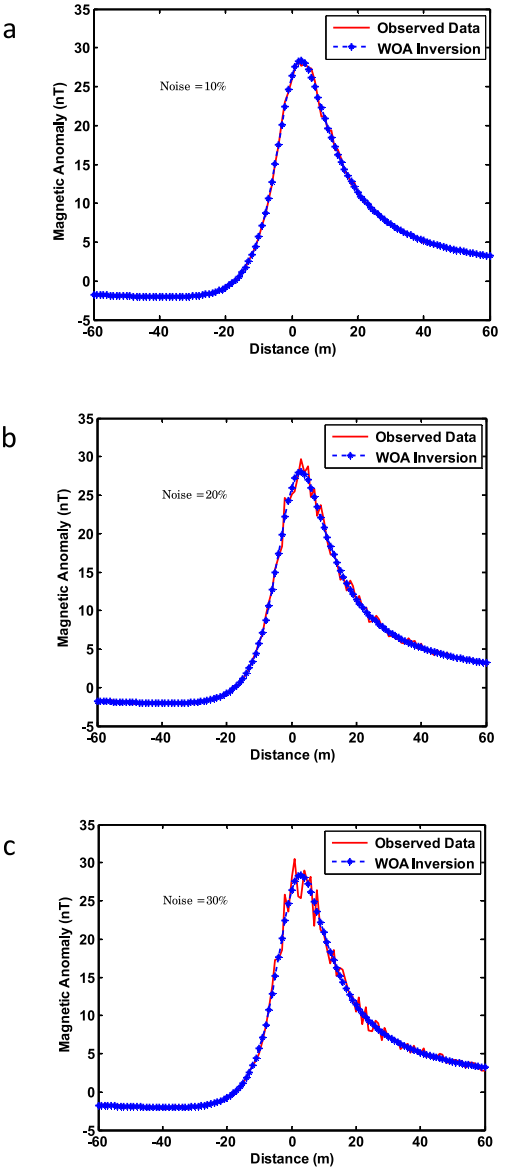


Fig. 8. Synthetic magnetic anomaly of 2-D dipping dike model with their WOA inversion responses for a) with 10% of random noise, b) with 20% of random noise and c) with 30% of random noise.

$x_0 = 0.5$ km, $z_b = 25$ km, $k = 100$ nT, $\theta = 30°$ using Eq. (3). Inversion of noise free synthetic data, concludes a misfit error not more than 0.0723% between synthetic and inverted response. A comparison between the synthetic magnetic data and calculated one via WOA is given in Fig. 9a. Average best of the misfit function is depicted in Fig. 9b, while Fig. 9c displays the differences between theoretical and computed magnetic data. The highest misfit error observed is 0.1609%, 0.3321%, and 0.4344% for the inverted 5%, 10%, and 15% noisy data as given in Table 3. The computed magnetic data and synthetic noisy one for 5%, 10%, and 15% random error are displayed together in Fig. 10a,b and c, respectively. It can be observed that the estimated parameters from the WOA inversion of data with noise are in excellent agreement with the exact ones.

## 4. Real examples

Real magnetic field data from variant locations over the world were studied to test the power and stability of the WOA inversion.

### 4.1. Diabase dike, Pishabo Lake magnetic anomaly, Ontario, Canada

This anomaly represents a total field magnetic example which was measured over an outcrop of a gabbroic olivine diabase dike, Pishabo Lake, Ontario, Canada (*McGrath and Hood, 1970; Al-Garni, 2017*) and is depicted in Fig. 11a. Aeromagnetic data has been recorded at 304 m elevation. The width of this dike is around 220 m. The entire length of the profile is 2000 m and 40 m sampling interval was used in the digitizing of this profile, so 51 data points used in the inversion. The geological cross-section of this magnetic profile is shown in Fig. 11b (after *McGrath and Hood, 1970*). The inverted parameters by WOA are as follows: $A_e = 144200.88$ nT.m, $x_0 = -6.41$ m, $h = 339.29$ m, $\theta = -37.14°$. The inverted outcomes by WOA suggest that those findings agree well with those obtained by (*El-Araby, 2003; Ekinci, 2016; Al-Garni, 2017*) as given in Table 4. The misfit error between observed and inverted data is 2.7051%. The average best of the cost function is displayed in Fig. 11c.

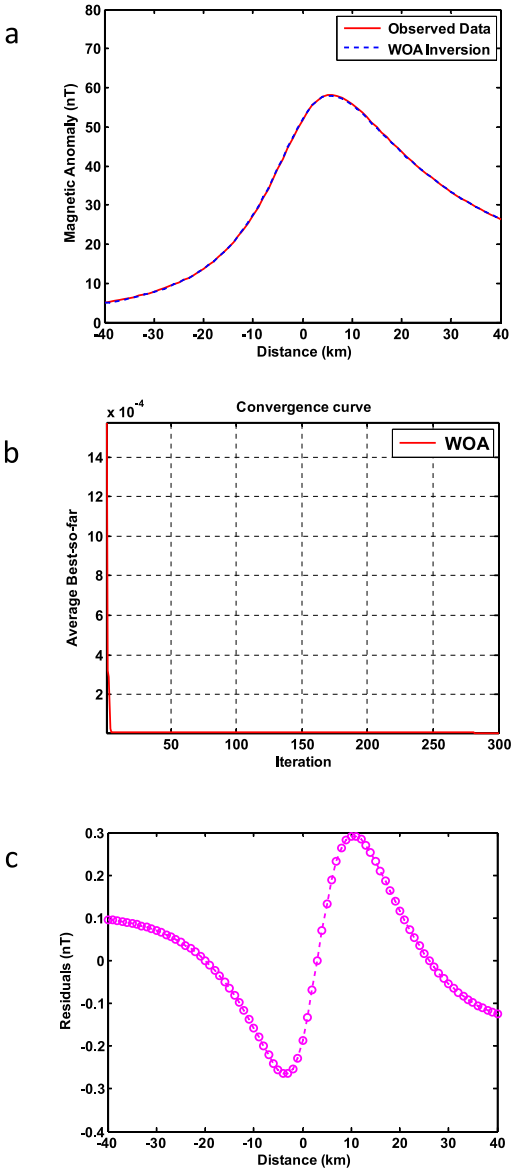


Fig. 9. WOA inversion results for synthetic magnetic anomaly of a noise free 2-D vertical fault model. a) comparison between inverted response (blue) and synthetic data (red), b) convergence curve of the objective function with WOA iterations values, and c) residuals between synthetic magnetic data and inverted magnetic data from WOA.

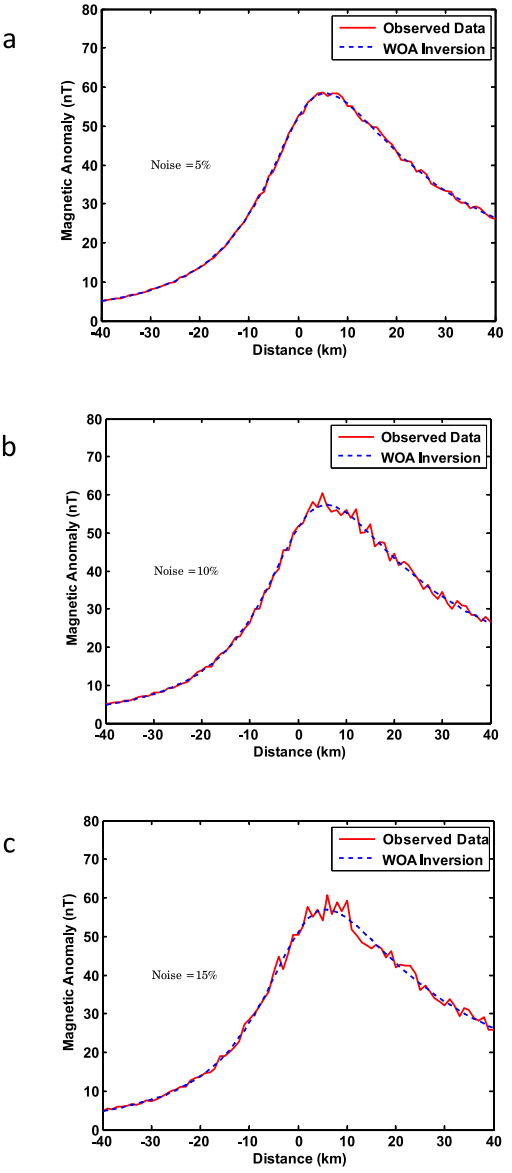


Fig. 10. Synthetic magnetic anomaly of 2-D vertical fault model with their WOA inversion responses for a) with 5% of random noise, b) with 10% of random noise and c) with 15% of random noise.

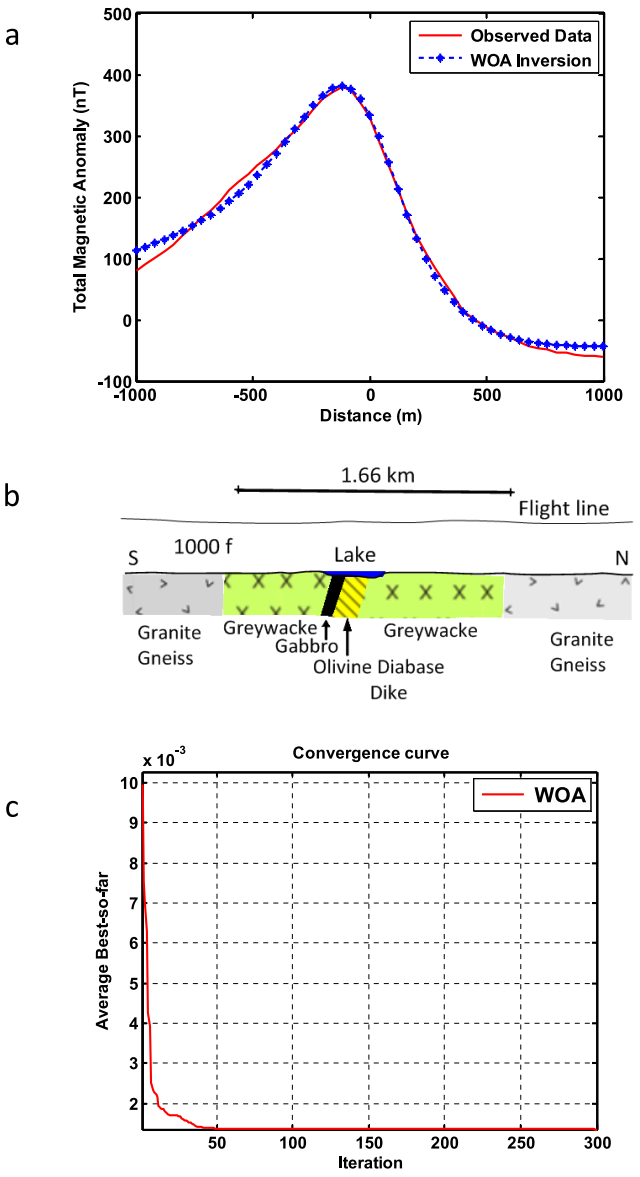


Fig. 11. WOA inversion results for Pishabo Lake magnetic Anomaly (after *McGrath and Hood, 1970*). a) Predicted response from WOA and measured data (red line), b) the corresponding geological cross-section (after *McGrath and Hood, 1970*), and c) objective function with iterations.

Table 4. WOA inversion results of Diabase dike, Pishabo Lake, Ontario, Canada (a comparison with other methods). The search spaces for WOA are: $10:200000$ nT.m ($A$), $-100:100$ m ($x_0$), $-90:90^\circ$ ($\theta$), and $1:400$ m ($h$).

| **Methods** | $\boldsymbol{A}$ **(nT.m)** | $\boldsymbol{x_o}$ **(m)** | $\boldsymbol{\theta}$ **(°)** | $\boldsymbol{h}$ **(m)** |
|---|---|---|---|---|
| *El-Araby (2003)* | – | – | – | 294.00 |
| *Ekinci (2016)* | 141,600.27 | – | −37.81 | 322.55 |
| *Al-Garni (2017)* | 139,736.73 | −6.19 | −37.37 | 323.92 |
| **WOA** | **144,200.88** | **−6.41** | **−37.14** | **339.29** |

### 4.2. Pima copper mine magnetic anomaly, Arizona, USA

The zone of Pima mining represents one of the greatest porphyry copper mine districts in USA since the nineteenth century. Mineralization interconnected with Laramide igneous activity arises in Paleozoic sedimentary rocks, Mesozoic sedimentary and volcanic sequences, and in Paleocene igneous rocks (*Shafiqullah and Langlois, 1978*). The Pima massive chalcopyrite ore bodies occur between the serpentinized dolomitic limestone and the highly altered clay-garnet limestone in an intensely altered zone consisting of a mixture of kaolin and small garnets (Fig. 12a,b), with some limestone remnants (*Thurmond and Storms, 1958*). This alteration suggests the possibility of a nearby intrusive. The thin bedded dolomitic limestone usually forms the foot wall of the massive ore bodies, although in a few places a thin bed of this formation forms the hanging wall. Where the ore body is absent, this thin-bedded, serpentinized, dolomitic limestone grades into the highly altered, clay-garnet limestone, with one formation fingering into the other (*Thurmond and Storms, 1958*). Fig. 12c shows a geologic cross section across Pima copper mine.

Fig. 13a shows the vertical magnetic field profile of the Pima copper mine, Arizona, USA (*Gay, 1963*). The profile length of this anomaly is 728 m and a sampling interval of 13 m was used in the digitizing process, so 57 points used in the WOA inversion. The inverted outcomes via WOA are as follows: $A = 41,218.73$ nT.m, $x_0 = -4.24$ m, $h = 67.93$ m, $\theta = -49.19^\circ$. The average best of the misfit function is depicted in Fig. 13b. Differences between observed and computed magnetic data are demonstrated in Fig. 13c. A comparison with other methods (*Gay, 1963; Abdelrahman et al.,*

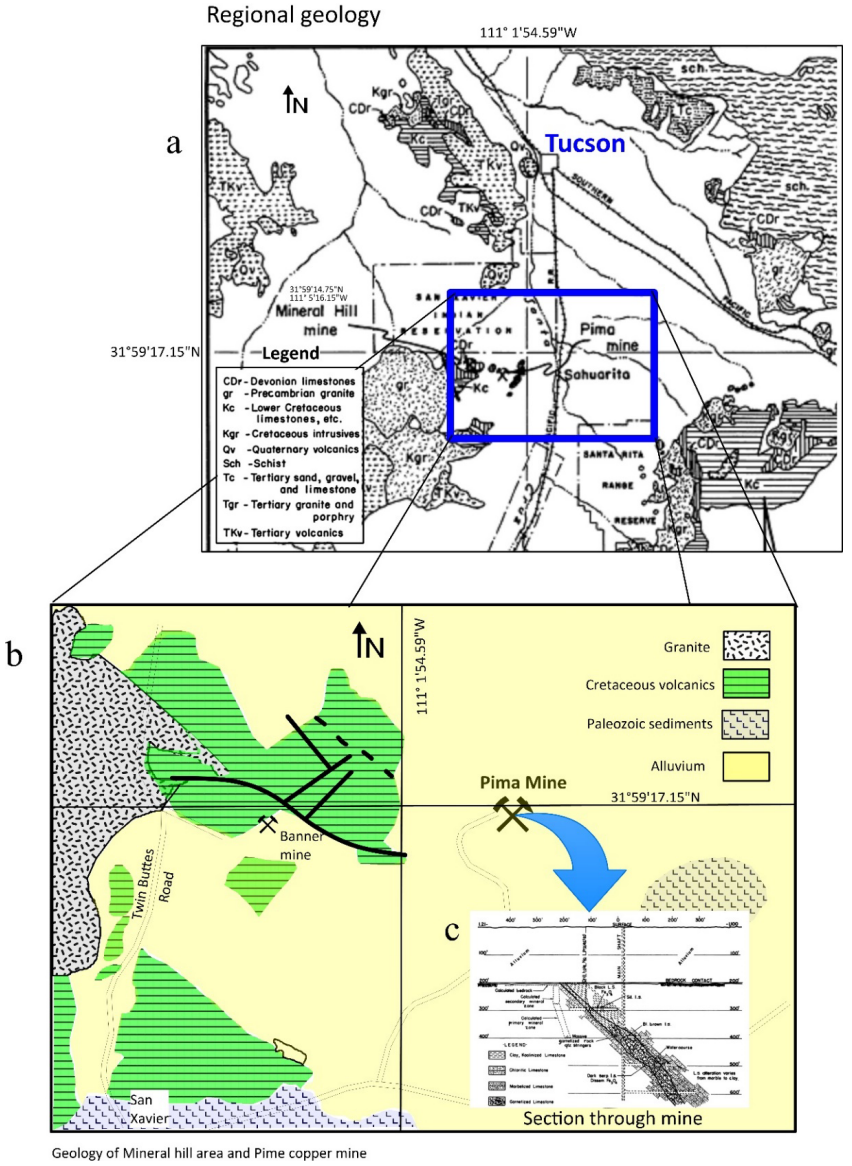


Fig. 12. General Geology of Tucson and surroundings (a), geology of mineral hill area and Pima copper mine (b), and simplified geologic cross section across Pima copper mine (c), (modified after *Thurmond and Storms, 1958*).

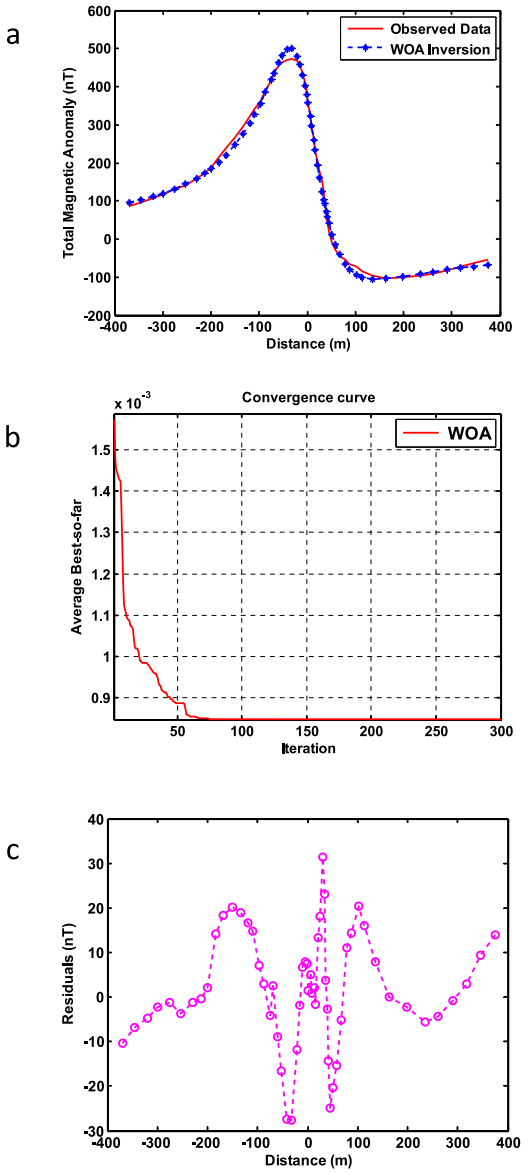


Fig. 13. WOA results for Pima copper mine magnetic Anomaly (after *Gay, 1963*). a) Calculated data from WOA (blue) and measured magnetic data (red), b) cost function with iterations, and c) residuals between measured magnetic response and inverted magnetic response from WOA.

*1989; Gobashy, 1999; Asfahani and Tlas, 2007; Tlas and Asfahani, 2011; Ekinci, 2016; Al-Garni, 2017*) was shown in Table 5.

Table 5. WOA inversion results of Pima copper mine, Arizona, USA (a comparison with other methods). The search spaces for WOA are: 10 : 100000 nT.m ($A$), −30 : 10 m ($x_0$), −60 : −40° ($\theta$), and 0 : 100 m ($h$).

| **Methods** | $A_e$ **(nT.m)** | $x_o$ **(m)** | $\theta$ **(°)** | $h$ **(m)** |
|---|---|---|---|---|
| *Gay (1963)* | – | – | −50 | 69.80 |
| *Abdelrahman and Sharafeldin (1996)* | – | – | −53 | 66.00 |
| *Asfahani and Tlas (2007)* | – | – | −50.5 | 71.5 |
| *Tlas and Asfahani (2011)* | – | −0.22 | −47.58 | 71.25 |
| *Ekinci (2016)* | 39,267.31 | – | −50.76 | 68.29 |
| *Al-Garni (2017)* | 37,065.73 | −14.23 | −44.78 | 65.63 |
| **WOA** | **41,218.73** | **−4.24** | **−49.19** | **67.93** |

### 4.3. Kiirunavaara iron mine magnetic anomaly, Sweden

Fig. 14a illustrates the vertical component of the magnetic field profile that was measured at the Kiirunavaara iron mine in northern Sweden. This field example is the largest of apatite iron ores in Sweden. *Lynch and Jönberger (2014)* explained that the Kiirunavaara group holds economically very essential iron oxide-apatite ore deposits in the districts of Kiruna and Malmberget. This magnetic field anomaly is resulted from a vein of approximately 20% magnetite (*Grant and West, 1965*). The vertical component magnetic profile has a length of 600 m and a 12 m sampling interval utilized in digitizing of this profile and fifty one points used though the inversion. The retrieved results via WOA are as follows: $A_e = 3,462,694.42$ nT.m, $x_0 = 4.89$ m, $h = 47.07$ m, $\theta = 5.86°$. A comparison with other techniques that interpreted this field example (*Grant and West, 1965; Sundararajan et al., 1985; Ekinci, 2016; Al-Garni, 2017*) was given in Table 6. The WOA results are very similar to those attained from (*Al-Garni, 2017*). The behavior of the cost function is depicted in Fig. 14b. Residuals between observed and computed magnetic data are demonstrated in Fig. 14c.

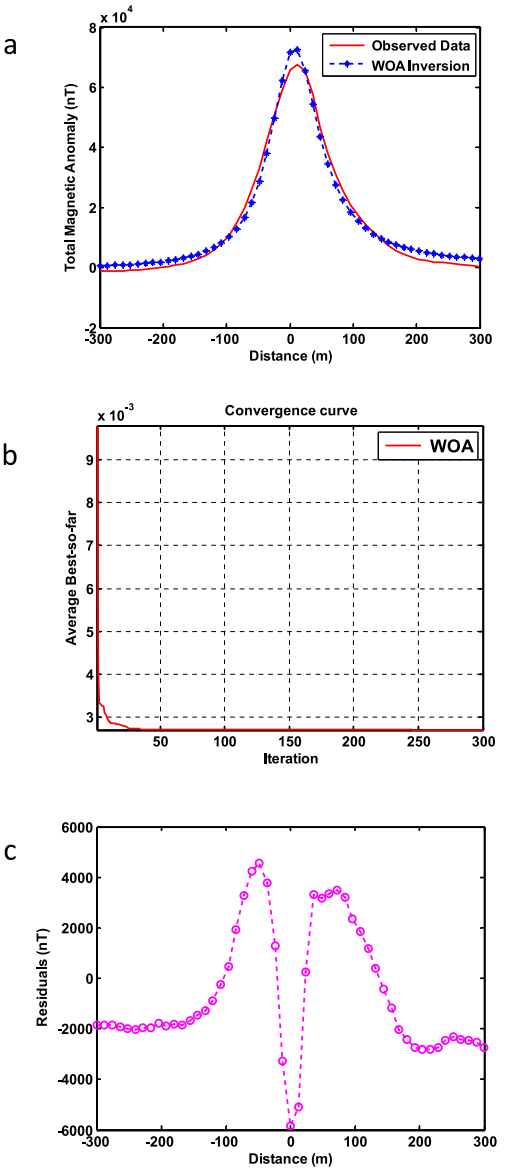


Fig. 14. WOA results for Kiirunavaara iron mine magnetic anomaly (after *Grant and West, 1965*). a) Calculated data from WOA (blue) and measured magnetic data (red), b) cost function with iterations, and c) residuals between measured magnetic response and inverted magnetic response from WOA.

Table 6. WOA inversion results of Kiirunavaara iron mine, Sweden (a comparison with other methods). The search spaces for WOA are: $10:10000000\,\mathrm{nT.m}$ ($A$), $-50:50\,\mathrm{m}$ ($x_0$), $-90:90^\circ$ ($\theta$), and $1:200\,\mathrm{m}$ ($h$).

| **Methods** | $\boldsymbol{A_e}$ **(nT.m)** | $\boldsymbol{x_o}$ **(m)** | $\boldsymbol{\theta}$ **(°)** | $\boldsymbol{h}$ **(m)** |
|---|---|---|---|---|
| *Grant and West (1965)* | – | – | – | 62–63 |
| *Sundararajan et al. (1985)* | – | – | – | 59.00 |
| *Ekinci (2016)* | 3,713,125.65 | – | 10.39 | 56.09 |
| *Al-Garni (2017)* | 3,483,203.00 | 13.91 | 2.17 | 49.70 |
| **WOA** | **3,462,694.42** | **4.24** | **5.86** | **47.07** |

### 4.4. Marcona magnetic anomaly, Marcona district, Peru

The iron oxide-copper-gold (IOCG) mineralization (Mesozoic age) sub-province of littoral south-central Perú, centered at latitude 15° 11′ S, longitude 75° 6′ W, incorporates Marcona (Fig. 15a), the pre-eminent central Andean iron oxide deposit (1.9 Gt @ 55.4% Fe), and Mina Justa, one of the few major Andean IOCG deposits with economic copper grades (346.6 Mt @ 0.71% Cu) (*Chen et al., 2010*). The mineralized area is intruded by a swarm of hypabyssal bodies. These range from apparently syn- to clearly post-mineralization and, in composition, from silicic to, rarely, ultramafic (hornblende pyroxenite: *Atchley, 1956*), but magmatic chemistry and mineralogy are almost everywhere disguised by alteration (*Chen et al., 2010*). Fig. 15b shows geology of the Marcona-Mina Justa district (modified from *Chen et al., 2010*). An en echelon array of 12 major magnetite ore bodies ("minas") and 55 smaller "cuerpos" is recognized in Marcona mine. This is probably the source of the high magnetic anomaly over the mine.

Fig. 16a depicts the magnetic field example due to a dipping dike (*Gay, 1963*) close to the magnetic equator in the Marcona district, Peru which was digitized at 10 m interval and 121 data points is used in the WOA inversion. The inverted parameters by WOA are as follows: $b = 196.44$ m, $I = 1057.78$ nT, $\theta = 58.57^\circ$, $h = 150.00$ m, $\psi = -50.72^\circ$. The misfit error between observed and inverted data from WOA is 0.9824%. Table 7 shows a comparison with other approaches in the literature which studied this field example as a dipping dike (*Gay, 1963; Koulomzine et al., 1970; Pal,*

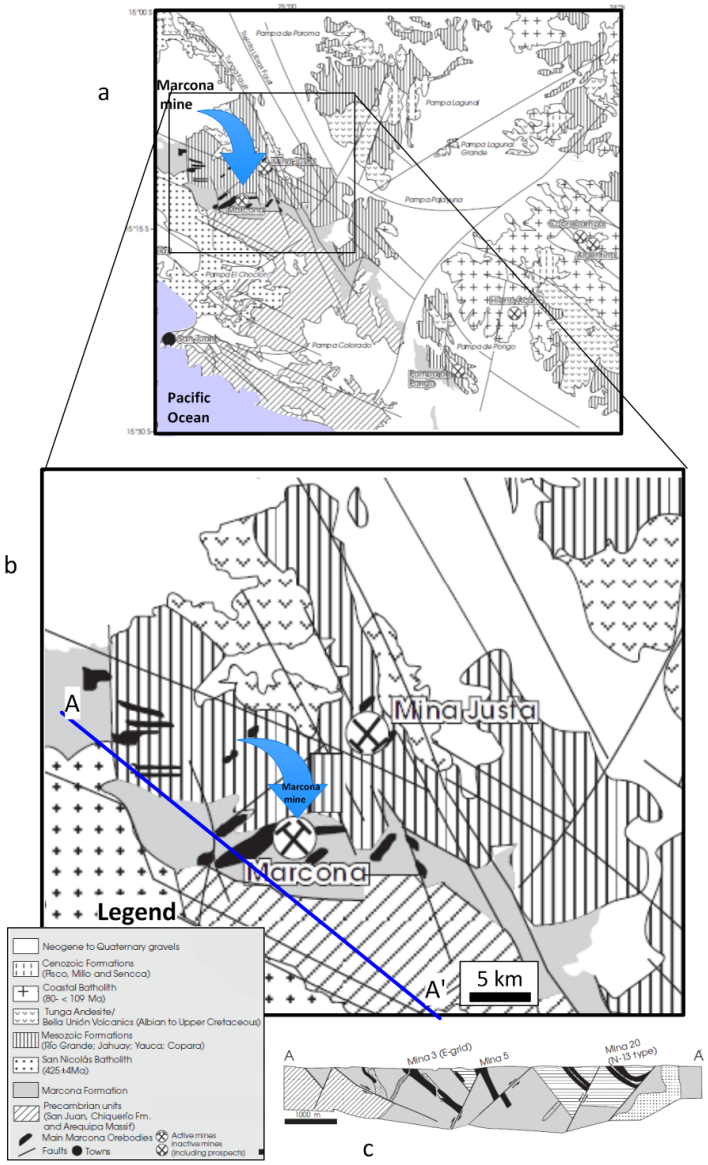


Fig. 15. General geology of the Marcona-Mina Justa district (modified after *Chen et al., 2010*) (a) and (b); Schematic cross section of Marcona mine area (A–A' in Fig. 15a), the magnetite ore bodies are extensively dislocated by faults (c).

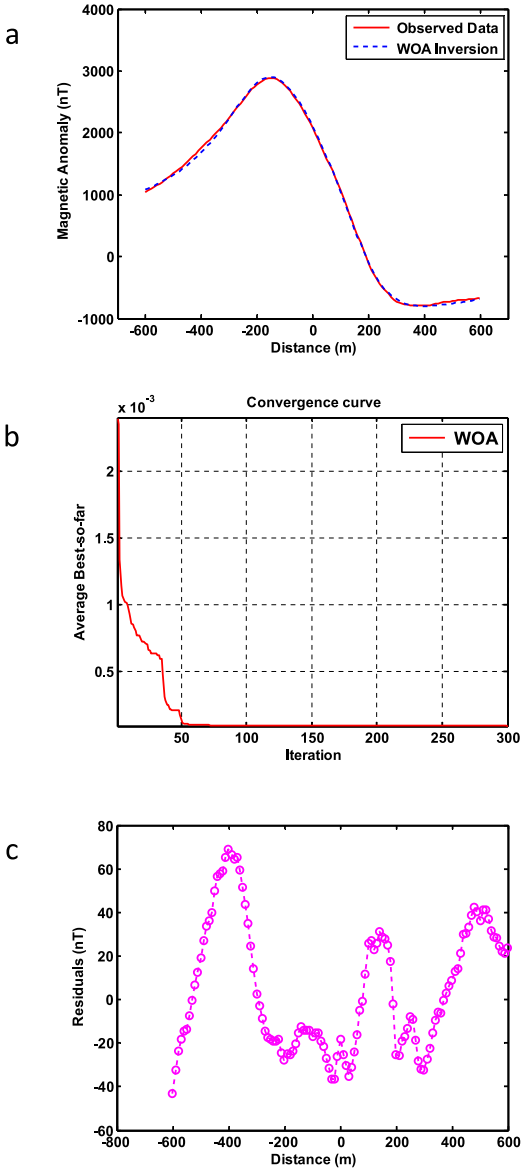


Fig. 16. WOA results for Marcona magnetic Anomaly (after *Gay, 1963*). a) Calculated data from WOA (blue) and measured magnetic data (red), b) cost function with iterations, and c) residuals between measured magnetic response and inverted magnetic response from WOA.

Table 7. WOA inversion results of Marcona magnetic anomaly, Marcona district, Peru (a comparison with other methods). The search spaces for WOA are: 70 : 150 m ($h$), 100 : 250 m ($b$), 500 : 1500 nT ($I$), 10 : 80° ($\theta$), and −80 : 80° ($\psi$).

| **Methods** | $h$ **(m)** | $b$ **(m)** | $I$ **(nT)** | $\theta$ (°) | $\psi$ (°) |
|---|---|---|---|---|---|
| *Gay (1963)* | 124.00 | 186.00 | – | – | −50.00 |
| *Koulomzine et al. (1970)* (1st solution) | 126.70 | 205.95 | – | – | −50.10 |
| *Koulomzine et al. (1970)* (2nd solution) | 135.50 | 202.75 | – | – | −50.50 |
| *Pal (1985)* | 132.60 | 193.75 | – | – | −49.30 |
| *Al-Garni (2015)* | 130.00 | 191.70 | 808.30 | 65.49 | −64.60 |
| **WOA** | **150.00** | **196.44** | **1057.78** | **58.57** | **−50.72** |

*1985; Al-Garni, 2015*). The inverted outcomes from our algorithm are in well agreement with those attained from methods interpreted this example as in Table 7. The behavior of the objective function is depicted in Fig. 16b and residuals between observed and computed magnetic data are displayed in Fig. 16c.

### 4.5. The aeromagnetic anomaly of Bihar, India

Fig. 17a depicts the aeromagnetic field anomaly measured at 2500 ft. above a dubitable deep positioned fault southwest of Dehri, Bihar, India. The anomaly is digitized at 1 km interval and 52 data points used in the WOA inversion. The survey area is enveloped by Uindhyan and sediments are connected with Bijawar rocks. The retrieved results via WOA are as follows: $z = 9.235\,\text{km}$, $x_0 = -2\,\text{km}$, $z_b = 24.538\,\text{km}$, $k = 856.400\,\text{nT}$, $\theta = -131.813°$. Table 8 shows a comparison with other approaches in the literature which studied this field example as a vertical fault (*Qureshi and Nalaye, 1978; Atchuta Rao and Ram Babu, 1983; Asfahani and Tlas, 2007; Tlas and Asfahani, 2011*). The inverted outcomes from our algorithm agreed well with those attained from methods interpreted this example as in Table 8. The average best of the misfit function is depicted in Fig. 17b. Differences between observed and computed magnetic data are demonstrated in Fig. 17c.

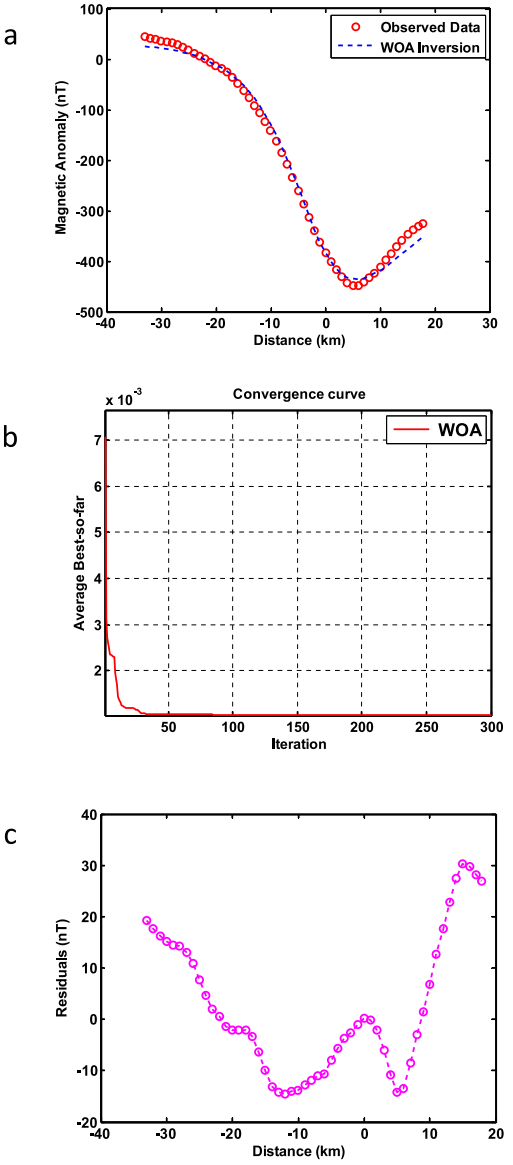


Fig. 17. WOA results for aeromagnetic Field Anomaly of Southwest of Dehri (after *Qureshi and Nalaye, 1978*). a) Calculated data from WOA (blue) and measured magnetic data (red circles), b) cost function with iterations, and c) residuals between measured magnetic response and inverted magnetic response from WOA.

Table 8. WOA inversion results of aero-magnetic of southwest of Dehri anomaly, Bihar, India (a comparison with other methods). The search spaces for WOA are: $1:15$ km ($z$), $20:50$ km ($z_b$), $-4:2$ km ($x_0$), $-270:90^\circ$ ($\theta$), and $500:1000$ nT ($K$).

| **Methods** | $z$ **(km)** | $z_b$ **(km)** | $x_o$ **(km)** | $\theta$ (°) | $K$ **(nT)** |
|---|---|---|---|---|---|
| *Qureshi and Nalaye (1978)* | 7.5 | 30 | – | −133 | – |
| *Atchuta Rao and Ram Babu (1983)* | 8 | 32 | – | −130 | – |
| *Asfahani and Tlas (2007)* | 10.2 | 25.5 | – | −141.7 | 815 |
| *Tlas and Asfahani (2011)* | 10.54 | 25.22 | 0.04 | −141.60 | 789.38 |
| **WOA** | **9.235** | **24.538** | **−2** | **−131.813** | **856.400** |

### 4.6. The magnetic anomaly of the western margin of Perth basin, Australia

The Perth basin is a major rift structure running parallel to the south-western coast of Australia (Fig. 18). The eastern boundary of the basin is clearly defined by the Darling fault which separates it from the Yilgam block comprising Archaean rocks of the Australian shield (*Qureshi and Nalaye, 1978*). The western boundary of the rift is recognized in the north in the Northampton block and in the south in the Leeuwin block, both made up of Precambrian rocks and faulted on the east to a varying degree of intensity An aeromagnetic survey conducted by the Bureau of Mineral Resources has revealed that the boundary may underlie the strong anomalies which run roughly in the north-south direction in this region This magnetic anomaly (*Qureshi and Nalaye, 1978*), is digitized at 1 km interval and 42 data points and used in the WOA inversion (Fig. 19a). The inverted parameters by WOA are as follows: $z = 6.032$ km, $x_0 = -1.731$ km, $z_b = 13.036$ km, $k = 213.161$ nT, $\theta = 48.092^\circ$. The misfit error between observed and inverted data from WOA is 3.7193%. A comparison with other techniques that interpreted this field example (*Qureshi and Nalaye, 1978; Atchuta Rao and Ram Babu, 1983; Asfahani and Tlas, 2007; Tlas and Asfahani, 2011*) was given in Table 9. The behavior of the cost function is depicted in Fig. 19b. Inverted outcomes from our algorithm are in well agreement with those attained from methods interpreted this example as in Table 9. Residuals between observed and computed magnetic data are demonstrated in Fig. 19c.

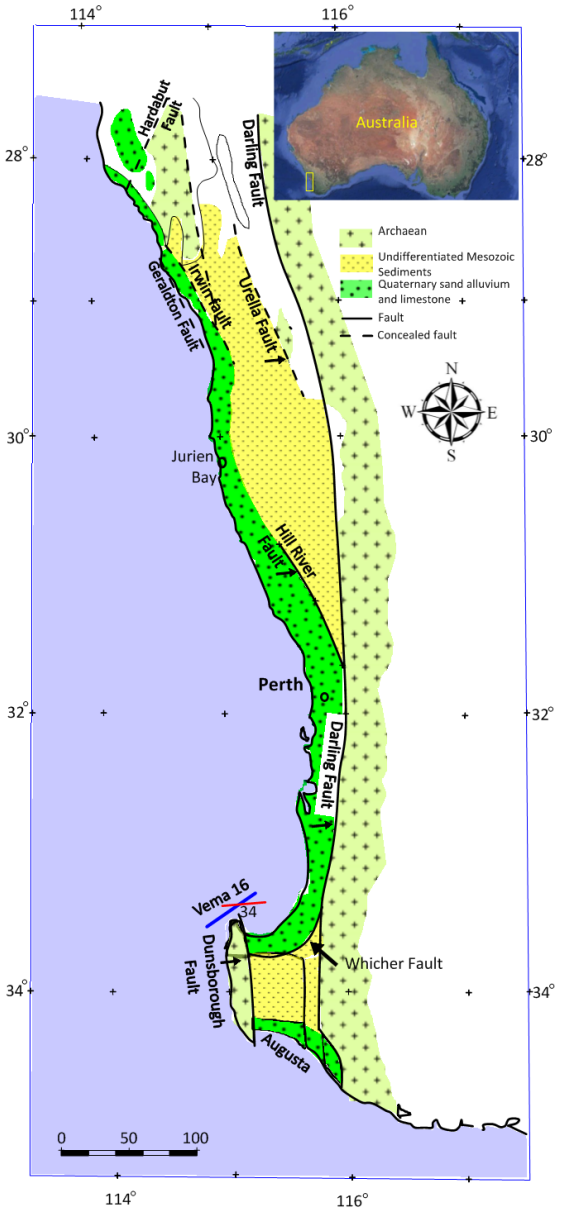


Fig. 18. General geologic map of Perth basin, Australia. Position of faults are posted based on *Wilson (1957)* (figure modified after *Hawkins et al., 1965*).

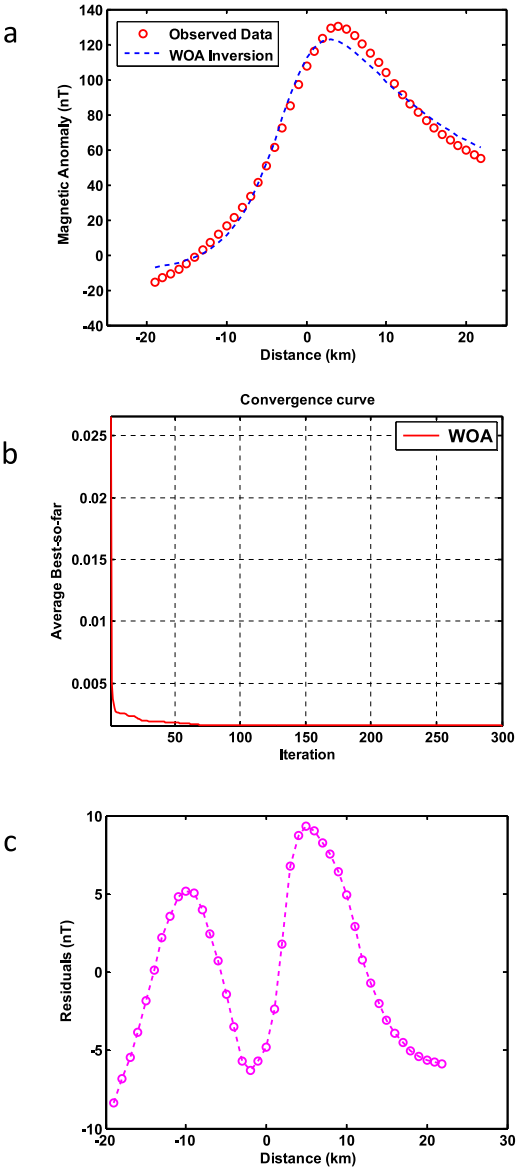


Fig. 19. WOA results for magnetic field anomaly of the western margin of Perth basin (after *Qureshi and Nalaye, 1978*). a) Calculated data from WOA (blue) and measured magnetic data (red circles), b) cost function with iterations, and c) residuals between measured magnetic response and inverted magnetic response from WOA.

Table 9. WOA inversion results of western margin of Perth basin anomaly, Australia (a comparison with other methods). The search spaces for WOA are: 1 : 30 km ($z$), 1 : 100 km ($z_b$), −4 : 4 km ($x_0$), −90 : 90° ($\theta$), and 100 : 300 nT ($K$).

| **Methods** | $z$ **(km)** | $z_b$ **(km)** | $x_o$ **(km)** | $\theta$ **(°)** | $K$ **(nT)** |
|---|---|---|---|---|---|
| *Qureshi and Nalaye (1978)* | 5.80–6.85 | 15.55–17.00 | – | 30 | – |
| *Atchuta Rao and Ram Babu (1983)* | 6.26 | 15.45 | – | 40 | – |
| *Asfahani and Tlas (2007)* | 7.5 | 14 | – | 39.8 | 200.3 |
| *Tlas and Asfahani (2011)* | 7.22 | 13.72 | 0.88 | 35.54 | 200.56 |
| **WOA** | **6.032** | **13.036** | **−1.731** | **48.092** | **213.161** |

## 5. Conclusion

A proficient algorithm is suggested for the elucidation of magnetic field data resulted from simple shaped subsurface geo-bodies like a thin dike, a dipping dike, and a vertical fault using Whale Optimization Algorithm (WOA), global meta-heuristic optimization technique, for ore and mineral investigation. By applying this technique, a best evaluation of the horizontal position, the depth to the upper surface (center) of the buried body, the effective magnetization angle, dip angle of the dipping dike, depths to the upper and to the lower edges of the fault and the amplitude coefficient is easily attained. The efficiency of our algorithm is illustrated through the examination on synthetic magnetic data generated via three different models (thin dike, dipping dike, and vertical fault). Every theoretical model is tested with and without random error, and the highest random error added is 30%.

Being hypothetically proved, this recent suggested algorithm was applied to real case studies from Canada, United States, Sweden, Peru, India, and Australia. The agreement between the results obtained by such a technique and those reported by other interpretation methods is good and comparable. Furthermore, the convergence towards the optimal estimation of parameters is assured and rapidly reached. One more advantage is that the probability of being trapped in local minimum is low, which is an advantage of meta-heuristic methods. Those essential characteristics give the new proposed method power over other published interpretative methods.

## References

Abdelazeem M., Gobashy M., Khalil M. H., Abdrabou, M., 2019: A complete model parameter optimization from self-potential data using Whale algorithm. J. Appl. Geophys., **170**, 103825, doi: 10.1016/j.jappgeo.2019.103825.

Abdelazeem M., Gobashy M., 2006: Self-potential inversion using genetic algorithm. Journal of King Abdulaziz University, JKAU: Earth Sci., **17**, 1, 83–101, doi: 10.4197/Ear.17-1.5.

Abdelazeem M., 2001: Robust Numerical Inversion of the magnetic anomalies due to long horizontal cylinders. Paper presented in the second international conference on the geology of Africa, Assiut, Egypt.

Abdel-Basset M., Manogaran G., El-Shahat D., Mirjalili S., 2018: A hybrid whale optimization algorithm based on local search strategy for the permutation flow shop scheduling problem. Future Gener. Comput. Syst., **85**, 129–145, doi: 10.1016/j.future.2018.03.020.

Abdelrahman E. M., Bayoumi A. I., Abdelhady Y. E., Gobashy M. M., Elaraby H. M., 1989: Gravity interpretation using correlation factors between successive order least-squares residual anomalies. Geophysics, **54**, 12, 1614–1621, doi: 10.1190/1.1442629.

Abdelrahman E. M., Sharafeldin S. M., 1996. An iterative least-squares approach to depth determination from residual magnetic anomalies due to thin dikes. J. Appl. Geophys., **34**, 3, 213–220, doi: 10.1016/0926-9851(95)00017-8.

Abdelrahman E. M., Abdelazeem M., Gobashy M., 2019: A minimization approach to depth and shape determination of mineralized zones from potential field data using the Nelder-Mead simplex algorithm. Ore Geol. Rev., **114**, 103123, doi: 10.1016/j.oregeorev.2019.103123.

Al-Garni M. A., 2015: Interpretation of magnetic anomalies due to dipping dikes using neural network inversion. Arab. J. Geosci., **8**, 10, 8721–8729, doi: 10.1007/s12517-014-1770-7.

Al-Garni M. A., 2017: Inversion of magnetic anomalies due to isolated thin dike-like sources using artificial neural networks. Arab. J. Geosci., **10**, 15, 337, doi: 10.1007/s12517-017-3115-9.

Asfahani J., Tlas M., 2007: A robust nonlinear inversion for interpretation of magnetic anomalies caused by faults, thin dikes and spheres like structure using stochastic algorithms. Pure Appl. Geophys., **164**, 2023–2042, doi: 10.1007/s00024-007-0254-z.

Atchley F. W., 1956: Geology of the Marcona iron deposits, Peru. Unpublished Ph.D. thesis, California, Stanford University, 150 p.

Atchuta Rao D., Ram Babu H. V., 1983: Standard curves for the interpretation of magnetic anomalies over vertical faults. Geophys. Res. Bull., **21**, 1, 71–89.

Biswas A., 2015: Interpretation of residual gravity anomaly caused by a simple shaped body using very fast simulated annealing global optimization. Geosci. Front., **6**, 6, 875–893, doi: 10.1016/j.gsf.2015.03.001.

Biswas A., Acharya T., 2016: A very fast simulated annealing method for inversion of magnetic anomaly over semi-infinite vertical rod-type structure. Model. Earth Syst. Environ., **2**, 4, 198, doi: 10.1007/s40808-016-0256-x.

Biswas A., Sharma S. P., 2014a: Resolution of multiple sheet-type structures in self-potential measurement. J. Earth Syst. Sci., **123**, 4, 809–825, doi: 10.1007/s12040-014-0432-1.

Biswas A., Sharma S. P., 2014b: Optimization of self-potential interpretation of 2-D inclined sheet-type structures based on very fast simulated annealing and analysis of ambiguity. J. Appl. Geophys., **105**, 235–247, doi: 10.1016/j.jappgeo.2014.03.023.

Biswas A., Sharma S. P., 2015: Interpretation of self-potential anomaly over idealized body and analysis of ambiguity using very fast simulated annealing global optimization technique. Near Surf. Geophys., **13**, 2, 179–195, doi: 10.3997/1873-0604.2015005.

Biswas A., Sharma S. P., 2016: Integrated geophysical studies to elicit the structure associated with Uranium mineralization around South Purulia Shear Zone, India: A review. Ore Geol. Rev., **72**, 2, 1307–1326, doi: 10.1016/j.oregeorev.2014.12.015.

Bruckshaw J. M., Kunaratnam K., 1963: The interpretation of magnetic anomalies due to dikes. Geophys. Prospect., **11**, 4, 519–522, doi: 10.1111/j.1365-2478.1963.tb02049.x.

Chen H., Clark A., Kyser T., Ullrich T., Baxter R., Chen Y., Moody T., 2010: Evolution of the Giant Marcona-Mina Justa Iron Oxide-Copper-Gold District, South-Central Peru. Econ. Geol., **105**, 1, 155–185, doi: 10.2113/gsecongeo.105.1.155.

Ekinci Y. L., 2016: MATLAB-based algorithm to estimate depths of isolated thin dike-like sources using higher-order horizontal derivatives of magnetic anomalies. Springer Plus, **5**, 1384, doi: 10.1186/s40064-016-3030-7.

El-Araby H. M., 2003: Quantitative interpretation of numerical horizontal magnetic gradients over dipping dikes. Bull. Fac. Sci. Cairo Univ., **71**, 97–121.

El-Kaliouby H. M., Al-Garni M. A., 2009: Inversion of self-potential anomalies caused by 2D inclined sheets using neural networks. J. Geophys. Eng., **6**, 1, 29–34, doi: 10.1088/1742-2132/6/1/003.

Gay S. P., 1963: Standard curves for interpretation of magnetic anomalies over long tabular bodies. Geophysics, **28**, 2, 161–200, doi: 10.1190/1.1439164.

Gay S. P., 1965: Standard curves for the interpretation of magnetic anomalies over long horizontal cylinders. Geophysics, **30**, 5, 818–828, doi: 10.1190/1.1439656.

Gerovska D., Araúzo-Bravo M. J., 2003: Automatic interpretation of magnetic data based on Euler deconvolution with unprescribed structural index. Comput. Geosci., **29**, 8, 949–960, doi: 10.1016/S0098-3004(03)00101-8.

Gobashy M. M., 1999: A quasi-Newton scheme for two-dimensional inversion of gravity data. Delta J. Sci., Tanta University, Egypt, **23**.

Gobashy M., Abdelazeem M., Abdrabou M., Khalil M., 2020: Estimating Model Parameters from Self-Potential Anomaly of 2D Inclined Sheet Using Whale Optimization Algorithm: Applications to Mineral Exploration and Tracing Shear Zones. Nat. Resour. Res., **29**, 1, 499–519, doi: 10.1007/s11053-019-09526-0.

Göktürkler G., Balkaya Ç., 2012: Inversion of self-potential anomalies caused by simple geometry bodies using global optimization algorithms. J. Geophys. Eng., **9**, 5, 498–507, doi: 10.1088/1742-2132/9/5/498.

Grant F. S., West G. F., 1965: Interpretation Theory in Applied Geophysics. New York: McGraw-Hill, 583 p.

Hartman R. R., Tesky D. J., Friedberg J. L., 1971: A system for rapid digital aeromagnetic interpretation. Geophysics, **36**, 5, 891–918, doi: 10.1190/1.1440223.

Hawkins L. V., Hennion J. F., Nafe J. E., Thyer R. F., 1965: Geophysical investigations in the area of the Perth Basin, Western Australia. Geophysics, **30**, 6, 1026–1052, doi: 10.1190/1.1439686.

Koulomzine T., Lamontagne Y., Nadeau A., 1970: New methods for the direct interpretation of magnetic anomalies caused by inclined dikes of infinite length. Geophysics, **35**, 5, 812–830, doi: 10.1190/1.1440131.

Ku C. C., Sharp J. A., 1983: Werner deconvolution for automated magnetic interpretation and its refinement using Marquardt's inverse modelling. Geophysics, **48**, 6, 754–774, doi: 10.1190/1.1441505.

Li X., 2003: On the use of different methods for estimating magnetic depth: Lead. Edge, **22**, 11, 1090–1099, doi: 10.1190/1.1634912.

Li X., Yin M., 2012: Application of differential evolution algorithm on self-potential data. PLoS ONE, **7**, 12, doi: 10.1371/journal.pone.0051199.

Lynch E. P., Jönberger J., 2014: Summary report on available geological, geochemical and geophysical information for the Nautanen key area, Norrbotten. Geological Survey of Sweden, report No. 34.

McGrath P. H., Hood P. J., 1970: The dipping dike case, a computer curve matching method of magnetic interpretation. Geophysics, **35**, 5, 831–848, doi: 10.1190/1.1440132.

Mirjalili S., Lewis A., 2016: The Whale Optimization Algorithm. Adv. Eng. Softw., **95**, 51–67, doi: 10.1016/j.advengsoft.2016.01.008.

Mohan N. L., Sundararajan N., Seshagiri Rao S. V., 1982: Interpretation of some two-dimensional magnetic bodies using Hilbert transforms. Geophysics, **47**, 3, 376–387, doi: 10.1190/1.1441342.

Monteiro Santos F. A., 2010: Inversion of self-potential of Idealized bodies anomalies using particle swarm optimization. Comput. Geosci., **36**, 9, 1185–1190, doi: 10.1016/j.cageo.2010.01.011.

Nettleton L. L., 1976: Gravity and magnetic in oil prospecting. New York: McGraw-Hill, 464 p.

Pal P. C., 1985: A gradient analysis based simplified inversion strategy for the magnetic anomaly of an inclined and infinite thick dike. Geophysics, **50**, 7, 1179–1182, doi: 10.1190/1.1441992.

Pasteka R., 2006: The role of the interference polynomial in the Euler deconvolution algorithm. Boll. di Geofis. Teor. ed Appl., **47**, 1-2, 171–180.

Prakasa Rao T. K. S., Subrahmanyan M., Srikrishna Murthy A., 1986: Nomograms for direct interpretation of magnetic anomalies due to long horizontal cylinders. Geophysics, **51**, 11, 2156–2159, doi: 10.1190/1.1442067.

Qureshi I. R., Nalaye A. M., 1978: A method for the direct interpretation of magnetic anomalies caused by two-dimensional vertical faults. Geophysics, **43**, 1, 179–188, doi: 10.1190/1.1440819.

Reid A. B., Allsop J. M., Granser H., Millet A. J., Somerton I. W., 1990: Magnetic interpretation in three dimensions using Euler deconvolution. Geophysics, **55**, 1, 80–91, doi: 10.1190/1.1442774.

Rao B. S. R., Murthy I. V. R., 1978: Gravity and magnetic methods of prospecting. New Delhi: Arnold Heinneman, 390 p.

Salem A., 2005: Interpretation of magnetic data using analytic signal derivations. Geophys. Prospect., **53**, 1, 75–82, doi: 10.1111/j.1365-2478.2005.00434.x.

Salem A., Ravat D., 2003: A combined analytic signal and Euler method (AN-EUL) for automatic interpretation of magnetic data. Geophysics, **68**, 6, 1952–1961, doi: 10.1190/1.1635049.

Shafiqullah M., Langlois J. D., 1978: The Pima mining district Arizona: a geochronologic update. In: Callender J. F., Wilt J., Clemons R. E., James H. L. (Eds.): Land of Cochise (Southeastern Arizona), New Mexico Geological Society 29th Annual Fall Field Conference Guidebook, 348 p., 321–327.

Sharma S. P., Biswas A., 2013: Interpretation of self-potential anomaly over 2D inclined structure using very fast simulated annealing global optimization – An insight about ambiguity. Geophysics, **78**, 3, WB3–WB15, doi: 10.1190/geo2012-0233.1.

Singh A., Biswas A., 2016: Application of global particle swarm optimization for inversion of residual gravity anomalies over geological bodies with idealized geometries. Nat. Resour. Res., **25**, 3, 297–314, doi: 10.1007/s11053-015-9285-9.

Sundararajan N., Mohan N. L., Vijaya Raghava M. S., Seshagiri Rao V.S., 1985: Hilbert transform in the interpretation of magnetic anomalies of various components due to thin infinite dike. Pure Appl. Geophys., **123**, 4, 557–566, doi: 10.1007/BF00877453.

Sungkono S., Desa Warnana D., 2018: Black hole algorithm for determining model parameter in self-potential data. J. Appl. Geophys., **148**, 189–200, doi: 10.1016/j.jappgeo.2017.11.015.

Sweilam N. M., Abdelazeem M., El-Metwally K., 2007: Self-potential signals inversion to simple polarized bodies using the particle swarm optimization method: A visibility study. J. Appl. Geophys. (ESAP-Egypt), **6**, 1, 195–208.

Sweilam N. H., Gobashy M. M., Hashem T., 2008: Using particle swarm optimization with function stretching (SPSO) for inverting gravity data: A visibility study. Journal of Physics and mathematics, Science Bull., Cairo University, **86**, 2, 259–283.

Wilson A. F., 1957: Geological map of the older Precambrian rocks of southwest Australia. J. Roy. Soc. West. Aust.

Telford W. M., Geldart L. P., Sheriff R. A., Keys D. A., 1976: Applied Geophysics. Cambridge University Press, Cambridge, 860 p.

Thurmond R. E., Storms W. R., 1958: Discovery and development of the Pima Copper Deposit, Pima Mining Co., Pima County, Ariz. United States Department of the Interior. Bureau of Mines, information circular 7822.

Tlas M., Asfahani J., 2011: Fair function minimization for interpretation of magnetic anomalies due to thin dykes, spheres and faults. J. Appl. Geophys., **75**, 2, 237–243, doi: 10.1016/j.jappgeo.2011.06.025.

Contributions to Geophysics and Geodesy Vol. 50/2, 2020 (201–221)

# Ambient radioactivity on a reconnaissance study tour of Bratislava – Dubai – Kathmandu – Nepal Himalaya

Andrej MOJZEŠ[1,*], Miroslav BIELIK[1,2], František MARKO[1], Ján MADARÁS[2], Kamil FEKETE[2], Pavol SIMAN[2], Juraj PAPČO[3], Ashok SIGDEL[4], Subash ACHARYA[4]

[1] Comenius University, Faculty of Natural Sciences, Ilkovičova 6, SK-84215 Bratislava, Slovak Republic

[2] Slovak Academy of Sciences, Earth Science Institute, Dúbravská cesta 9, SK-84005 Bratislava, Slovak Republic

[3] Slovak University of Technology, Faculty of Civil Engineering, Radlinského 11, SK-81005 Bratislava, Slovak Republic

[4] Tribhuvan University, Central Department of Geology, Kirtipur, Kathmandu 44618, Nepal

**Abstract:** Ambient radioactivity originates mainly from natural sources and materials (rocks and soils, building and other man-made materials, and cosmic radiation), and less frequently from artificial radionuclides. A geoscientific comparative study of the geological structure of the Alpine-Carpathian and Himalayan mountain range systems primarily focused on the area of structure geology, tectonics, stratigraphy and petrology in connection with the in-situ sampling of magnetic susceptibility and radioactivity at rock outcrops was also utilized to perform continual monitoring and acquisition of the equivalent gamma dose rate values in the air of the surrounding environment. A Geiger-Müller dosimeter was used for continual recording at a sampling frequency of 2 minutes. Simultaneously, a data-logger was used to record the ambient temperature, humidity and pressure values at a sampling frequency of 4 minutes. The measurements cover the entire tour, in particular, Bratislava, Slovakia (42.5 hours) – flight (5.75 hours) – Dubai, United Arab Emirates (11.3 hours) – flight (4 hours) – Kathmandu, Nepal (12.2 days) – flight (4.8 hours) – Dubai (9 hours) – flight (6.25 hours) – Bratislava (48 hours) from 27 March 2019 to 15 April 2019. The levels of ambient radioactivity belonging to different environments are compared and discussed in the contribution. The differences are based on both the chemical composition of the geological basement and adequate building materials and the cosmic contribution. The results of the measurements show higher values of ambient radioactivity for the Nepal environments and lower values for Dubai, in comparison with Bratislava, and by far the highest, but safe values for international flights attributed to the high portion of cosmic radiation. The contribution was generated within the ambit of the research project APVV-16-0146 WECAFARE (WEstern CArpathians FAults

*corresponding author: e-mail: andrej.mojzes@uniba.sk

doi: 10.31577/congeo.2020.50.2.2

REsearch) "Multidisciplinary research of the geophysical and structural parameters and environmental impacts of the faults of the Western Carpathians" thanks to the financial support of the Slovak Research and Development Agency.

**Key words:** applied geophysics, radioactivity, gamma dose rate, comparative geological study

## 1. Introduction

The instrumental data collection of physical properties of the geological environment creates the core of geophysical measurements and significantly contributes to its more complete cognition. That is also true for the case of the Western Carpathians faults research project under the name "Multidisciplinary research of the geophysical and structural parameters and environmental impacts of the faults of the Western Carpathians". The international cooperation of experts and an effort to correlate and update knowledge led to the realization of a multidisciplinary geoscientific comparative study of the geological structure of the Alpine-Carpathian and Himalayan mountain systems in the form of an intensive 9-day field research stay in the area of Nepal Himalaya. A structure-geological, tectonic, stratigraphic and petrologic investigation was also accompanied by in-situ sampling of magnetic susceptibility and radioactivity at rock outcrops and by collecting the small-volume rock samples. Moreover, regarding radioactivity measurement issues, the so-called continual monitoring and recording of the equivalent gamma dose rate values in the air of the surrounding environment during the 20-day stay on the tour Bratislava (Slovakia) – Dubai (United Arab Emirates) – Kathmandu (Nepal) – Nepal Himalaya – Kathmandu – Dubai - Bratislava was carried out. The issues of the analysis of the radioactivity rock outcrops were thus enlarged by problems of background radioactivity and the contribution of cosmic radiation during the plane flights themselves. This article provides an evaluation and comparison between ambient radioactivity during the constituent trip periods.

## 2. Study aim

The goals of study were:

– to carry out, as circumstances allowed, complete continual data collection

on radioactivity in the form of the equivalent gamma dose rate in the air during the entire tour, together with the ambient temperature, humidity and air pressure data;
- to process and evaluate such data in terms of their changes during the tour due to particular environmental differences;
- to compare the levels of ambient radioactivity and meteorological variables between constituent tour stages; and
- to try to identify and distinguish the sources of the changes of the measured variables during the tour.

The sources of the equivalent gamma dose rate in the air were natural radionuclides present in the surroundings, either the geological or generally natural environs, or in man-made materials (building, technological and other), where cosmic radiation presents a permanent contribution. To a lesser extent, it is not possible to rule out the presence of artificial radioactive sources. This article does not include a detailed analysis of the composition of radioactive sources (e.g. by the gamma-ray spectrometric measurement) or an evaluation of the results of the detailed sampling of the equivalent gamma dose rate at individual rock outcrops.

## 3. Methods and equipment

The continual measurements and data collection of the equivalent gamma dose rate in the air were carried out by dosemeter based on the Geiger-Müller detector at a recording frequency of 2 minutes. The GAMMA-SCOUT instrument with a registration and recording of gamma rays in an energy range of 0.03–3 MeV was used for measurement purposes.

The continual measurement and data collection of the ambient air temperature, humidity and pressure were carried out by the multifunction datalogger VOLTCRAFT THP180 at a recording frequency of 4 minutes.

## 4. Study areas and their geological settings

The measurements were taken continuously at the above-mentioned recording frequency on the Bratislava – Dubai – Kathmandu – Pokhara – Baglung – Kalopani – Kagbeni – Muktinath – Tukuche – Beni – Pokhara – Kath-

mandu – Dubai – Bratislava tour from 27 March 2019 to 15 April 2019 (20 days). The reconnaissance study on the mentioned tour itself (Fig. 1) lasted 16 days from 29 March 2019 to 13 April 2019, and the direct field geological research in the Nepal Himalaya along the line of the Kathmandu – Pokhara – Baglung – Kalopani – Kagbeni – Muktinath – Tukuche – Beni – Pokhara – Kathmandu geological transect (Fig. 2) lasted 9 days from 1 April 2019 to 9 April 2019.

Due to the length of the planned field geological profile, i.e. approx. 200 km of the Kathmandu – Pokhara leg and approx. 175 km of the Pokhara – Muktinath leg, the field survey was performed with the help of 2 field cars (9-member research team) in the form of numerous stops at selected localities along with walking examinations of geological objects.


Fig. 1. Illustration of the entire tour in the Google Earth application.

In terms of covered distance, there were two different means of transportation: air transport comprising of 4 international flights (Bratislava – Dubai and Dubai – Kathmandu, Kathmandu – Dubai, Dubai – Bratislava) with large distances (thousands of kilometres) covered in a relatively short time (hours) and car + walking transport (in Bratislava, Dubai and Nepal) with short distances (up to hundreds of kilometres in Nepal) covered in a substantially long time (days). For this reason, the next short geological characterization is given for those tour parts covered by car and foot only, i.e. the Bratislava and Dubai areas and the field study trail in the Nepal

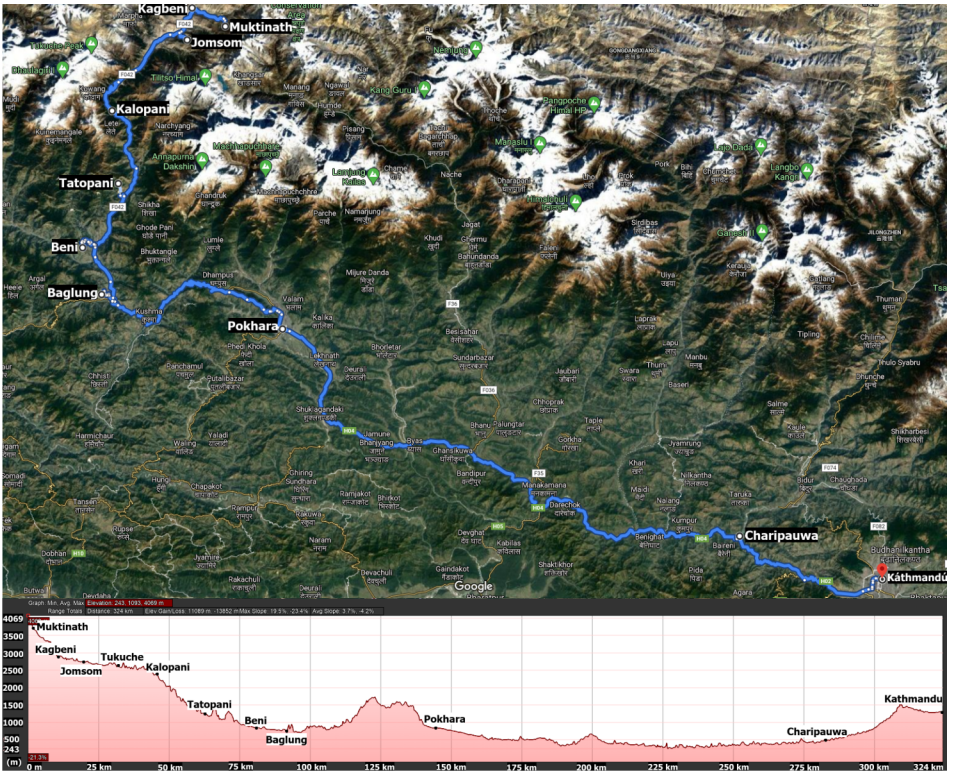


Fig. 2. Illustration of the field study geological transect (blue line) through the Nepal Himalaya and its height profile in the Google Maps and Google Earth applications.

Himalaya.

### 4.1. Bratislava (Slovakia)

The referred area of the eastern part of the city at the airport site is entirely comprised of Quaternary (the Late Pleistocene – Holocene) fluvial sediments (Fig. 3) in the form of lithofacially undivided alluvial clay soils and sandy to gravel soils (map index "fhh"), as well as sandy gravel and sand (map index "fš"). Postglacial deposits of alluvial sediments make up a substantial part of the fine-grained sedimentary surface cover of the sandy-gravel formation of the bottom accumulation of water flows (*Geological map of Slovakia 1:50 000, 2013*).

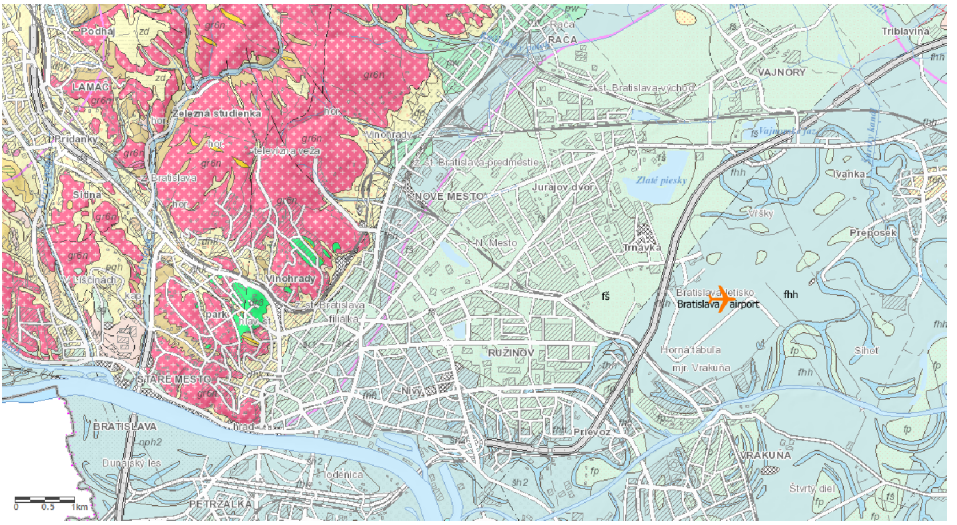


Fig. 3. Section of the geological map of the eastern part of Bratislava at the international airport localization (*Geological map of Slovakia 1:50 000, 2013*).

### 4.2. Dubai (United Arab Emirates)

The surface geology of the United Arab Emirates is concealed under a cover of sand (Fig. 4). Outcrops are confined only to the eastern part where the Oman Mountains form part of that region. The sands form dune ridges reaching heights of 150 m inland. Plain gravel areas – the so-called "desert floor", separate the dune ridges. Evaporatic flats (sabkha) dominate the coastal plains, which extend more than 80 km southwards into sand deserts. Consequently, the geology of this area is based exclusively on subsurface information (*Irani, 2001*).

Superficial deposits in the major urban areas in the emirates of Dubai, Sharjah and Ajman comprise the Quaternary fluvio-aeolian, aeolian and shallow marine deposits. Over much of the area, anthropogenic activity has resulted in the widespread deposition of made ground, including engineered fill. The Quaternary superficial deposits are underlain by variably calcareous and dolomitised sandstones, siltstones and conglomerates of the Barzaman Formation and weak mudstones, siltstones and gypsums of the Gachsaran Formation. In heavily urbanised areas, the extent of made

ground, the lack of exposure and the restricted nature of many of the site investigation reports means that the geological line-work was based on aerial photographs and satellite imagery taken prior to development (*Price et al., 2012*).

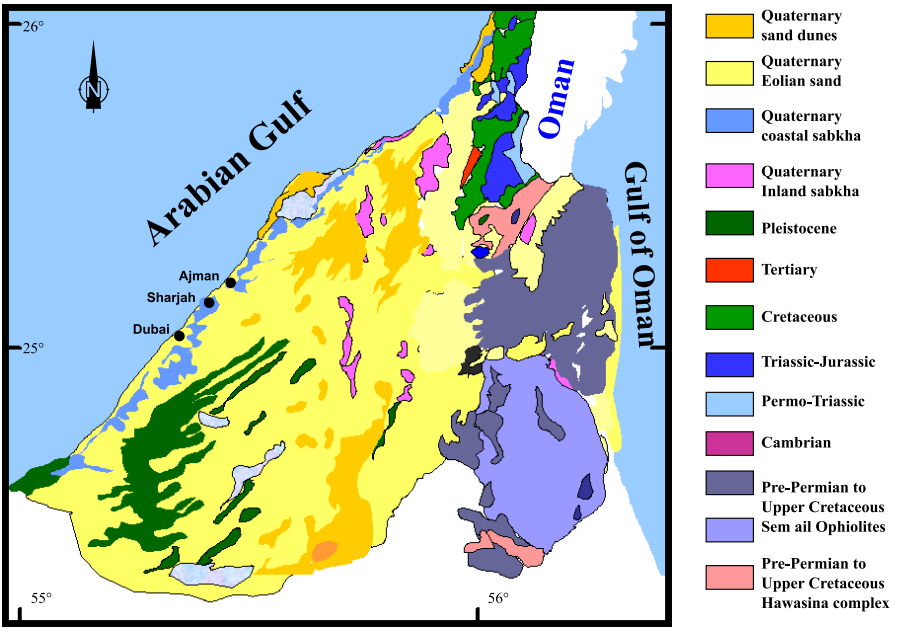


Fig. 4. Simplified geological map of the northern part of UAE (*Internet 1*, modified and *Internet 2*).

### 4.3. Kathmandu – Muktinath (Nepal)

The geological transect was very suitably selected considering the characteristic latitudinal features of the geological structure of Nepal with five fundamental NW–SE geological zones ranging from south to north in the following order: Terai and Bhabar Zone, Siwaliks and intermontane basins, Lesser Himalaya, Higher Himalaya and Tethys Himalaya (*Dhital, 2015*; Fig. 5). The first approximately 300 km-long part of the tour between Kathmandu and Beni followed a general NW–SE direction of geological units, which is why it runs mostly in the Lesser Himalaya zone, except for the first section – the approximately 70 km-wide Kathmandu surroundings with a compli-

cated geological structure of the Kathmandu Group belonging to the Higher Himalaya zone (Figs. 5, 6a). The Lesser Himalaya is basically composed of Proterozoic, mostly sedimentary (limestone, dolomite, shale and conglomerates) and low-grade metamorphic rocks (quartzites, phyllites, slates). The Kathmandu Group is composed mostly of Pre-Cambrian to Devonian metamorphic rocks (phyllites, micas and quartz schists, quartzites and sandstones) (Fig. 6b).

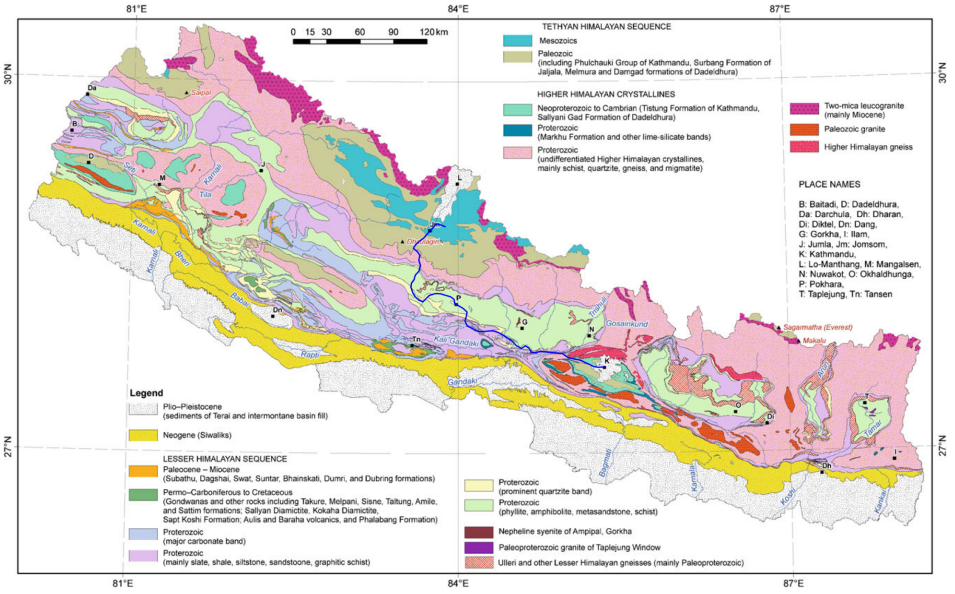


Fig. 5. Simplified geological map of Nepal (*Dhital, 2015*; supplemented by the blue line of the geological transect).

The second part of the tour between Beni and Muktinath (around 112 km) followed the Kali Gandaki River valley in a SSW–NNE direction across geological zones, and thus it cuts the Lesser Himalaya zone, the Main Central Thrust (MCT), the Higher Himalaya zone, the fault South Tibetan Detachment System (STDS) and ends in the Tethys zone (Muktinath) (Figs. 5,6a). The Lesser Himalaya zone is, intersected by the tour approximately in the part between Beni and Tatopani, and similar to the first part between Charipauwa and Beni, it is mostly composed of the Proterozoic low-grade metamorphic rocks (quartzites, phyllites, carbonaceous slates) and sedimentary rocks (green shales, compact dolomites, dolomitic limestones, sandstones


Fig. 6a. Section of the geological map of Nepal (*Himalayan Map House Pvt. Ltd., 2014*).


Fig. 6b. Legend of the geological map of Nepal (*Himalayan Map House Pvt. Ltd., 2014*).

and gritstones) (Fig. 6b). Generally, the grade of metamorphism increases from the foreland (south) to the hinterland (north) (*Dhital, 2015, p. 65*).

The Main Central Thrust (MCT) was intersected in the area of the village of Dana near Tatopani. This fundamental thrust structure repre-

sents the boundary between the underlying faintly metamorphosed Lesser Himalaya succession (south) and overlying Higher Himalayan crystallines (north) (*Dhital, 2015, p. 199*). The MCT comprises a wide zone of mylonitic rocks (fylonite) Proterozoic phyllites, quartzites and carbonates. The locally abundant presence of carbonate – quartzite veins and the remobilization of ferric oxides (limonitization), refers to fluid penetration in this zone. The increased seismicity, but also numerous natural thermal springs in the vicinity of the village of Tatopani (warm water in translation), also refer to recent activity of the tectonic zone.

The Higher Himalaya zone, between the villages of Tatopani and Kalopani, is composed of Proterozoic crystallines made up of medium to high-grade schists, quartzites and marbles together with augen and banded gneisses, migmatites and granites (*Dhital, 2015, p. 199*) (Fig. 6b). The Higher Himalayan crystallines are characterized by inverted metamorphism towards their base and a normal Barrovian type of metamorphism towards their top. The grade of metamorphism in the Higher Himalayan crystallines decreases progressively from the hinterland (north) towards the foreland (Siwaliks). Also, their metamorphic grade sharply diminishes towards the Tethyan sedimentary succession (*Dhital, 2015, p. 197*).

The Higher Himalayan crystallines are frequently truncated to the north by a system of normal faults called the South Tibetan Detachment System (STDS). This fault system was intersected in the area of the village of Kalopani. On the surface, the detachment is a discontinuous fault system with one or more splays. In some instances, it is represented by a shear zone (*Dhital, 2015, p. 197*). The South Tibetan Detachment System separates the medium to high-grade metamorphic rock of the Higher Himalaya from an overlying sedimentary or low-grade metamorphic secession of the Tethys Himalaya.

The last, most remote part of the tour between Kalopani – Jomsom – Kagbeni – Muktinath was in the Tethys Himalaya zone. The Tethyan Himalayan sequence mainly occupies the south periphery of the windswept Tibetan Plateau. The Tethyan rocks are made up of a variety of terrigenous and carbonate sediments, such as sandstones, siltstones, dolomites, limestones and shales (Fig. 6b). They range in age from Cambrian to Eocene. They are strongly folded and faulted, but conformably overlie the Proterozoic succession of the Higher Himalaya. Their grade of metamor-

phism generally increases from west to east. The Tethyan sediments have lateral changes and strong facies differences. The rocks are intricately folded and frequently verging due north, that is, opposite to the Higher and Lesser Himalayan successions. There are few Paleozoic remnants on top of the Higher Himalayan rocks (*Dhital, 2015, p. 285*).

## 5. Results and discussion

### 5.1. Overview

The results of the parallel recording of temperature, humidity and pressure of atmospheric air are presented in Fig. 7, while the overall results of ambient radioactivity recording on the Bratislava – Dubai – Nepal – Dubai – Bratislava reconnaissance study tour in the form of the equivalent gamma dose rate in the air from 27 March 2019 to 15 April 2019 are presented in Fig. 8. The graphs of the measured variables are presented in a time course, not a distance course. The changes in single variable courses are evident and easily readable in both figures and considering the fact that the path of the trips from Bratislava to Muktinath and back was almost identical; the curves are characterized by an almost mirror image with the centre in the most remote point of the tour – the Muktinath monastery and trekking ascent to the altitude of 4100 m a.s.l. in the Annapurna massif. This fact illustrates the satisfactory sensitivity of the instruments, the repeatability of their measurements and the stability of the meteorological conditions during the entire tour.

### 5.2. Meteorological parameters

From among the meteorological variables (Fig. 7), barometric pressure bears the highest information value as temperature and humidity were often influenced by the datalogger placement in baggage, the means of transportation or the indoor environment in dwellings.

The overall barometric pressure course (Fig. 7) reliably documents the dependence on altitude. Although altitude was not recorded, the pressure curve shows an evident difference between the low-lying regions of Bratislava (around 130 m a.s.l.) and Dubai (around 15 m a.s.l.) and the mountainous areas of the Nepal Himalaya. Also, the periods of four international

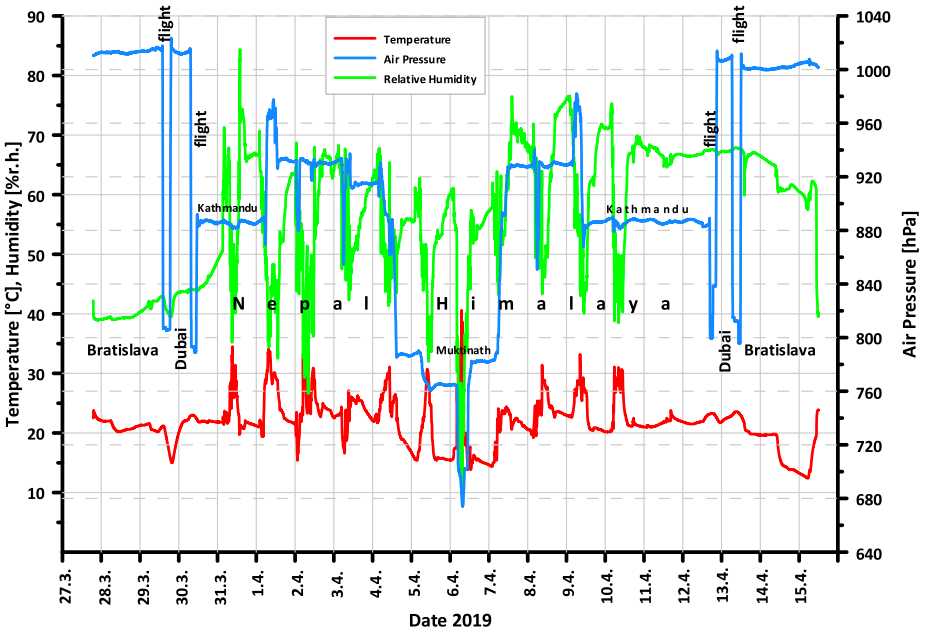


Fig. 7. Time course of meteorological parameters logged during the entire trip.

flights (Bratislava – Dubai, Dubai – Kathmandu and back) can be sharply distinguished, even if their expressive pressure minima at a flight altitude of about 10000 m a.s.l. has higher values than the lowest pressure minimum achieved during the trekking ascent to an altitude of 4100 m a.s.l. (in the middle of the curve in Fig. 7). This is due to overpressure conditions in the aircraft. Equally, there are easily identified areas in Nepal itself on the barometric pressure course (Figs. 7–9), e.g. the higher-lying Kathmandu plateau (around 1600 m a.s.l.), and the low-lying river valleys (around 300 m a.s.l.) on the road leading from Kathmandu to Pokhara, as well as the depression at Pokhara itself (around 1000 m a.s.l.) and the nearby lake (Fig. 2). From there, the gradual ascent follows up the Kali Gandaki River valley between the Dhaulagiri and the Annapurna massifs to the Muktinath monastery (around 3800 m a.s.l.) at the Upper Mustang border and to the altitude point of 4100 m a.s.l. below the Thorung La Pass (5416 m a.s.l.). The crossings of the deep valleys of the Trishuli and Marsyangdi rivers (around 300 m a.s.l.) on the road between Kathmandu and Pokhara, and the crossings of

mountain ranges, e.g. on the road between Pokhara and Baglung (around 1800 m a.s.l.) as well as the ascent to the Sarangkot observation hill (around 1590 m a.s.l.) near Pokhara are detected on the barometric pressure curve.

The basic statistical characteristics of the meteorological parameters for individual destinations and environments are presented in Table 1.

Table 1. Basic statistical characteristics of meteorological parameters for single destinations and environments.

| | No. of measurements (à 4 min) | Minimum | Maximum | Mean | Standard deviation | Coefficient of variation |
|---|---|---|---|---|---|---|
| TEMPERATURE (°C) | | | | | | |
| Bratislava (Slovakia) | 1359 | 12.4 | 23.9 | 19.2 | 2.0 | 0.11 |
| Dubai (United Arab Emirates) | 321 | 15.0 | 22.9 | 21.2 | 1.5 | 0.07 |
| Nepal | 4750 | 13.8 | 40.6 | 22.3 | 3.8 | 0.17 |
| aircraft flights | 304 | 15.3 | 23.6 | 22.0 | 0.7 | 0.03 |
| HUMIDITY (% r.h.) | | | | | | |
| Bratislava (Slovakia) | 1359 | 38.9 | 67.5 | 51.4 | 2.9 | 0.05 |
| Dubai (United Arab Emirates) | 321 | 39.5 | 67.5 | 55.2 | 0.7 | 0.02 |
| Nepal | 4750 | 9.8 | 84.4 | 58.1 | 10.6 | 0.18 |
| aircraft flights | 304 | 39.5 | 67.9 | 55.0 | 0.4 | 0.01 |
| AIR PRESSURE (hPa) | | | | | | |
| Bratislava (Slovakia) | 1359 | 999.6 | 1017.8 | 1007.6 | 1.5 | 0.002 |
| Dubai (United Arab Emirates) | 321 | 1000.9 | 1023.6 | 1010.3 | 1.6 | 0.002 |
| Nepal | 4750 | 673.9 | 982.1 | 878.1 | 60.5 | 0.07 |
| aircraft flights | 304 | 788.9 | 1012.2 | 828.8 | 50.6 | 0.06 |

### 5.3. Equivalent gamma dose rate

The overall equivalent gamma dose rate course (Fig. 8) reflects changes in the ambient radioactivity of the studied destinations. Besides the natural gamma radiation of the surrounding geological and non-geological environment, its the most important component is the gamma component of cosmic radiation. These radioactivity components could not be separated by the

instruments that were used.

Based on the overall curve, it can be concluded that the lowest values of the equivalent gamma dose rate are connected with the Dubai environment, where they are bound to large complexes of the Quaternary sandy cover formations (*Price et al., 2012*), with the typically low content of radioactive elements (*IAEA, 1990*), as well as to the low contribution of cosmic radiation in consideration of the very low altitude of around 15 m a.s.l. (*IAEA, 1990*).

The higher values of the equivalent gamma dose rate are valid for the region of Bratislava near its airport. This area is composed of Quaternary clayey cover (*Geological map of Slovakia 1:50 000, 2013*) with a higher content of a generally more radioactive clay component (*IAEA, 1990*); but it also lies at a higher altitude (around 130 m a.s.l.), with an appropriately higher degree of cosmic radiation (*IAEA, 1990*) in comparison with Dubai.

Even higher values of the equivalent gamma dose rate were registered

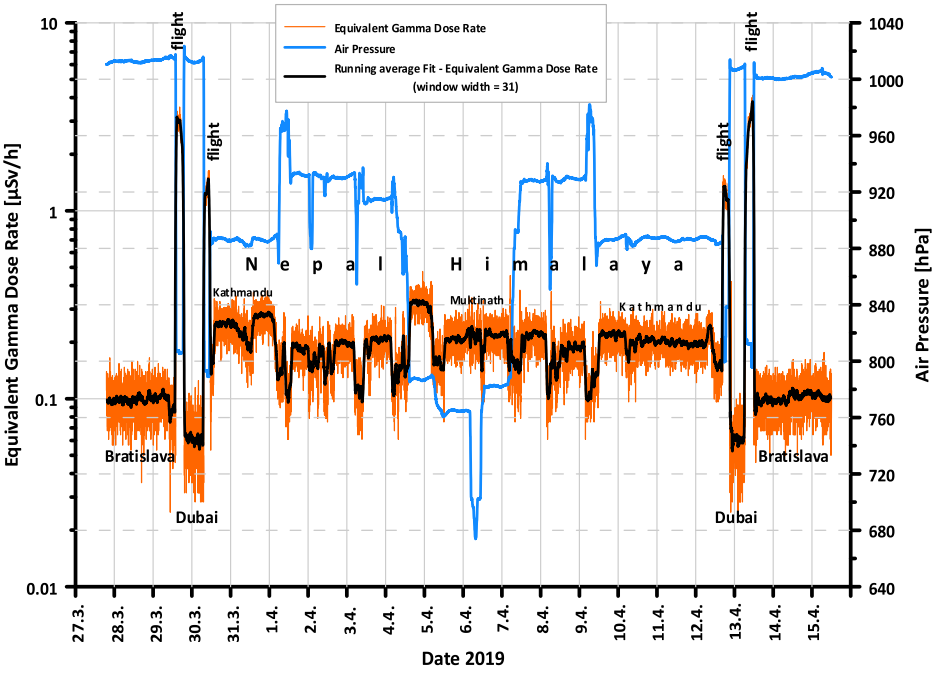


Fig. 8. Overview of the equivalent gamma dose rate and barometric pressure courses during the entire trip.

along the study transect through the Nepal Himalaya, where on one hand the surrounding mountain environment is comprised to a great extent by parent rocks and their fresh weathered cover with a possibly higher content of radionuclides, while on the other hand the contribution of cosmic radiation is even higher as a result of the high average altitude (*IAEA, 1990*).

The highest values by far of the equivalent gamma dose rate were detected during four international aeroplane flights (Bratislava – Dubai, Dubai – Kathmandu and back) with the highest degree of cosmic radiation at altitudes of around 10000 m a.s.l.

The basic statistical characteristics of the equivalent gamma dose rate for individual destinations and environments are presented in Table 2.

Table 2. Basic statistical characteristics of the equivalent gamma dose rate for individual destinations and environments.

| | No. of measurements (à 2 min) | Minimum ($\mu$Sv/h) | Maximum ($\mu$Sv/h) | Mean ($\mu$Sv/h) | Standard deviation ($\mu$Sv/h) | Coefficient of variation |
|---|---|---|---|---|---|---|
| Bratislava (Slovakia) | 2 715 | 0.025 | 0.176 | 0.099 | 0.020 | 0.199 |
| Dubai (United Arab Emirates) | 637 | 0.025 | 0.097 | 0.061 | 0.022 | 0.349 |
| Nepal | 9 502 | 0.053 | 0.476 | 0.199 | 0.055 | 0.279 |
| aircraft flights | 611 | 0.057 | 4.126 | 1.733 | 0.745 | 0.419 |

### 5.4. International flights and the equivalent gamma dose rate

The highest values of the equivalent gamma dose rate were registered during four international flights as a result of the high contribution of cosmic radiation at flight altitudes of around 10000 m a.s.l. The detector was placed in the luggage compartment of aeroplane during the entire flight time. The maximum value (4.126 $\mu$Sv/h) and average value (1.733 $\pm$ 0.745 $\mu$Sv/h) of the equivalent gamma dose rate during flights (Table 2) comply with official data stated by aircraft crews for flights at altitudes of up to 16500 m (*EURADOS WG5, 2004*), monitored from 1992 to 2003, with an average value of $3.8 \pm 0.8$ $\mu$Sv/h, the most frequent measured value of $2.5 \pm 0.5$ $\mu$Sv/h and the maximum value of 19.2 $\pm$ 12.4 $\mu$Sv/h. The probable reason for the lower values in our case was the registration of gamma radiation only, while

in the case of the EURADOS study, the complex sun and galactic cosmic radiation was a subject of interest (*EURADOS WG5, 2004*). In terms of safety and protection against radiation, the mean value of the effective dose obtained during the overall flight time (20.8 hours) at the level of 0.036 mSv (1.733 $\mu$Sv/h $\times$20.8 h = 36 $\mu$Sv = 0.036 mSv) was absolutely safe as one would have to undergo at least 300 flight hours at altitudes of over 9144 m in the equatorial zone (*Beck et al., 2006*), where our flights were undertaken to achieve the limit of the annual effective dose valid for the population at the level of 1 mSv/year (*Council Directive 2013/59/EURATOM, 2014*).

### 5.5. The Nepal Himalaya environment

On the basis of a more detailed view of the time course of the equivalent gamma dose rate (Fig. 9) and the barometric pressure (Figs. 7, 9), it is possible to state that these variables also depict some environmental changes within transfers in the Nepal Himalaya area itself (Fig. 2).

Considering the fact that the measured variables are presented in a time course and not a distance course, the longer one stays in one place (usually in accommodations) form the more relatively stable parts, where the values oscillate around the mean value, while car transfers to other accommodation places, usually accompanied by short stops at geologically interesting localities and outcrops, appear as shorter parts of lowered and less stable values of the equivalent gamma dose rate.

Repeated stays in some places, e.g. in the Kathmandu and Pokhara regions (on the way there and back), show approximately the same levels of the equivalent gamma dose rate. It is more evident for the Pokhara area (on average 0.178 $\mu$Sv/h on the way there versus 0.177 $\mu$Sv/h on the way back), than for the Kathmandu area (on average 0.242 $\mu$Sv/h on the way there versus 0.201 $\mu$Sv/h on the way back), where the equivalent gamma dose rate values increased significantly (up to 0.375 $\mu$Sv/h) during the first stay during and after a strong thunderstorm on 31 March 2019 as a result of radon gas washing from the atmosphere to the earth's surface (Fig. 9). This rainstorm is documented by the highest measured values of air humidity (up to 84.4% r.h.) during the entire trip (Fig. 7). This was the only single, unstable meteorological event during the entire trip. The well-marked decrease of the equivalent gamma dose rate values immediately before the storm (to

the level of 0.115 $\mu$Sv/h) was probably caused by the composition of building material in the vicinity of Durbar Square in the centre of Kathmandu (Fig. 9). The higher average values of the equivalent gamma dose rate in the Kathmandu region (0.222 $\mu$Sv/h) in comparison with the Pokhara region (0.178 $\mu$Sv/h) could have been due to the commonly higher radioactivity of the Pre-Cambrian to Devonian metamorphites (phyllites and shales) of the Higher Himalaya's Kathmandu Group, while the Pokhara area is comprised of Proterozoic, mostly sedimentary rocks (limestones, dolomites) and low-grade metamorphed rocks (quartzites) of the Lesser Himalaya sequences, with commonly low radioactivity.

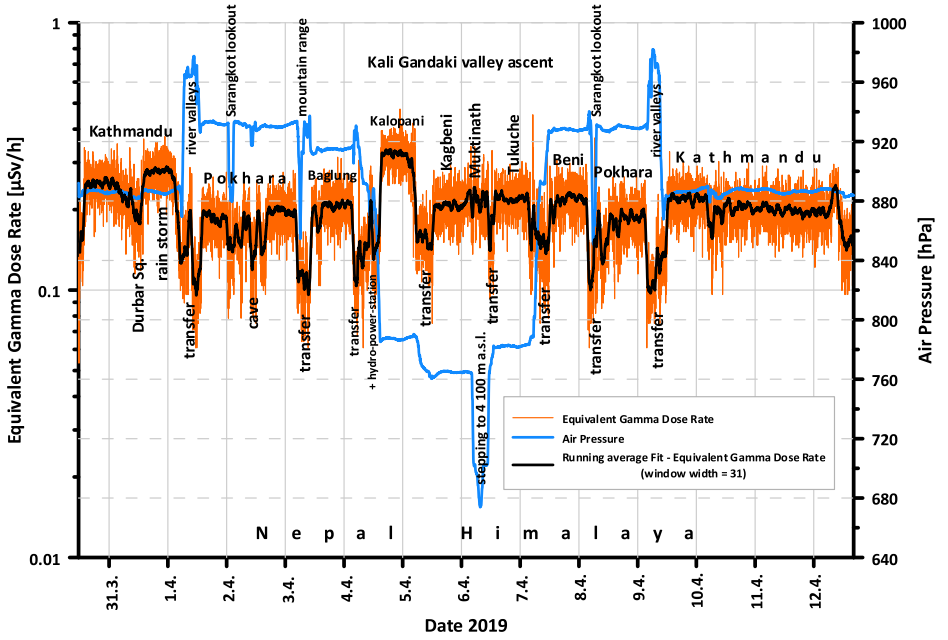


Fig. 9. Time courses of the equivalent gamma dose rate and barometric pressure in detail for the Nepal Himalaya part.

The transfer from the Kathmandu plateau to the Pokhara depression and back is indicated by short but distinct decreases in barometric pressure values (Figs. 7–9) when crossing the mountain range encircling Kathmandu, followed by stages of expressive increases in barometric pressure values when travelling along the deep valleys of the Trishuli, Marsyangdi and Seti Rivers

on the way to Pokhara.

In a similar way, due to the sharp minima of barometric pressure (Figs. 7–9), the ascents to Sarangkot lookout hill site (1590 m a.s.l.) in the Pokhara area, as well as the crossings of the mountain range on the way from Pokhara to Baglung (around 1800 m a.s.l.) are also indicated.

Starting from Pokhara, a sequential decrease of barometric pressure is recorded in connection with the gradual ascent following the Kali Gandaki River valley between the Dhaulagiri and the Annapurna massifs up to its lowest value of 673.85 hPa at the highest point – the Muktinath monastery (around 3800 m a.s.l.) and the altitude of 4100 m a.s.l. below the Thorung La Pass (5416 m a.s.l.).

The Baglung surroundings are also comprised of rock sequences of the Lesser Himalaya zone with an average equivalent gamma dose rate value (0.202 $\mu$Sv/h) near the Pokhara area.

The section of lower equivalent gamma dose rate values (on average 0.145 $\mu$Sv/h), belonging to the transfer from Baglung to Kalopani, contains a peak of higher values (on average 0.291 $\mu$Sv/h) obtained during the guided tour of the inflow underground tunnel of the hydroelectric power station of the Mistri Khola Hydroelectric Project.

After crossing the Main Central Thrust (MCT) zone in the area of the village of Dana (Figs. 2 and 6a) the geological surroundings are formed by the Neo-Proterozoic rocks of the Higher Himalaya zone, which are represented by mica-schists alternating with banded gneisses, migmatites and granites showing the highest equivalent gamma dose rate values (maximally up to 0.476 $\mu$Sv/h, on average 0.343 $\mu$Sv/h) in the section of the villages of Tatopani, Dana and Kalopani.

After crossing the tectonic boundary of the South Tibetan Detachment System (STDS) between the villages of Kalopani and Larjung, the Tethyan Himalayan sequence of terrigenous and carbonate sediments such as sandstones, siltstones, dolomites, limestones and shales starts and continues further to the north. These rocks form the highest mountain peaks in the surroundings (Dhaulagiri – 8167 m a.s.l., Tukuche Peak – 6920 m a.s.l., Annapurna – 8091 m a.s.l., Nilgiri – 7061 m a.s.l., Tilicho Peak – 7134 m a.s.l. and others). The most remote points of the tour – the Muktinath monastery and the mountain stepping to 4100 m a.s.l. also lay in this geological environment. Sedimentary rocks show lower values of the dose equivalent rate

in the Kagbeni area (on average 0.210 $\mu$Sv/h) and Muktinath (on average 0.223 $\mu$Sv/h) as well as in the Tukuche area (on average 0.221 $\mu$Sv/h) on the way back from Muktinath.

The part with the highest measured equivalent gamma dose rate values (Kalopani – Dana – Tatopani) of the Higher Himalaya rocks did not show higher values on the way back. This was probably due to the fast vehicle transport, despite the fact that the short measurements at orthogneiss outcrops showed high equivalent gamma dose rate values (up to 0.453 $\mu$Sv/h).

The Beni area again formed by rock sequences of the Lesser Himalaya zone showed the same equivalent gamma dose rate values (on average 0.217 $\mu$Sv/h) as in nearby Baglung (0.202 $\mu$Sv/h).

## 6. Conclusions

The recording measurements of ambient radioactivity in the form of the equivalent gamma dose rate in the air taken on the tour dedicated to the reconnaissance comparative study of the Alpine-Carpathian and Himalayan mountain range systems on the way from Bratislava (Slovakia) – Dubai (United Arab Emirates) – Kathmandu (Nepal) – Nepal Himalaya and back showed the presence of different equivalent gamma dose rate levels between particular destinations and environments and the possibility of the registration of their changes by the above-mentioned instruments. The differences were based on both the composition of the natural environment (geological and non-geological), and the varying contribution of cosmic radiation depending on altitude. The lowest registered equivalent gamma dose rate values were recorded in the Dubai environment (UAE); a higher equivalent gamma dose rate values were recorded in the Bratislava region (Slovakia) and even higher values of the entire study geological transect were recorded in the Nepal Himalaya environment. By far the highest equivalent gamma dose rate values were registered during the four international aeroplane flights at high altitudes; however, the effective dose value did not exceed the obligatory limits for safe exposure of the common population. The results confirm the generally known facts about the dependence of cosmic radiation growth on altitude increase, and the growth of geological environment radioactivity in the following sequence: sandy formations – clayey formations – weathered and non-weathered sequences of parent rocks.

***Acknowledgements***. The authors are grateful for the support by the Slovak Research and Development Agency APVV under grant APVV-16-0146 and APVV-15-0050. This work was supported also by the Slovak Grant Agency VEGA, under grant 2/0006/19. The Slovak authors are also very grateful for the accompanying support by Assist. Prof. Ashok Sigdel and Dr. Subash Acharya from the Central Department of Geology, Tribhuvan University, Kathmandu.

## References

Beck P., Bartlett D., Lindborg L., McAulay I., Schnuer K., Schraube H., Spurný F., 2006: Aircraft crew radiation workplaces: comparison of measured and calculated ambient dose equivalent rate data using the Eurados in-flight radiation database. Radiat. Prot. Dosim., **118**, 2, 182–189, doi: 10.1093/rpd/ncl029.

Council Directive 2013/59/EURATOM of 5 December 2013 stipulating the basic safety standards for protection against the dangers arising from exposure to ionising radiation. Official Journal of the European Union, L 13/1, 17. 1. 2014, 73 p.

Dhital M. R., 2015: Geology of the Nepal Himalaya. Springer, 498 p.

EURADOS WG5, 2004: Cosmic radiation exposure of aircraft crew. Compilation of measured and calculated data. Final report. Radiation Protection, Issue 140, Luxembourg, 271 p., online, available at http://europe.eu.int.

Geological map of Slovakia 1:50 000, 2013: State Geological Institute of Dionýz Štúr, Bratislava, online, available at http://apl.geology.sk/gm50js on 13. 1. 2020.

Himalayan Map House Pvt. Ltd., 2014: The Geological Map of Nepal, 1:1 000 000.

IAEA, 1990: The Use of Gamma Ray Data to Define the Natural Radiation Environment. IAEA-TECDOC-566, Vienna, 48 p.

Internet 1: Geology of Emirates. Available at http://www.angelfire.com/az3/mohgameil/emirates.html on 13. 1. 2020.

Internet 2: United Arab Emirates, Ministry of Energy and Industry, Geology and Mineral Resources Department: Geological Passport, Abu Dhabi. Available at https://www.moei.gov.ae/assets/9ad782cf/geological_passport.aspx on 13.1.2020.

Irani F. N., 2001: Geology of the United Arab Emirates. Schlumberger Drilling and Measurements, Abu Dhabi, 143 p.

Price S. J., Farrant A. R., Thomas R. J., Ellison R. A., 2012: Geology of the Dubai, Sharjah and Sir Bu N'Air 1:100 000 map sheet, 100–5, United Arab Emirates. Nottingham, UK, British Geological Survey, 54 p.

Contributions to Geophysics and Geodesy Vol. 50/2, 2020 (223–247)

# A regional Stokes-Helmert geoid determination for Costa Rica (GCR-RSH-2020): computation and evaluation

Jaime GARBANZO-LEÓN[1,*], Alonso VEGA FERNÁNDEZ[1], Mauricio VARELA SÁNCHEZ[1], Juan Picado SALVATIERRA[1], Robert W. KINGDON[2], Oscar H. LÜCKE[3]

[1] School of Surveying Engineering, University of Costa Rica

[2] School of Geodesy and Geomatics Engineering, University of New Brunswick

[3] Central American School of Geology of the University of Costa Rica

**Abstract:** GNSS observations are a common solution for outdoor positioning around the world for coarse and precise applications. However, GNSS produces geodetic heights, which are not physically meaningful, limiting their functionality in many engineering applications. In Costa Rica, there is no regional model of the geoid, so geodetic heights ($h$) cannot be converted to physically meaningful orthometric heights ($H$). This paper describes the computation of a geoid model using the Stokes-Helmert approach developed by the University of New Brunswick. We combined available land, marine and satellite gravity data to accurately represent Earth's high frequency gravity field over Costa Rica. We chose the GOCO05s satellite-only global geopotential model as a reference field for our computation. With this combination of input data, we computed the 2020 Regional Stokes-Helmert Costa Rican Geoid (GCR-RSH-2020). To validate this model, we compared it with 4 global combined geopotential models (GCGM): EGM2008, Eigen6C-4, GECO and SGG-UM-1 finding an average difference of 5 cm. GECO and SGG-UM-1 are more similar to the GCR-RSH-2020 based on the statistics of the difference between models and the shape of the histogram of differences. The computed geoid also showed a shift of 7 cm when compared to the old Costa Rican height system but presented a slightly better fit with that system than the other models when looking at the residuals. In conclusion, GCR-RSH-2020 presents a consistent behaviour with the global models and the Costa Rican height systems. Also, the lowest variance suggests a more accurate determination when the bias is removed.

**Key words:** heights, geoid, gravity, Stokes-Helmert approach, Costa Rica

## 1. Introduction

GNSS observations are a common solution for outdoor positioning around

*corresponding author: e-mail: jaimegarbanzo@gmail.com

the world and are used for height determination in other mapping techniques such as photogrammetry and LiDAR. The latitude and longitude are determined accurately by GNSS for precise applications, but the orthometric heights for some science and engineering applications can only be determined if geoid heights are also available in the area of interest. A geoid height ($N$) is the correction needed for the geodetic height from GNSS to be transformed to the orthometric height ($H$). The quantity $N$ is the height of the geoid reference surface above the reference ellipsoid. Thus, the accurate computation of the geoid is of great importance in the development of a region. Until today, there is no official determination of a geoid for Costa Rica and the $H$ determination had to rely in global geoid models, which have a low spatial resolution and lack the contributions of high density ground based gravity stations to the high frequency gravity spectrum since the ground data in global models is gridded and decimated. This paper shows the efforts of the University of Costa Rica to provide a valid and traceable solution to this problem. This project also had the support of the University of New Brunswick, which allows the computation of a geoid using the Stokes-Helmert technique developed in this institution.

First, this document shows a literature review some of the efforts made for the geoid determination. Next, we describe some of the developments achieved in satellite gravity modelling and the Stokes-Helmert technique. After that, we discuss the land gravimetric campaigns of the historic gravity databases available for the computation. We explain in the method section the data quality testing for land and marine gravity data, the basis of the Stokes-Helmert Technique, the gravity interpolation process, and other parameter choice for the computation. Finally, we focus on the comparison between the global geoid models (GGM) and the computed geoid, and validation using 25 GNSS points associated with vertical benchmarks. This last validation suggests that the computed geoid describes the reference surface in Costa Rica better than the global geoid models.

## 2. Literature review

In Costa Rica, there have been few attempts to compute a regional geoid model (*Cordero Gamboa, 2010; Moya Zamora and Dörries, 2004*). More recently, *Varela Sánchez (2018)* computed a regional gravimetric geoid using

historical databases provided by the National Geographic Institution (IGN). However, these gravimetric databases do not contain detailed comprehensive compilation of all the available historical data and did not include a rigorous quality assessment and outlier removal process. Also, marine and satellite altimetry data were not included in the computation.

Gravity studies in Costa Rica began since 1916 for oil and gas prospecting (*Ballestero et al., 1995*). The first published data is from 1958 (*Monges, 1958*). The International Gravity Standardization Network (IGSN71) included 2 points (Point # 00994K and 00994L) in the country (*Morelli et al., 1972*), which served as reference points for densification, but these points are now destroyed. Also, geophysical studies have been a provider of gravity values, including those from *de Boer (1974), Barritt and Berrangé (1987), Gurney (1997)* and many others. This data is accumulated in different databases, which sometimes are duplicated, and its quality is not checked. For example, Institutions such as the Bureau Gravimetrique International (BGI) and the National Geospatial Intelligence Agency of the United States (NGA) hold large amounts of terrestrial and marine data, which must be thoroughly filtered. Most recently, New high quality terrestrial gravity data is being acquired, for example by *Lücke (2018)* and *Denyer et al. (2019)*. The variety of datasets requires paying special attention on the interpolation approach.

The fundamental theory behind the Stokes-Helmert approach of performing the Stokes integration in the Helmert space was introduced by *Vaníček and Kleusberg (1987)*. Since this time, the approach is being perfected through a series of improvement to provide a very accurate determination of a gravimetric geoid (*Foroughi et al., 2019; Kingdon and Vaníček, 2011; Tenzer et al., 2003a; Tenzer et al., 2003b*). Modern testing of the approach had been done in the last years. For example, *Janák et al. (2017)* demonstrated than when the approach is correctly applied the computed geoid is of the same or perhaps better accuracy than the results of other techniques. Furthermore, *Foroughi et al. (2017)* provide an assessment on the optimal combination of satellite data and terrestrial data and most recently they showed new advances on the algorithm for downward continuation using Least Squares and showed the likelihood of obtaining a sub-centimetric geoid (*Foroughi et al., 2019*). All these findings and developments assure a very precise geoid determination using the Stokes-Helmert approach. In the

current work, the improvements carried out by *Foroughi et al. (2019)* were not included because of the time period of this project.

## 3. Theory and methods

The importance of gravity in height determinations is well-known. For example, we can find this effect when surveying with an automatic level (A-level). Spirit levelling is the simplest and most accurate technique for height determination. Basically, height differences are measured from point (A) to another point (B). If the gravity measurements are not performed when surveying with this technique, the heights will contain a systematic error due to non parallelism of the equipotential gravity surfaces, and the height differences obtained are only an approximation of the real change in orthometric heights – see *Hofmann-Wellenhof and Moritz (2006)*. Fig. 1 illustrates this situation with a little exaggeration; the subtraction of the reading (Bs-R − Fs-R) is not equal to the same operation using the differences in orthometric heights ($\Delta Ha - \Delta Hb$).

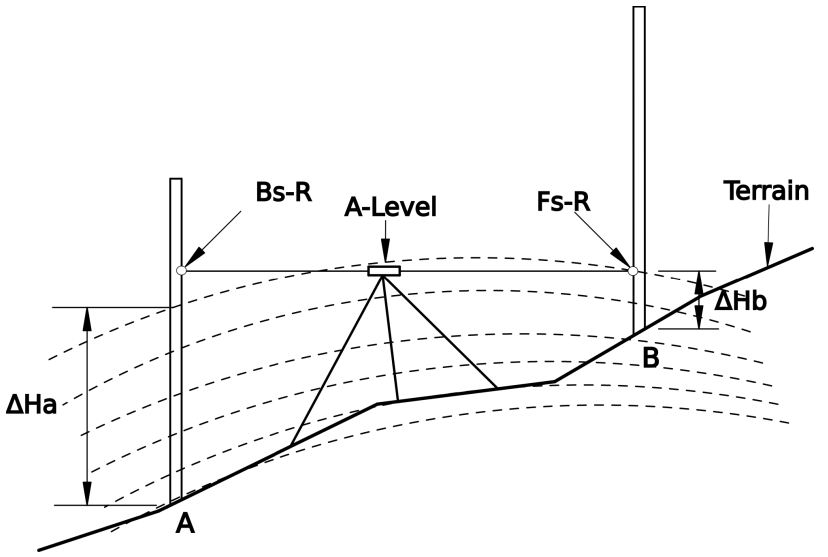


Fig. 1. The difference between the Bs-R and $\Delta Ha$ illustrates the problem of physical height determination.

To have a consistent national height system, all benchmarks (BM) must be referred to a common equipotential surface (a geoid). This is a complex situation because the survey lines run on the surface of topography while the geoid most of the time remains under the topographical surface. The situation can only be resolved with knowledge of the topographical density distribution, which has split the geodetic community over how to define a height reference surface (*Vaníček et al., 2012*).

As an alternative to spirit levelling, one can determine the geodetic height ($h$) using GNSS observations. This h is a geometric quantity representing a straight line from a reference ellipsoid to the point of interest. The more useful orthometric height ($H$) is a physically meaningful height of a point above the geoid and is measured along a curved plumbline from the geoid to the surface (*Hofmann-Wellenhof and Moritz, 2006*). Apart from the obvious differences between them, h may be considered a coarse approximation of the orthometric height that can be converted to H by a transformation, called the geoid-ellipsoid separation N; Eq. (1) shows the relationship between the different heights:

$$H = h - N\,. \tag{1}$$

## 4. The disturbing potential and its relationship to the geoid

The disturbing potential ($T$) on the geoid is the difference between the actual gravity potential ($W$) and the normal gravity potential ($U$) at the same point (*Heiskanen and Moritz, 1967*). $N$ can be determined by means of Brun's formula if T is known on the geoid ($T_G$) (Eq. (2) and Eq. (3)):

$$T_G = W_G - U_G\,, \tag{2}$$

$$N = \frac{T}{\gamma} + \frac{W_0 - U_0}{\gamma}, \tag{3}$$

$W_0$ and $U_0$ are the geoid and the ellipsoid reference equipotential values. $\gamma$ represents the normal gravity value on the ellipsoid.

If $W_0$ is set to be equal to $U_0$, the second term in Eq. (3) becomes 0, and the computation is simplified. As $W_G$ is the potential on the geoid is also the same as $W_0$.

## 5. The UNB Stokes-Helmert approach

The Stokes-Helmert approach has been described thoroughly by *Ellmann and Vaníček (2007)* and a series of other publications. Here, we provide a summary of the main concepts.

Stokes' integral (*Stokes, 1849*) may be used to calculate the disturbing potential on the geoid surface, using gravity anomalies provided on the geoid surface. The process of transforming anomalies values on the surface to the geoid is called downward continuation (DWNC) and the gravity values outside the geoid must be harmonic to perform DWNC correctly. If the gravity anomaly values ($\Delta g$) are multiplied by the point's distance to the center of the Earth ($r$), the term $r\Delta g$, which is harmonic (*Huang, 2002*), can be introduced in the Poisson's integral to obtain the downward continued $\Delta g$.

Inside the topographic masses the gravity potential field is not harmonic. Thus, Helmert's second condensation method is applied to allow downward continuation in this domain. In this method, the Earth's topographic and atmospheric masses are condensed to a thin layer on the geoid, transforming the gravity values to the Helmert space (see *Janák et al. (2017)* and *Ellmann and Vaníček (2007)* for more information). The Stokes' integral (Eq. 4) may then convert the downward continued gravity anomalies into disturbing potential ($T$) and a geoid height ($N$) may be determined, and ultimately transformed from the Helmert space, back into the real space:

$$N = \frac{R}{4\pi\gamma_m} \iint S(\psi) * \Delta g \, \mathrm{d}\sigma \,, \tag{4}$$

where $R$ is the semimajor axis of the reference ellipsoid, $\gamma_m$ the mean normal gravity value, $S(\psi)$ the Stokes' kernel and $\Delta g$ is the gravity anomaly (*Torge and Müller, 2012*).

## 6. The process of geoid computation

In addition to the main steps described so far in this document, a geoid computation involves numerous small details, which can lead to an incorrect result if neglected (see *Janák et al. (2017)*). Thus, to perform the computation, the researcher must thoroughly study the technique. The first step is to compute the Helmert gravity anomalies ($\Delta g^H$), which are required to

compute the disturbing potential and so the geoid. $\Delta g^H$ is well approximated by the widely available free-air gravity anomaly, $\Delta g^{FA}$ (*Heiskanen and Moritz, 1967*). Thus, the process of a geoid computation starts with the free-air gravity anomaly. A series of transformations must be applied to compute the $\Delta g^H$ values such as the direct topographical (DTE) and atmospheric (DAE) effects, the secondary topographical effect (SITE), and the geoid-quasigeoid correction (G-QG). Furthermore, the Helmert gravity anomalies must be downward continued to the geoid. These processes may be represented as:

$$\Delta g^{FA}(r_t, \Omega) \rightarrow \Delta g^H(r_t, \Omega)\,, \tag{5}$$

$$\Delta g^H(r_t, \Omega) \rightarrow \Delta g^H(r_g, \Omega)\,. \tag{6}$$

*Vaníček and Sjöberg (1991)* introduced the idea of splitting the determination of geoid heights in two parts. This idea allows combination of satellite and ground gravity techniques to obtain a more accurate solution, because satellite geopotential modelling describes the long wavelength of the gravity potential field using spherical harmonics coefficients, more accurately than ground measurement techniques. Thus, an accurate geoid determination must include satellite measurements. Consequently, the satellite-based Helmert anomalies $\Delta g^H_{sat}$, represented by a spherical harmonic series to low (e.g. 160) degree and order are subtracted from, producing a residual Helmert gravity anomaly $\Delta g^H_{res}$:

$$\Delta g^H_{res} = \Delta g^H - \Delta g^H_{sat}\,, \tag{7}$$

where $\Delta g^H_{sat}$ is computed using a global geopotential model.

A residual cogeoid height $N^H_{res}$, is obtained from application of Stokes' integral using $\Delta g^H_{res}$, and $N^H_{sat}$ is computed using global geopotential models (GGM). Then, the full geoid heights are found using:

$$N^H = N^H_{res} + N^H_{sat}\,. \tag{8}$$

The cogeoid quantity is the result of applying the Stokes' integral to the downward continued data, and it is not a geoid because the effects of the compression of the atmospheric and topographic masses has to be restored. In other words, these quantities are still in the Helmert space; thus, the

primary indirect topographic (PITE) and atmospheric (PIAE) effects must be added to transform the result to the final geoid heights in the real space ($N$).

## 7. Satellite, marine, and ground data combination

We combined several ground and marine databases to obtain the data set shown in Fig. 2. Specifically, onshore data from the National Geospatial Intelligence Agency (NGA) of the United States, onshore and offshore data from the Bureau Gravimetrique International (BGI), offshore data from the National Oceanographic and Atmospheric Agency (NOAA) of the United States, and a compilation of all the available historical gravity measurements for Costa Rica which were not contained in the previ-

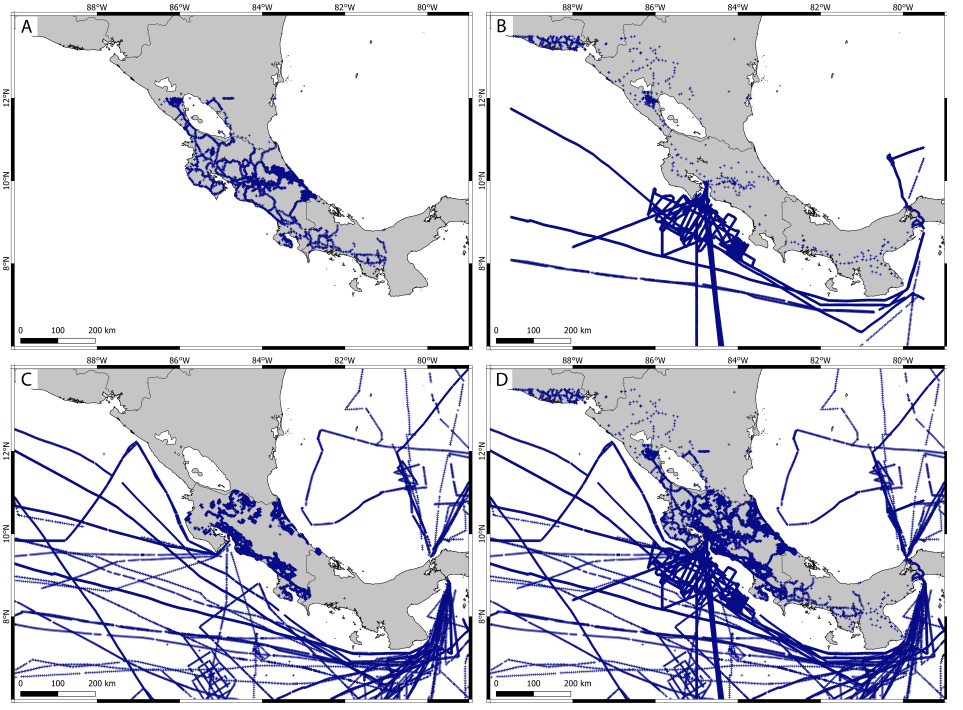


Fig. 2. Surface gravity data distribution. A: NGA database. B: BGI database, C: Costa Rica Historical Database onshore, NOAA database offshore. D: Combined quality-controlled database for calculation of GCR-RSH-2020.

ous datasets. As quality control, we used the x2sys GMT tools to check the crossover errors of the marine gravity survey, while the ground gravity databases were compared to high degree and order GGMs and topography. To carry out this comparison, gravity disturbances ($\delta g$) were computed in both land gravity values and GGMs. The ICGEM calculation service (`http://icgem.gfz-potsdam.de/calcgrid`) allows to compute the gravity disturbance quantities which uses the ETOPO1 to perform the necessary computations (*Barthelmes, 2013*). To make the computation of $\delta g$ of the land gravity values ($\delta g^{Terrest}$) closer to the ones computed by the ICGEM calculation service ($\delta g^{Model}$), we estimate h by bilinear interpolation using the ETOPO1 each model and $N$ values from the geoid models grids. The residuals from the subtraction of to the would give a value that can be use to validate both the GBG and the CGMs ($\delta g^{DIFF}$) (see Eq. (9)). Table 1 shows the CGMs used performed this comparison while Table 2 shows the statistics of this process. Furthermore, we assessed the land gravity values in the form of classical Bouguer anomalies ($\Delta g$) using leave-one-out cross validation (LOOCV). Fig. 3 shows the histogram of the residuals of this validation process after removing outliers, and their statistics.

$$\delta g^{DIFF} = \delta g^{Terrest} - \delta g^{Model}. \tag{9}$$

Table 1: global geopotential models (GGM) used for the computation of gravity disturbances.

| **Gravity Model** | **Degree / Order** | **Max. Resolution** | **Reference** |
|---|---|---|---|
| EGM2008 | 2190 | 5' approx. | *Pavlis et al., 2012* |
| Eigen-6C4 | 2190 | 5' approx. | *Förste et al., 2014* |
| GECO | 2190 | 5' approx. | *Gilardoni et al., 2016* |
| SGG-UGM-1 | 2159 | 5' approx. | *Liang et al., 2018* |

Approximately, 160000 points remained of the original 209000 after quality control. The estimated overall uncertainty of the terrestrial gravity anomalies was about 2.3 mGal, with residuals of up to 16 mGal in magnitude. They appear to be unbiased and normally distributed. Furthermore, satellite altimetry data from *Sandwell et al. (2014)* was used to augment the marine gravity, excluding land values and a buffer zone of 20 km from the coastline. Finally, overlaid a $5 \times 5$ arc-minute grid to fill gaps in the datasets. Empty cells in this grid were filled with Bouguer gravity anoma-

Table 2. Statistics on the gravity disturbance difference ($\delta g^{DIFF}$) for land gravity point.

| | **EGM08** | **EIGEN6C4** | **GECO** | **SGGUG** |
|---|---|---|---|---|
| Mean | −2.602 | −2.597 | −2.396 | −2.928 |
| Median | −3.340 | −2.145 | −1.894 | −3.047 |
| Min | −87.681 | −86.147 | −89.774 | −87.577 |
| Max | 92.669 | 96.819 | 98.182 | 95.252 |
| STD | 11.088 | 11.146 | 11.376 | 10.923 |
| Range | 180.350 | −182.966 | −187.956 | 182.829 |
| | N = 16812 | | | |

lies ($\delta g$) calculated from the from GECO GGM (*Gilardoni et al., 2016*). We chose GECO GGM for compatibility reasons in the process of satellite data combination, which is further explained in this section below. In a similar process of computation of $\delta g^{Model}$, $\Delta g$ values from GECO GCGM was performed using the ICGEM computation services, which approximates the quantity using the topographic spherical model ETOPO1.

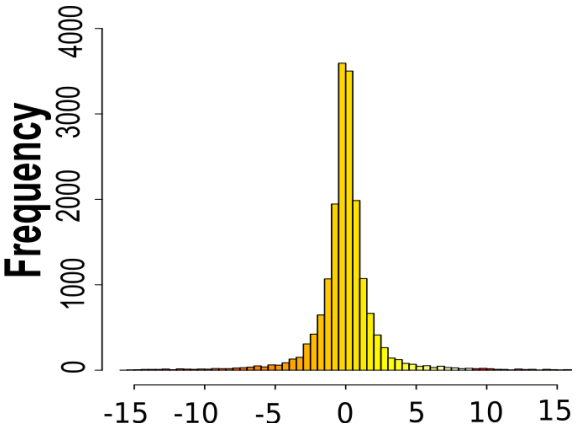


Fig. 3. The histogram shows the residuals of the LOOCV. The $x$-axis values are expressed in mGals. Statistics: Min. −15.710, 1st Qu. −0.670, Median −0.006, Mean: −0.004275, 3rd Qu. 0.677849, Max. 15.954, Std. 2.329.

To perform the interpolation, all anomalies were converted into Bouguer anomalies and aggregated to the GECO GCGM anomalies. This interpolation was performed to simplify the process instead of the more rigorous process, using NT anomalies. We assigned weights considering the date of survey, source and measurement type. All the $\delta g$ observations were gridded

with a $1 \times 1$ arc minute resolution using GMT-blockmean and GMT-surface in a way to prevent high frequency aliasing. Finally, the SRTM-1 (*U. S. Geological Survey, n.d.*) (with 1 arc-second resolution) resampled to $1' \times 1'$ was used to compute the free-air anomalies necessary to start the computation.

We chose the GOCO05s global satellite-only geopotential model (GSGM) as the reference field for our computation because of improvements made with the inclusion of GOCE data (*Mayer-Guerr, 2015*) and the compatibility with GECO GCGM previously used for filling data gaps. A degree and order of 160 was chosen as the contribution of GOCO05S. This parameter was set based on the investigations of *Foroughi et al. (2017)*. Finally, a geoid resolution of 1 arc minute was chosen for numerical stability reasons (*Foroughi et al., 2019*).

## 8. Validation and comparison to the global geoid models

To test the computations, we selected 4 GCGMs, which have the highest degree and order available. For example, EGM2008 was the first high resolution global geoid model and it is still used by many institutions as standard (*Pavlis et al., 2012*). Eigen-6C4 and GECO contain data from the Gravity Field and Steady-State Ocean Circulation Explorer (GOCE) project (*Förste et al., 2014*). Moreover, GECO contains an improvement compared to EGM2008 at medium frequencies (*Gilardoni et al., 2016*). At last, the SGG-UGM improved the resolution of the EGM2008 using GOCE and airborne gravity data in China. Since SGG-UGM is one of the newest GGM combined models, some authors suggest it needs further testing (*Liang et al., 2018*). Geoid models computed from these GCGMs have a maximum spatial resolution of approximately 9 km (5').

## 9. Results

The free-air anomalies ($\Delta g^{FA}$) are influenced by all topographic and atmospheric masses. These effects make $\Delta g^{FA}$ noisier at the topographical surface than the Helmert anomalies ($\Delta g^{H}$), which have all these masses condensed to the geoid. Fig. 4 shows a plot of both quantities over Costa Rica, Nicaragua and Panama. One can see that $\Delta g^{H}$ are recognisably

smoother than $\Delta g^{FA}$, especially in the mountainous areas. Also, mountainous areas present larger gravity anomalies than flatlands, as we might expect. Fig. 4 further shows the condensation process to prepare $\Delta g^{FA}$ for the downward continuation operation. As one can see, a correction for lateral topographical density variations was not included in the computation because a density model was not available at the time of the computation. Also, the Hörmander effect has not been included, but is very small compared to our expected final centimetric accuracy (see *Janák et al. (2017)*).

Fig. 5 shows the downward continued Helmert anomalies ($\Delta g_g^H$). When the reference anomalies ($\Delta g_{sat}^H$) are subtracted from $\Delta g_g^H$, we obtained the residual Helmert anomalies ($\Delta g_{res}^H$) on the geoid that are required to compute the residual cogeoid. One can notice that $\Delta g_g^H$ quantities are rougher than $\Delta g^H$, as expected.

Applying Stokes' integral provides the residual cogeoid, that is then added to the reference cogeoid computed from GOCO05s. This operation provides a complete cogeoid that is converted to the geoid by adding the primary indirect topographic effect (PITE) and primary indirect atmospheric effect (PIAE) to transform the resultant surface from the Helmert space to the real one. Moreover, the final geoid model is referred to the GRS80 system which has a slightly different reference geopotential value than the WGS84. Thus, the computed geoid was transformed to WGS84 using the correction to the zero degree order suggested by ICGEM Centre (see FAQ from `http://icgem.gfz-potsdam.de/icgem_faq.pdf`). Fig. 6 shows the quantities of residual cogeoid, reference cogeoid, and final geoid. As expected, the higher N values are presented in the Talamanca Range and the lower values on the coastal areas. The geoid height range is 15.733 m, where 3.032 m and 18.765 m are the lowest and highest values respectively. We called this geoid determination the 2020 Regional Stokes-Helmert Costa Rican Geoid (GCR-RSH-2020), following a Spanish abbreviation.

To validate this result, the GCR-RSH-2020 was compared to 4 GCGMs. The smallest and largest differences are approximately 0.4 m and 1.5 m respectively. In evaluating these comparisons, we must consider that the maximum spatial resolution of a GCGM is approximately 9 km while the computed geoid has a maximum spatial resolution of 1.8 km. Thus, these differences might come from the GCGMs smoothing. We believe that more rigorous comparison would not be necessary because it is noticeable that

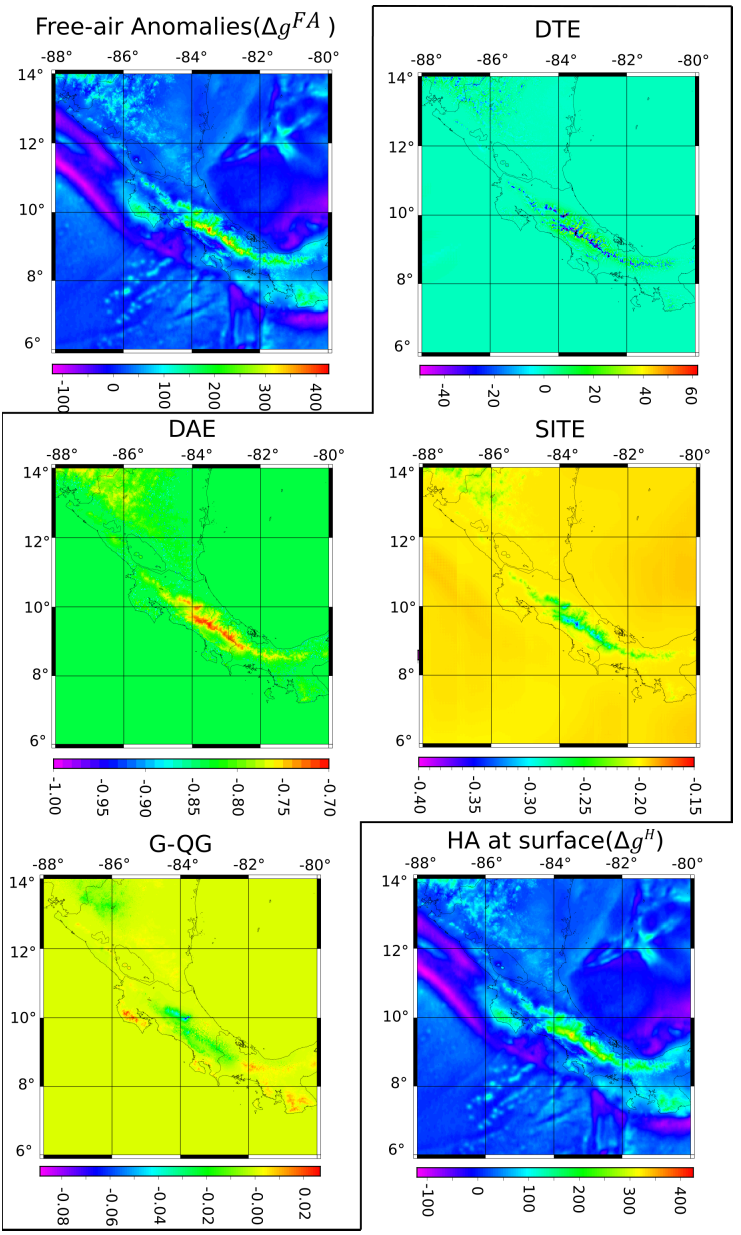


Fig. 4. The process of condensation is shown in this figure; all quantities are expressed in mGal.

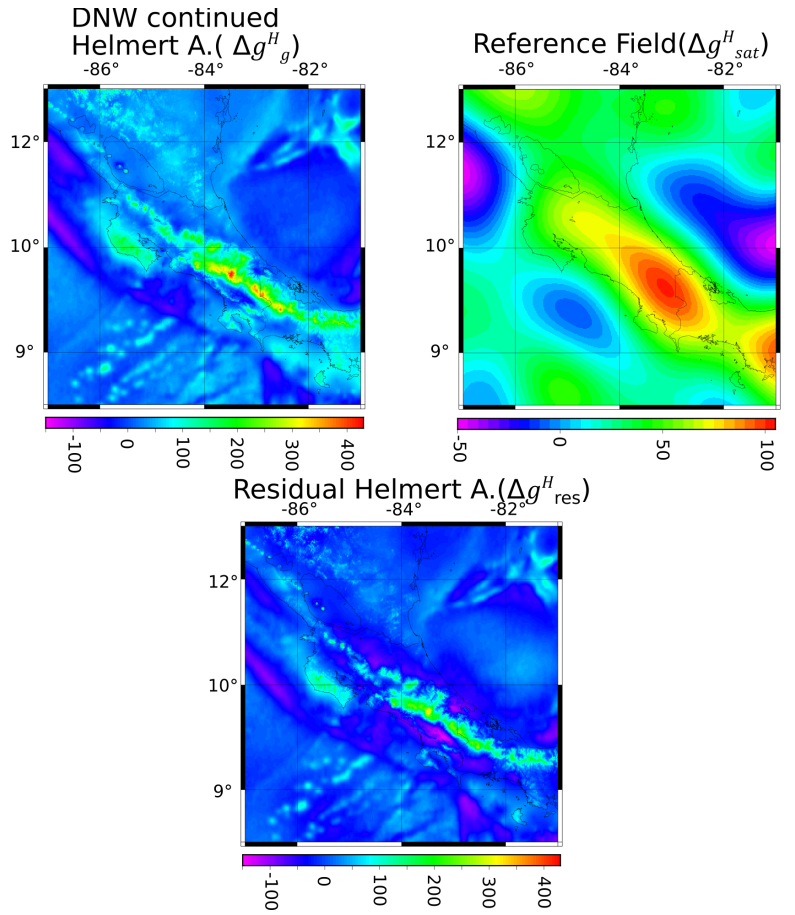


Fig. 5. The downward continued Helmert anomalies ($HA_{geoid}$) minus the references Helmert ($HA_{RF}$) give the residual Helmert Anomalies ($HA_{res}$); all quantities are expressed in mGal.

the main differences are in the mountainous areas and the Talamanca range. Also, the differences found in the rest of the country are centimetric.

Fig. 7 shows the subtraction of the chosen GCGM from GCR-RSH-2020. As seen, the largest differences are obtained when comparing to the EGM2008 geoid. This result shows that the improvements in Costa Rica from the new models are mostly in the mountains. Other testing against models EIGEN-6C4, GECO, SGG-UGM-1 show smaller residuals, but the

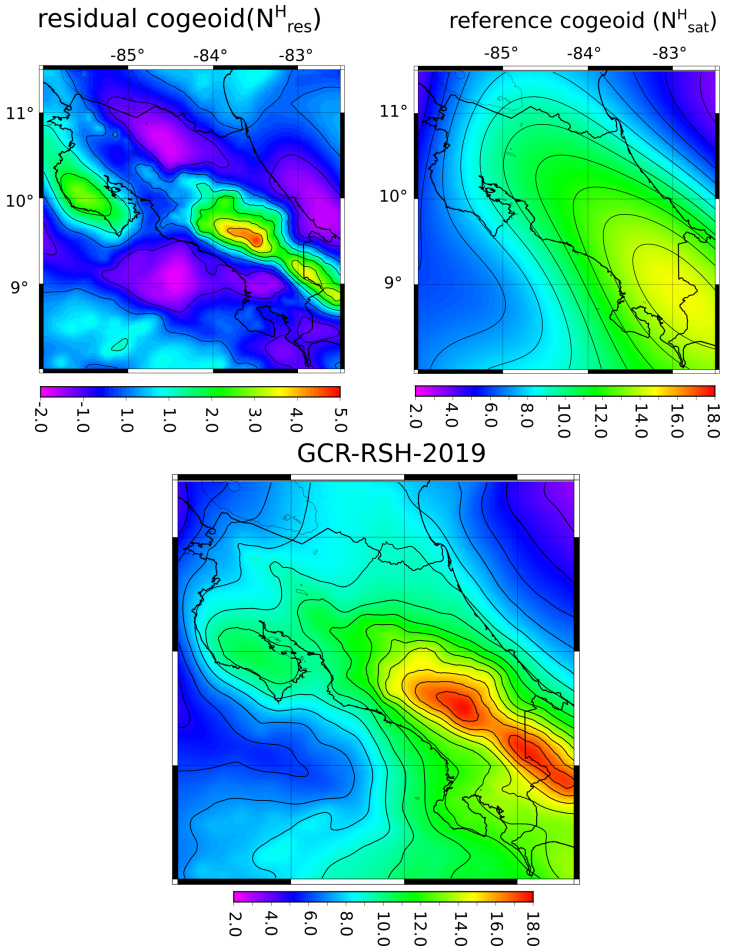


Fig. 6. Quantities of the residual cogeoid, reference cogeoid and the final geoid model. Red values represent the higher geoid heights ($N$) while blue/violet the lower ones. The geoid is referred to WGS84. The units are metres (m).

lowest differences are obtained in comparisons with SGG-UGM-1 and GECO (see Fig. 7). We are aware that there is a stronger correlation between our solution and these two GCGM, because they both include the new GOCE satellite gravity data. However, this also means that our solution is consistent with other modelling based on this data, and properly incorporates the improved model.

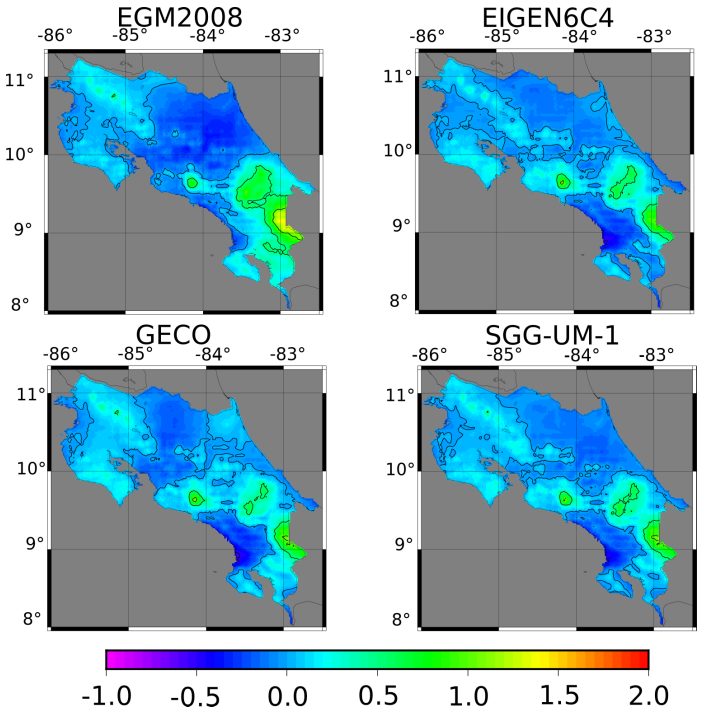


Fig. 7. The ellipsoidal height differences between GCR-RSH-2020 and each of the 4 GCGM models are presented in meters.

We computed differences from global models both including and excluding ocean areas. This process was done to know how the geoid behaves in both conditions, and to be able to isolate issues with topography and land gravity from issues with the geoid modelling as a whole. Differences from these global models should be approximately normally distributed. Fig. 8 shows a histogram of the differences when ocean values are included, i.e., when the whole onshore and offshore geoid is compared with global models. As seen, the residuals have approximately normal distribution, with longer tails extending to the right of the histogram indicating some extreme positive differences. The histograms for differences from GECO and from SGG-UM-1 are similar to one another. The statistics of these differences show a small systematic shift between the geoid and the other global geoid models (see Table 3). Also, we can conclude that the ocean determination of the $N$ values is accurate because the interquartile range is centimetric.

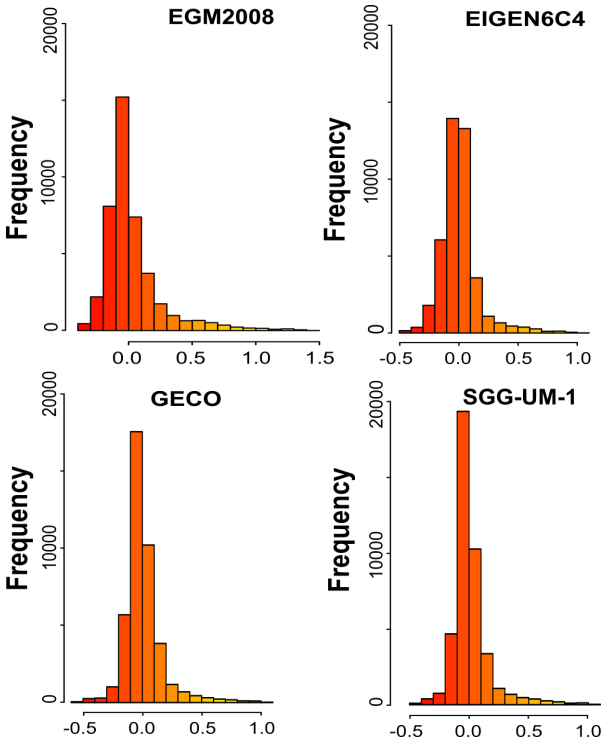


Fig. 8. The histogram of the differences between the global geoid models and GCR-RSH-2020, including ocean values. Horizontal axes are in metres.

The histograms of the differences for land values (see Fig. 9) present differences in contrast to the ones show in Fig. 8. The EGM2008 differences

Table 3. Statistics of the differences between global geoid models and GCR-RSH-2020, including ocean values. All quantities are in metres.

| | **EGM2008** | **EIGEN6C4** | **GECO** | **SGG-UM-1** |
|---|---|---|---|---|
| Min | −0.396 | −0.494 | −0.535 | −0.464 |
| Max | 1.431 | 1.065 | 1.082 | 1.088 |
| 1st Qu. | −0.101 | −0.083 | −0.079 | −0.065 |
| 3rd Qu. | 0.078 | 0.059 | 0.061 | 0.046 |
| Median | −0.029 | −0.007 | −0.023 | −0.018 |
| Mean | 0.026 | 0.006 | 0.006 | 0.012 |
| Range | 1.827 | 1.559 | 1.617 | 1.552 |
| Std | 0.231 | 0.162 | 0.167 | 0.162 |

have a more substantial tail to the right while the other global geoid models have histograms approaching the normal distribution. Moreover, the statistics show a bias of approximately 5 cm from the global fields, but this is probably influenced by the positive tails of the histogram. The median values, when comparing to EIGEN-6C4 and SGG-UM-1, is very close to 0 (see Table 3). The extreme values that influence the mean value come mostly from the Talamanca mountain range and the Cerro de la Muerte region, as seen in Fig. 7, and these have a greater influence when excluding ocean values because fewer values are averaged. The minimum and maximum values from Tables 3 and 4 slightly differ due to interpolation error in the resampling process (the resolution of the GGM is about 5'), but the differences are not significant.

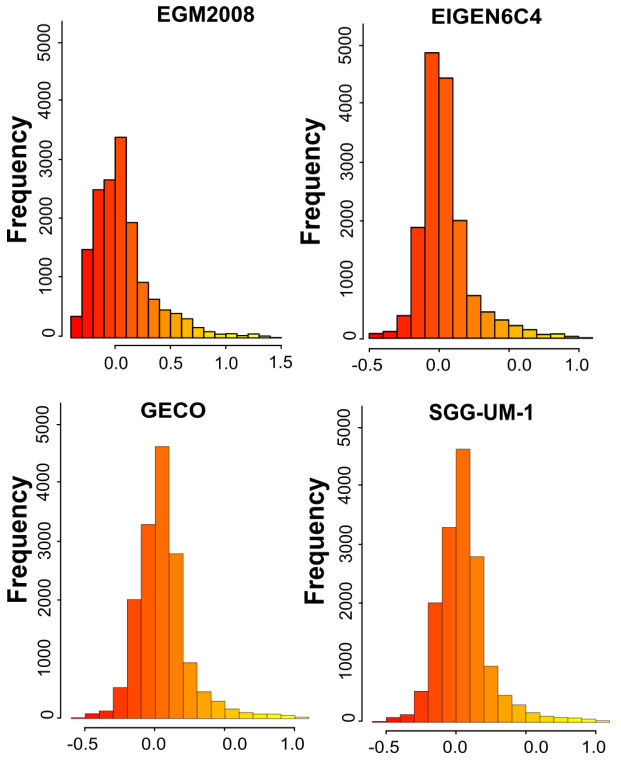


Fig. 9. The histogram of the differences between global geoid models and GCR-RSH-2020, excluding ocean values. Horizontal axes are in metres.

Table 4. Statistics of the differences between global geoid models and GCR-RSH-2020, excluding ocean values. All quantities are in metres.

| | **EGM2008** | **EIGEN6C4** | **GECO** | **SGG-UM-1** |
|---|---|---|---|---|
| Min | −0.397 | −0.493 | −0.535 | −0.463 |
| Max | 1.436 | 1.070 | 1.087 | 1.093 |
| 1st Qu. | −0.119 | −0.064 | −0.052 | −0.070 |
| 3rd Qu. | 0.159 | 0.102 | 0.126 | 0.110 |
| Median | 0.023 | 0.009 | 0.042 | 0.017 |
| Mean | 0.069 | 0.043 | 0.055 | 0.048 |
| Range | 1.833 | 1.563 | 1.622 | 1.556 |
| Std | 0.275 | 0.183 | 0.192 | 0.188 |

The accuracy of the old Costa Rican height system is still in debate and is unknown. However, GNSS/levelling differences on 25 selected benchmarks of the old height system are the only available independent method for testing the computation. Table 5 shows the comparison of GNSS/levelling geoid-ellipsoid separations from GCR-RSH-2020 model and from the different GCGM geoids. The GNSS/levelling points were distributed evenly along the country (see Fig. 10). Consequently, a shift of 7 cm can be seen from the subtraction of GCR-RSH-2020 from GNSS/levelling values. This result is not surprising because the old height system was referred to an unknown reference surface tied to a tidal gauge. GCR-RSH-2020 showed a better standard deviation of differences than the GCGMs, suggesting a higher relative accuracy. However, a 5% significant level Fisher test on the variance does not show significant differences among the models. Since all models showed a similar level of disagreement, it is likely that these variations are mainly associated with errors in the existing height system rather than in the geoid models, and this makes it difficult to draw strong conclu-

Table 5. Differences between the geoid-ellipsoid separations from GNSS/levelling and from global geoid models. All quantities are in metres. 25-point sample size.

| | **GCR-RSH-2019** | **EGM08** | **Eigen6C4** | **GECO** | **SGG-UM-1** |
|---|---|---|---|---|---|
| Mean | 0.072 | 0.013 | 0.026 | 0.006 | 0.026 |
| Min | −0.396 | −0.489 | −0.370 | −0.390 | −0.455 |
| Max | 0.643 | 0.692 | 0.680 | 0.703 | 0.672 |
| Median | 0.074 | −0.005 | −0.023 | −0.007 | −0.001 |
| Std | 0.207 | 0.263 | 0.217 | 0.228 | 0.216 |
| Range | 1.039 | 1.181 | 1.050 | 1.093 | 1.127 |

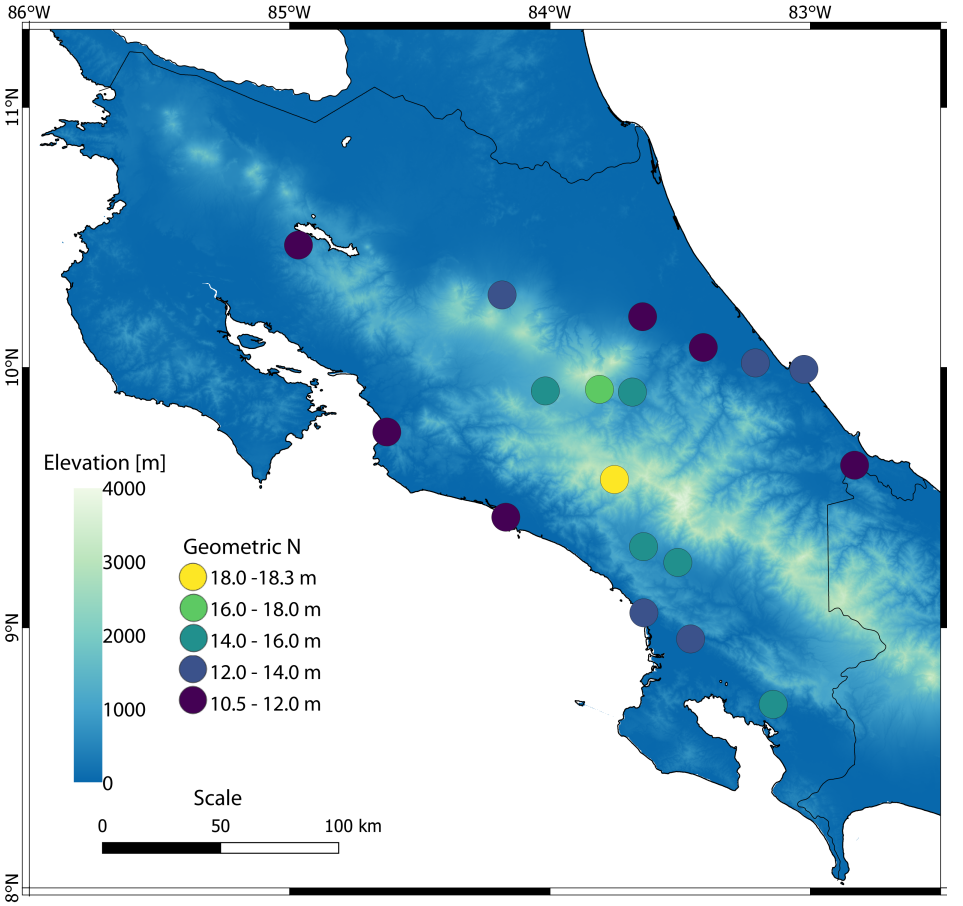


Fig. 10. GNSS/levelling geoid-ellipsoid separations. The circles show the location of the benchmarks used for validation of N and the resulting value.

sions from this comparison.

All the results shown above suggest that GCR-RSH-2020 is consistent with the global geoid models and is more accurate in terms of the determination of ($N$) as well as having a better spatial resolution (1.8 km compared to 9 km). The analysis is limited by the small number of GNSS/levelling points for comparison and the quality of those points. The small size of the comparison area excluding ocean values limits comparisons with GCGMs as local differences, e.g. in mountain areas, significantly affect the mean differ-

ence. There is still more work to carry out for the Costa Rica geoid determination. However, we consider our solution is accurate enough to be released to the public for validation purposes. Moreover, we will focus on gravity ground surveys for the Talamanca region and a density model to improve our geoid determination in the near future. Also, more GNSS/levelling data samples must be collected to evaluate the computation more thoroughly.

## 10. Concluding remarks

A geoid for Costa Rica was computed using the UNB Stokes-Helmert approach. This effort used data derived from satellite altimetry, marine gravity surveys, and terrestrial gravity surveys, which were transformed to the Helmert anomalies derived from the free-air anomalies. We downward continued the data from the physical surface of the Earth to the geoid and filled any data gaps with the GECO GCGM. An interpolation process was performed using Bouguer anomalies to reconstruct a regular grid of $1' \times 1'$ resolution, using the SRTM1 DTM. The final $\Delta g^{FA}$ values matched with the Costa Rican topography and the geological structures. Thus, we confirmed that the interpolation process was reasonable. The computed 2020 Regional Stokes-Helmert Costa Rican Geoid (GCR-RSH-2020) has maximum and minimum values of 15.733m and 3.032m using the WGS84 vertical reference geopotential value. GCR-RSH-2020 was consistent with GCGMs over a large area. Values over land only appeared biased relative to the tested GCGMs, but the small area tested limits the meaningfulness of such analysis. The GECO and the SGG-UM-1 GCGMs presented a better agreement with the geoid model based on histograms and the statistics. The maximum and minimum values of the differences are approximately 1.5 m and $-0.5$ m approximately with the largest discrepancies in the mountainous areas, where global models and gravity data are both likely to be of lower quality. Approximately, a 5 cm shift was found in the difference between of geoid values over land from the GCGM and the GCR-RSH-2019 models, largely because the GCR-RSH-2020 model was higher in mountainous areas. This disagreement in the mean is possible despite the inclusion the GOCO satellite-only global geopotential model, which improves the lower frequencies of the geoid, because the inclusion of the better distributed and high quantity land data might have an effect in this systematic shift. When com-

pared with GNSS/levelled geoid-ellipsoid separations, the smallest variance was given by GCR-RSH-2020. This result shows that the GCR-RSH-2020 is at least as accurate as the tested GCGMs, but there are no statistical differences in the variances of these models based on the Fisher test on the variance. The model GCR-RSH-2020 also represents an improvement in terms of spatial resolution. A greater number of GNSS/levelling data samples would allow to test the variances more adequately, and these tests would be more meaningful if compared against a more precise levelling datum. In the future, we are working on a density model and collecting more gravity ground data especially in the Talamanca range and Cerro de la Muerte region to improve future geoid computation as well as more GNSS observations on levelled bench marks for validation.

***Acknowledgements***. We acknowledge the contribution of the National Geospatial Intelligence Agency (NGA) of the United States, the Bureau Gravimétrique International (BGI), and CENIGA for the provided gravimetric data, which is an important part of this research. This article is a contribution to the Surveying Engineering School's project 341-B6-538 part of the research program *Red Sismológica Nacional* of the University of Costa Rica.

## References

Ballestero C. L. E., Dobrinescu M. M., Jager G. C., Mayers I. R., 1995: An Integrated Geological and Geophysical Interpretation of the San Carlos Basin, Costa Rica. In: Miller R. L., Escalante G., Reinemund J. A., Bergin M. J. (Eds.): Energy and Mineral Potential of the Central American-Caribbean Region. Berlin, Heidelberg: Springer Berlin Heidelberg, 95–103, doi: 10.1007/978-3-642-79476-6_11.

Barritt S., Berrangé J., 1987: Interpretation of a Gravity Survey of the Osa Peninsula and environs, Southern Costa Rica. Overseas Geology and Mineral Resources, No. 64, British Geological Survey.

Barthelmes F., 2013: Definition of functionals of the geopotential and their calculation from spherical harmonic models: theory and formulas used by the calculation service of the International Centre for Global Earth Models (ICGEM). http://icgem.gfz-potsdam.de/ICGEM/, revised Edition, (Scientific Technical Report, 09/02), Potsdam: Deutsches GeoForschungsZentrum GFZ, 32 p., doi: 10.2312/GFZ.b103-0902-26.

Cordero Gamboa G., 2010: Development of the CGV08 geoid model as a contribution to the determination of a national geoid (Desarrollo de un modelo geoidal CGV08 como insumo para la determinación nacional del geoide). Uniciencia, **24**, 1, 35–40 (in Spanish).

de Boer J., 1974: Mapa geofísico preliminar de Costa Rica – Escala 1:500 000. San Jose, Costa Rica: Instituto Geográfico Nacional de Costa Rica (in Spanish).

Denyer P., Vargas C., Lücke O. H., Solano J., 2019: Deformation and Geomorphology (Deformación y Geomorfología). In: Denyer P. (Ed.): Geological perspective of northwestern Costa Rica: History, Evolution and Cartography (Perspectiva Geológica del Noroeste de Costa Rica. Historia, Evolución y Cartografía), 1st ed., 26 p., San Jose, Costa Rica: Editorial Universidad de Costa Rica (in Spanish).

Ellmann A., Vaníček P., 2007: UNB application of Stokes-Helmert's approach to geoid computation. J. Geodyn., **43**, 2, 200–213, doi: 10.1016/j.jog.2006.09.019.

Foroughi I., Vaníček P., Kingdon R. W., Goli M., Sheng M., Afrasteh Y., Novák P., Santos M. C., 2019: Sub-centimetre geoid. J. Geod., **93**, 6, 849–868, doi: 10.1007/s00190-018-1208-1.

Foroughi I., Vaníček P., Novák P., Kingdon R. W., Sheng M., Santos M. C., 2017: Optimal Combination of Satellite and Terrestrial Gravity Data for Regional Geoid Determination Using Stokes-Helmert's Method, the Auvergne Test Case. In: Vergos G. S., Pail R., Barzaghi R. (Eds.): International Symposium on Gravity, Geoid and Height Systems 2016, 37–43, Springer, doi: 10.1007/1345_2017_22.

Förste C., Bruinsma S., Abrikosov O., Flechtner F., Marty J.-C., Lemoine J.-M., Dahle C., Neumayer H., Barthelmes F., König R., Biancale R., 2014: EIGEN-6C4 – The latest combined global gravity field model including GOCE data up to degree and order 1949 of GFZ Potsdam and GRGS Toulouse. In: EGU General Assembly Conference Abstracts, EGU General Assembly 2014, Vienna, **16**, 3707.

Gilardoni M., Reguzzoni M., Sampietro D., 2016: GECO: a global gravity model by locally combining GOCE data and EGM2008. Studia Geophys. et Geod., **60**, 2, 228–247, doi: 10.1007/ s11200-015-1114-4.

Gurney S., 1997: Geophysical reconnaissance of the Golfo Dulce drainage basin and environs of Costa Rica. Thesis, University of Toledo.

Heiskanen W. A., Moritz H., 1967: Physical Geodesy. W. H. Freeman and Company, San Francisco.

Hofmann-Wellenhof B., Moritz H., 2006: Physical geodesy. Springer-Verlag Vienna, Science & Business Media, 403 p., doi: 10.1007/978-3-211-33545-1.

Huang J., 2002: Computational Methods for the Discrete Downward Continuation of the Earth Gravity and Effects of Lateral Topographical Mass Density Variation on Gravity and the Geoid. Ph.D. dissertation, Department of Geodesy and Geomatics Engineering, Technical Report No. 216, University of New Brunswick, Fredericton, New Brunswick, Canada, 141 p.

Janák J., Vaníček P., Foroughi I., Kingdon R., Sheng M. B., Santos M. C., 2017: Computation of precise geoid model of Auvergne using current UNB Stokes-Helmert's approach. Contrib. Geophys. Geod., **47**, 3, 201–229, doi: 10.1515/congeo-2017-0011.

Kingdon R., Vaníček P., 2011: Poisson downward continuation solution by the Jacobi method. J. Geod. Sci., **1**, 1, 74–81, doi: 10.2478/v10156-010-0009-0.

Liang W., Xu X., Li J., Zhu G., 2018: The determination of an ultra high gravity field model SGG-UGM-1 by combining EGM2008 gravity anomaly and GOCE observa-

tion data. Acta Geod. et Cartogr. Sin., **47**, 4, 425–434, doi: 10.11947/j.AGCS.2018.20170269.

Lücke O. H., 2018: Geophysics and geodynamics of the volcanic arc in Costa Rica (Geofísica y geodinámica interna del arco volcánico en Costa Rica). San Jose, Costa Rica, https://vinv.ucr.ac.cr/sigpro/web/projects/B5A00 (in Spanish).

Mayer-Guerr T., 2015: The combined satellite gravity field model GOCO05s. In: EGU General Assembly Conference Abstracts, EGU General Assembly 2015, Vienna, **17**, 12364.

Monges J., 1958: Isoanomalías Bouguer de la gravedad – Escala 1:2 000 000. San Jose, Costa Rica: Instituto Geográfico de Costa Rica (in Spanish).

Morelli C., Gantar C., T. Honkasalo T., McConnell R. K., Tanner J. G., Szabo B., Uotila U., Whalen C. T., 1972: The International Gravity Stadardization Net 1971. Osservatorio Geofisico Sperimentale, Trieste, https://apps.dtic.mil/dtic/tr/fulltext/u2/a006203.pdf.

Moya Zamora J., Dörries E., 2004: A study of the geoid undulation (Estudio de la ondulación del Geoide). Uniciencia, **21**, 1, 151–155 (in Spanish).

Pavlis N. K., Holmes S. A., Kenyon S. C., Factor J. K., 2012: The development and evaluation of the Earth Gravitational Model 2008 (EGM2008). J. Geophys. Res.: Solid Earth, **117**, B4, doi: 10.1029/2011jb008916.

Sandwell D. T., Müller R. D., Smith W. H. F., Garcia E., Francis R., 2014: New global marine gravity model from CryoSat-2 and Jason-1 reveals buried tectonic structure. Science, **346**, 6205, 65–67, doi: 10.1126/science.1258213.

Stokes G. G., 1849: On the variation of gravity on the surface of the Earth. Trans. Cam. Phil. Soc., **8**, 672–695.

Tenzer R., Vaníček P., Novák P., 2003a: Far-zone contributions to topographical effects in the Stokes-Helmert method of the geoid determination. Studia Geophys. et Geod., **47**, 3, 467–480, doi: 10.1023/A:1024799131709.

Tenzer R., Vaníček P., van Eck van der Sluijs S., Hernández-Navarro A., 2003b: On some numerical aspects of primary indirect topographical effect computation in the Stokes-Helmert theory of geoid determination. Rev. Cartogr., **76-77**, 71–78.

Torge W., Müller J., 2012: Geodesy. 4th Edition, Walter de Gruyter, Berlin. doi: 10.1515/9783110250008.

U. S. Geological Survey (n.d.): USGS EROS Archive – Digital Elevation – Shuttle Radar Topography Mission (SRTM) 1 Arc-Second Global. Earth Resources Observation and Science (EROS) Center, doi: 10.5066/F7PR7TFT.

Vaníček P., Kingdon R., Santos M., 2012: Geoid versus quasigeoid: a case of physics versus geometry. Contrib. Geophys. Geod., **42**, 1, 101–118, doi: 10.2478/v10126-012-0004-9.

Vaníček P., Kleusberg A., 1987: The Canadian geoid-Stokesian approach. Manuscr. Geod., **12**, 2, 86–98.

Vaníček P., Sjöberg L. E., 1991: Reformulation of Stokes's Theory for Higher than Second Degree Reference Field and Modification of Integration Kernels. J. Geophys. Res.: Solid Earth, **96**, B4, 6529–6539, doi: 10.1029/90JB02782.

Varela Sánchez M., 2018: Establishment of a tool for the re-definition of the height system for Costa Rica by means of a static gravimetric geoid (Establecimiento de una herramienta para la redefinición del sistema de alturas de Costa Rica mediante la obtención de un geoide gravimétrico estático). Ph.D. Thesis, National University of Rosario, Argentina (in Spanish).

Contributions to Geophysics and Geodesy Vol. 50/2, 2020 (249–259)

# Geophysical survey of earthen dam using the electrical prospecting methods

Yermek M. AKHMETOV[1], Kambar M. ASSEMOV[1,*], Victor N. SHAYTOROV[2]

[1] National Center on complex processing of mineral raw materials of the Republic of Kazakhstan, Almaty, Kazakhstan

[2] Institute of Geophysical Research, Kaskelen, Almaty region, Kazakhstan

**Abstract:** The hydraulic structures for the land reclamation needs and their operation are the objects of careful attention. The water-bearing earth dams of small height pose an extra danger, where the accident occurs the most often. Such facilities should be constantly monitored to prevent the dangerous incidents. The article discusses an alternative method for studying the filtration properties of earth dams by the electrical parameters – resistivity, induced polarization and self-potential. The relative polarizability was used to exclude the influence of electrical resistivity to the induced polarization data. A study of advanced technology to identify the filter zones was carried out on an earthen dam in the Almaty region, Kazakhstan. The measurement data for three profiles are presented as the sections form in the parameters of resistivity and relative polarizability. Their complex interpretation with the respect of self-potential data, is given as a diagram of probable filtration paths. This is possibly due to the local increased watering in the dam loamy body. Then, the electric and self-potential parameters were evaluated to determine the filtering zones. The study results of above parameters have identified several water-saturated zones in the dam body. This technology could be used to estimate the condition of such objects and their engineering-geological monitoring.

**Key words:** earthen dam, geophysics, filtration, resistivity, polarizability, self-potential

## 1. Introduction

Many hydraulic structures in Kazakhstan were constructed in the 60–80s in the last century. The longterm operation, as well as the influence of climatic and seismic factors have gradually resulted in the moral and physical deterioration of these structures. Over the past decade, there have been more than 10 dam destructions in Kazakhstan with consequences of human

* corresponding author: Kambar M. Assemov, NC CPMRM RK, 67, Zhandossov Street, Almaty, A10M6G5, Kazakhstan, tel.: +7 727 3092560, e-mail: kassemov@kazkern.kz

doi: 10.31577/congeo.2020.50.2.4

casualties and significant of economic, social and environmental damages (*Shibutova, 2017*).

Traditional methods for the structures safety determining are based on the data of external inspection and field observation. The water-physical properties data of samples taken from specially drilled wells, are used to determine the destructive processes occurring in the dam body. However, the well drilling and other excavation work violate the integrity of dam structures and may adversely affect their strength characteristics.

The world experience shows that the geophysical methods of non-destructive testing are widely used to determine the safety of hydraulic structures. The applied geophysical methods are sufficiently described in works (*Camarero and Moreira, 2017; Dzhurik et al., 2014; Fatoba et al., 2018; Kayode et al., 2018; Kolesnikov et al., 2009; Kolesnikov et al., 2012; Nwokebuihe et al., 2017; Olasunkanmi et al., 2018; Prigara et al., 2012; Prigara et al., 2014; Zumr et al., 2018*). An analysis of these works indicates that the seismic methods, georadar sounding and various modifications of electrometric methods are widely used. The advantage of geophysical methods is a mutual supplementation of the measured parameters of geophysical fields. Interpretation of these fields will allow the identification and prediction of adverse changes in the dam structure at the early stages.

Over the past 15–20 years, the significant positive experience of using the geophysical methods for the dams physical condition inspection has been accumulated. At the same time, the studies indicate that the solution of safety monitoring problem of hydraulic structures by geophysical methods could not be completely unified for all cases. This requires technologies, adapted to the specific physical and geological conditions, in particular, for the earth dams in Kazakhstan.

The authors have made a research to extend the set of informative parameters to improve the geophysical data reliability for the identification of filtration processes in the earth dams. The results of this work are the subject of this article.

## 2. Materials and methods

The field electrical surveys were served as an informational basis for the studying of possibility to increase the geophysical data reliability for the

dams filtration processes identification. The induced polarization (IP) and self-potential (SP) methods were chosen for this research.

## 2.1. Study Object

The object of study was the earthen dam 18 metres high, 156 metres long and 4.5 metres wide coping in Almaty region. The dam is composed of the loamy soils. The dam body has the outlet and emergency spillway conduits. The geophysical survey scheme is shown in Fig. 1.

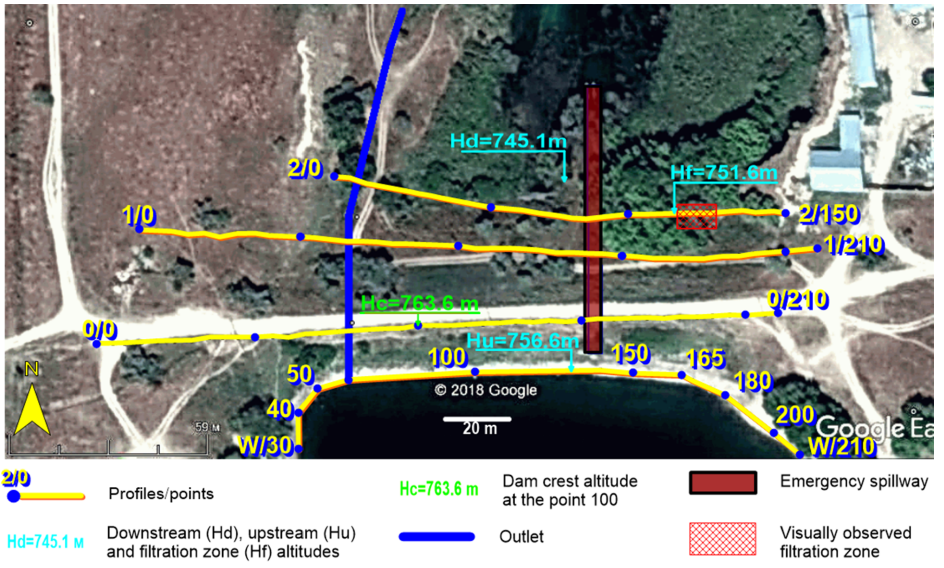


Fig. 1. The scheme of geophysical survey.

The geophysical surveys were provided with the topographic and geodetic works. They included the geophysical profiles measuring and the coordinate-altitude gridding every 5 metres in the WGS-84-UTM coordinate system.

## 2.2. Metodology

*Induced polarization method (IP)*

The purpose of survey was an assessment of electrical resistivity and polarizability inhomogeneity in the depth from 5 down to 40 metres of dam body

and identification of local changes of these parameters. The regularities of resistivity decreasing and the loamy soils polarizability increasing because of moisture increasing were a physical basis for this task solving (*Sharapanov et al., 1974*).

The survey was performed in three profiles, laid along the coping and downstream side. The dipole electrical sounding (DES-IP) was used according to the dipole-dipole scheme (Fig. 1). The polarizability distribution data were obtained by the sounding at 8 points. In this case, the distance between the centres of supply and receiving lines had been changing (Fig. 2).

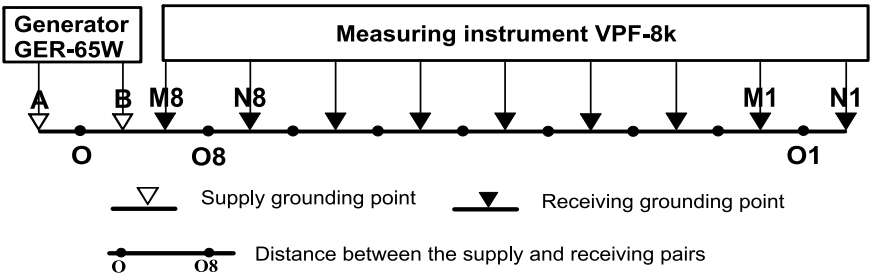


Fig. 2. The scheme of dipole electrical sounding.

The sizes of supply and receiving dipoles were 10 metres, the distance between their centers varied from 10 to 80 metres, the survey pitch – 10 metres. Such monitoring system provided the expected survey minuteness at least 40 metres depth. The used equipment: generator – GER-65W-500V, measuring instrument – VPF-8k (model of the Institute of Geophysical Research of the Republic of Kazakhstan).

It is well known that the electrical resistivity and polarizability of soils depend on the water salt content (*Komarov, 1957*). The parameter of relative polarizability ($\eta^*$) is used to take into account this factor influence in the polarizability. It was shown in (*Recommendations, 1984*) that the relation $\eta^* \approx \eta_a/\rho_a$ is valid for the granular ion-conducting rocks, where $\eta_a$ – apparent polarizability and $\rho_a$ – apparent resistivity.

The calculations of relative polarizability show that the loams and sands stably differ with the natural moisture more than 10% (*Shulga et al., 2018*). In this regard, the effective IP data are presented in the form of relative polarizability graphs.

*Self-potential method (SP)*

The electric field production during the fluid moving through the porous medium is the physical prerequisite for the estimation of filtration situation in the loamy dam body by the SP method (*Semenov, 1980*). The areas with the downward filtering are fixed by the lower potential values, and upward – by the higher values of this parameter. The intensity of observed field is higher, if the thickness of rocks is less and their resistivity is higher (*Semenov, 1980*). It is found that the potential increases to the water filtration direction. This is due to the fact that the boundary layer contains an excess of positively charged ions.

The SP measurements were carried out along the W profile line 210 metres long on headrace. The potential measurements relative to the main point in the middle of profile were carried out using the copper-sulfate non-polarizable electrodes according to the requirements (*Engineering surveys for construction, 1987*). A measuring device was the VPF-210 electric prospecting receiver (model of the Institute of Geophysical Research of the Republic of Kazakhstan).

The SP data processing includes the construction of potential increment graph along the profile and its interpretation. The results of repeated measurements show the error within $\pm 5\%$, which corresponds to the requirements (*Engineering surveys for construction, 1987*). The patterns of SP changes associated with the filtering processes were also analysed.

## 3. Results and discussions

The data processing included the drawing of sections $\rho_a$ and $\eta^*$ for all measurement points. These sections provide the spatial change of polarizability and resistivity as well as the presence of local changes of these parameters.

The interpretation results of DES-IP and SP measurements are shown in Figs. 3 and 4.

*Vertical section of resistivity*

Fig. 3 shows that the dam vertical section is characterized by the low $\rho_a$ not more than 30 $\Omega$ m in all three sections. The specified parameter increases with the depth rise.

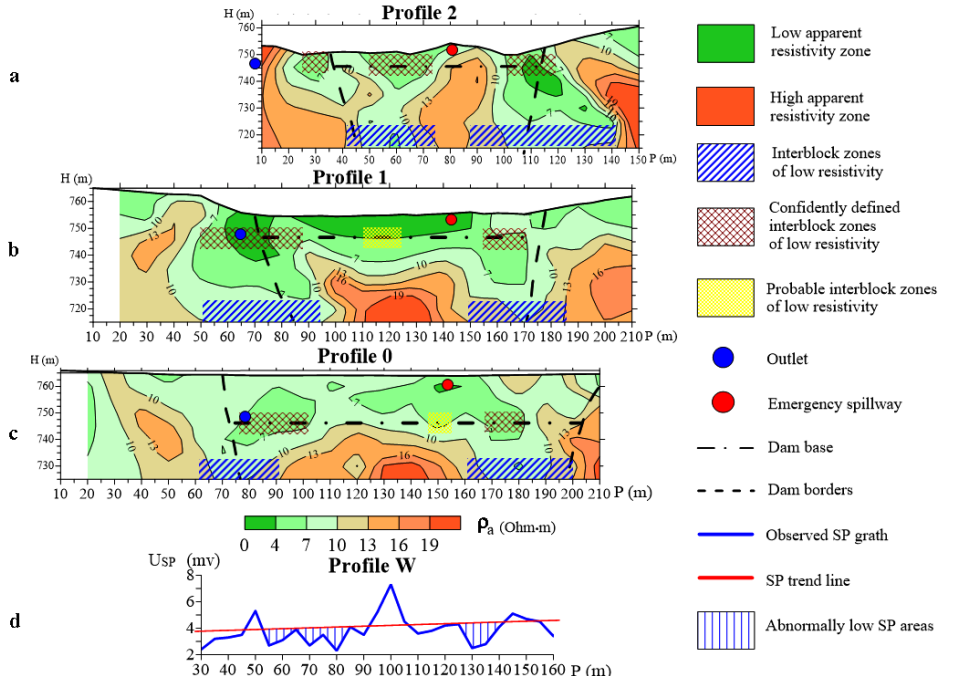


Fig. 3. The map of resistivity contours (a), (b), (c), self-potential graph (d).

A characteristic feature of $\rho_a$ sections is the significant lateral irregularity. The electrically conductive areas of various sizes and contrasts are observed. They determine the block structure of dam body sections.

There are the electrically conductive areas at the dam sides along three profiles (profile 0 points 60–95 and 160–195, profile 1 points 47–90 and 150–175, profile 2 points 35–62 and 100–133). These areas are shown over the entire range of sounding depths from 5 to 40 metres down, including below the dam base and in the visually observed water filtration zone around the points 110–125 along profile 2.

There are the metal structures in the dam body – the reservoir outlet and emergency spillway, which affect the resistivity distribution. This effect shows itself in the form of local increased electrical conductivity anomalies and the ambiguous interpretation of vertical sections around conduits. The increased electrical conductivity areas extend much lower than the conduit location (profiles 0 and 1), or do not correlate with these objects position

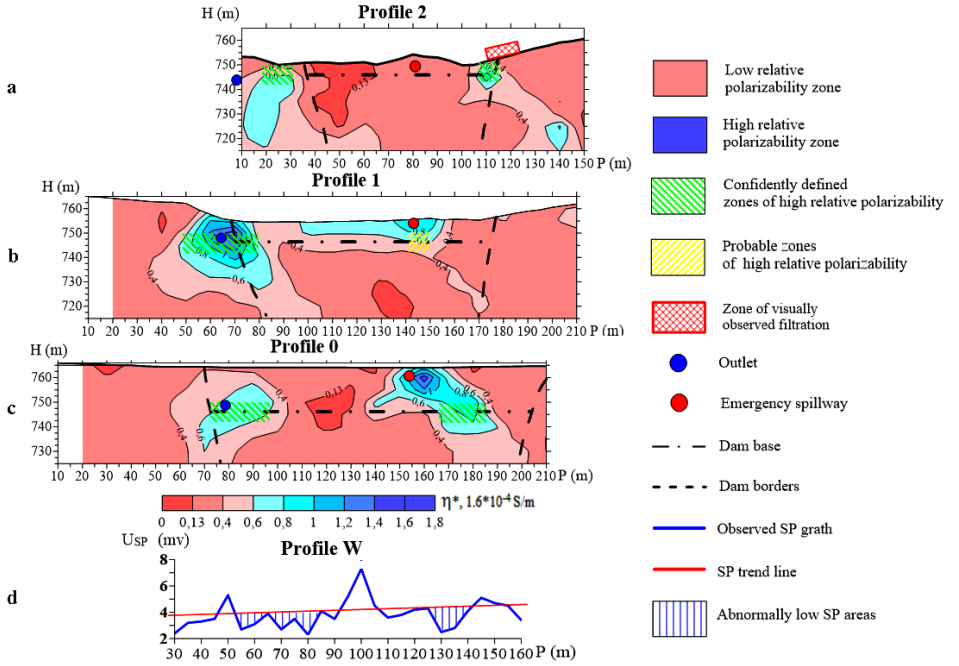


Fig. 4. The map of relative polarizability contours (a), (b), (c), self-potential graph (d).

(profile 2). It is very likely that the observed electrical conductivity effects could be interpreted as the consequence of changing of geological engineering conditions, the local increasing of moisture content in the dam loamy body.

Such local increased moisture is quite possible due to the jet water filtering. The SP data along the W profile indirectly confirm this supposition. Two zones with lower SP were found near points 55–85 and 125–143 along this profile. It is typical for the downward water filtering (*Shulga et al., 2018*). According to the DES data they are located almost in the range of increased electrical conductivity areas.

*Vertical section of relative polarizability*

The distribution of relative polarizability and its interpretation are presented in Fig. 4. The main pattern of this parameter distribution is its background or lower values in the central parts of sections. The most contrasting increased polarizability areas are on the flanks.

The maximized polarizability areas also have the shallow depth along profile 1, where the outlet and spillway are close to the surface. Such spatial relationship between the polarizability anomalies and pipelines in the increased soil moisture zones gives the good reason to suppose that these anomalies have the redox nature.

The distribution of resistivity and relative polarizability parameters is shown in Fig. 5.

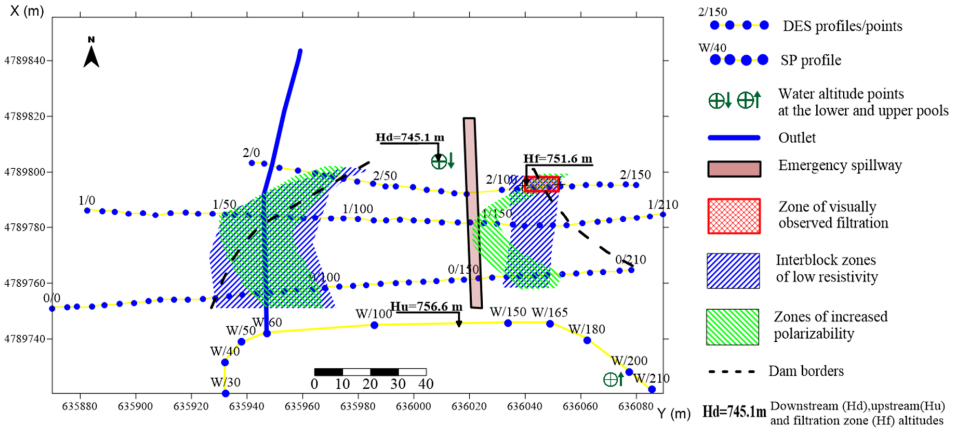


Fig. 5. The scheme of possible filtering zones according to the DES-IP data.

The abnormally increased polarizability areas are mainly consistent to the increased electroconductivity zones, except the sections of profile 1 points 140–155 and profile 2 points 20–30. The anomalous polarizability zones for these intervals are more common at the western periphery of electro-conductive zones. The detailed surveys of these areas are needed to establish the reasons for this discrepancy.

In total, the results of DES-IP are evidenced about the high efficiency of this method for the heterogeneity studying of dam body and identifying the increased water permeability areas. These areas can be the ways of concentrated water filtration from the reservoir under “the favourable conditions”.

## 4. Conclusion

As a result of geophysical studies, the following conclusions are made:

– The DES-IP data quite well distinguish the heterogeneous structure of dam body. This heterogeneity of electric parameters possibly is associated with the presence of increased water-cut zones. Based on these data, it becomes possible to chart the potential filtering paths.
– The studies have shown the relevance to clarify the electric anomalies nature in the areas of possible water pipelines influence. The solution to this task requires to use the methods, aimed to obtain the information about the loamy soils elastic-deformation properties. It is these properties primarily change with the increasing of local water permeability.

It is necessary to conduct the regime self-potential observations at the different reservoir fullness for more reasonable identification of filtration zones. This will eliminate the influence of redox and adsorption-diffusion potentials from the metal structures and clay – sand sediments.

***Acknowledgements***. The research was funded within the project No. AP0513 4944 "The development of methods for monitoring of hydraulic facilities stability based on the complex engineering and geophysical studies", granted by the Ministry of Education and Science of the Republic of Kazakhstan. The authors declare no conflict of interest.

## References

Camarero P. L., Moreira C. A., 2017: Geophysical investigation of earth dam using the electrical tomography resistivity technique. REM, Int. Eng. J., **70**, 1, 47–52, doi: 10.1590/0370-44672016700099.

Dzhurik V. I., Eskin A.Yu., Serebrennikov S. P., Bryzhak E. V., 2014: Physical condition dynamics on the weakened zones of the bulk dam of the Irkutsk Hydroelectric Power Station for the period 2002–2012. The Bulletin of Irkutsk State University – Series: Earth Sciences (Izvestiya Irkutskogo Gosudarstvennogo Universiteta – Seriya: Nauki o Zemle), **8**, 35–41, available at: http://izvestiageo.isu.ru/ru/article/file?id=217 (in Russian with English summary).

Engineering surveys for construction, 1987: Technical requirements for the production of geophysical works. Electrical intelligence. Gosstroy of the RSFSR (Republican building norms 64–87), available at: http://www.snip-info.ru/Rsn_64-87.htm (in Russian).

Fatoba J. O., Eluwole A. B., Ademilua O. L., Sanuade O. A., 2018: Evaluation of subsurface conditions by geophysical methods at Ureje Earth Dam Embankment, Ado-Ekiti, Southwestern Nigeria – A case study. Indian J. Geosci., **72**, 4, 275–282, available at: https://bit.ly/3hlBbdX.

Kayode O. T., Odukoya A. M., Adagunodo T. A., Adeniji A. A., 2018: Monitoring of seepages around dams using geophysical methods: a brief review. IOP Conf. Ser.:

Earth Environ. Sci., **173,** 2nd International Conference on Science and Sustainable Development, 493–499, doi: 10.1088/1755-1315/173/1/012026.

Kolesnikov V. P., Konoplev A. V., Prigara A. M., Tatarkin A. V., 2012: Technology of complex engineering-geophysical surveys for diagnosing the state of hydraulic structures. Sovremennye problemy nauki i obrazovaniya, 6, available at: https://www.science-education.ru/ru/article/view?id=7839 (in Russian with English summary).

Kolesnikov V. P., Tatarkin A. V., Prigara A. M., Konoplev A. V., 2009: Status diagnosis of earth dams by non-destructive testing methods. Geology and Minerals of the Western Urals: Materials of regional scientific and practical conference, Perm University, Perm, 257–262.

Komarov V. A., 1957: On the nature of electric fields caused by polarization and the possibilities of their use in the search for ore deposits. Vestnik gosudarstvennogo universiteta: Seriya Geologiya and Geographiya, **16**, 37–46.

Nwokebuihe S. C., Alotaibi A. M., Elkrry A., Torgashov E. V., Anderson N. L., 2017: Dam Seepage Investigation of an Earthfill Dam in Warren County, Missouri Using Geophysical Methods. AIMS Geosciences, **3**, 1, 1–13, doi: 10.3934/geosci.2017.1.1.

Olasunkanmi N. K., Aina A., Olatunji S., Bawalla M., 2018: Seepage Investigation on an Existing Dam using Integrated Geophysical Methods, J. Environ. Earth Sci., **8**, 5, 6–16, available at: https://iiste.org/Journals/index.php/JEES/article/download/42360/43627.

Prigara A. M., Tatarkin A. V., Pensky A. V., Osovetsky B. M., Konoplev A. V., 2012: Determination of physical and mechanical properties of soils when assessing the condition of hydraulic structures using non-destructive testing methods. Nauchnyi zhurnal KubGAU, **84**, 10, available at: http://ej.kubagro.ru/2012/10/pdf/13.pdf (in Russian).

Prigara A. M., Tsarev R. I., Konoplev A. V., Pensky O. G., Osovetsky B. M., 2014: Engineering and geological assessment of hydraulic structures with non-destructive testing methods. Fundamentalnye issledovaniya, **11**, 2, 348–352, available at: https://www.fundamental-research.ru/pdf/2014/11-2/35525.pdf (in Russian with English summary).

Recommendations on the methodology for predicting changes in the construction properties of structurally unstable soils during flooding. Industrial and Research Institute for Engineering Surveys in Construction, Stroiizdat, Moscow, 1984, 156 p. (in Russian).

Semenov A. S., 1980: Electrical exploration using the natural electric field method. Publisher Nedra, Leningrad, 446 p., available at: http://geo.web.ru/db/msg.html?mid=1183685 (in Russian).

Sharapanov N. N., Chernyak G. Ya., Baron V. A., 1974: The methodology of geophysical research in hydrogeological surveys with the aim of land reclamation. Publisher Nedra, Moscow, 176 p., (in Russian).

Shibutova L., 2017: The issue of flood prevention in Kazakhstan: statistics of destructions. Information Agency Regnum, available at: https://regnum.ru/news/economy/2279631.html/ (in Russian).

Shulga M. V., Zholdybayev A. K., Kusherbayev N. N., 2018: Electrical survey during the assessment of the dynamics of subsoil inundation in nuclear energy facilities locations (at the example of VVR-K INP). Vestnik Nacionalnogo Yadernogo Centra, **3**, 75, 67–72, available at: https://www.nnc.kz/media/bulletin/files/NOp9IwYoNM.pdf.

Zumr D., David V., Krása J., Nedvěd J., 2018: Geophysical Evaluation of the Inner Structure of a Historical Earth-Filled Dam. Proceedings (MDPI), **2**, 11, 664, 1–7, doi: 10.3390/proceedings2110664.

Contributions to Geophysics and Geodesy Vol. 50/2, 2020 (261–285)

# The comparison of the divergent and convergent tectonic plates margins seismicity – the case study: Red Sea and Zagros

Ali AMJADI[1], Bahram AKASHE[1,*], Mohammad ARIAMANESH[2], Mohsen POURKERMANI[3]

[1] Department of Geophysics, North Tehran Branch, Islamic Azad University, Tehran, Iran

[2] Department of Geology, Payam Noor University, Tehran, Iran

[3] Department of Geology, North Tehran Branch, Islamic Azad University, Tehran, Iran

**Abstract:** Regarding the seismicity of the Zagros and the Red Sea regions, the present study has investigated and analyzed the seismicity with $M \geq 5$ of these regions with obtaining seismicity coefficients, geometrical characteristics including depth, earthquake dispersion and focal mechanism of earthquakes, and their relation to each other. The estimated b-value for these two zones is approximately the same, being equal to ∼1.2. However, the total number of earthquakes in the Zagros is much higher (approximately 5.5 times), when the ratio of small to large earthquakes is about the same amount. In this study, focal depth of more earthquakes occurred and located in the Zagros and Red Sea respectively in depth of 15–20 km and 10–15 km from the earth surface, indicating that the Zagros Crust is thicker than the Red Sea.

**Key words:** Zagros, Red Sea, focal depth, magnitude-frequency relation, focal mechanism

## 1. Introduction

The Iranian plateau is a large part of the Alpine-Himalayan orogenic belt between the two Arabian Precambrian and the Hercynian Eurasian persistent zones with a convergence rate of 25 to 30 mm per year in the north-south direction (*DeMets et al., 1994*). The convergence of the Arabian plateau and the Central Iranian microcontinent is accompanied by numerous folds and fault systems called the Zagros fold-thrust belt. The present-day convergence between Arabia and Eurasia is 2–3 cm/yr (*Vernant et al., 2004*) in the N–S direction and is assumed to be unchanged since at least 10 Ma

* corresponding author: e-mail: akashebahram@gmail.com

doi: 10.31577/congeo.2020.50.2.5

(*McQuarrie et al., 2003*). The Zagros Mountain belt, which trends NW–SE, extends over 1800 km from southeastern Turkey and north of Iraq border in the NW and W of Iran to the Makran area in the SE, where oceanic subduction is still active (*Smith et al., 2012*). This belt is the result of the collision between the Arabian shield and the Iranian Block in the late Miocene (*Stöcklin, 1974*) and is currently close to half the rate of convergence between the two plates (*Tatar et al., 2002; Vernant et al., 2004; Engdahl et al., 2006*). Also, it includes more than 50% of the recorded earthquakes in the Iranian territory (*Mirzaei et al., 1998*). The thickness of the sedimentary cover and the basement depth in the area are estimated to be between 10 and 12 km (*Berberian, 1995*) and 45 km, respectively (*Hatzfeld et al., 2003; Paul et al., 2010*). Most of the earthquakes located in the simply folded belt of Zagros have thrust mechanisms and depths of less than ∼20 km. Furthermore, their ruptures have rarely reached the surface, which may be due to the presence of salt layers in the sedimentary cover (*Jackson and Fitch, 1981; Talebian and Jackson, 2004*).

The Red Sea, known as Bahr al Ahmar in Arabic, is a semi-enclosed, elongated warm body of water about 2,000 km long with a maximum width of 355 km, a surface area of roughly 458,620 $km^2$, and a volume of 250,000 $km^3$ (*Head, 1987*). The Red Sea is one of the youngest oceanic zones of the Earth and was created by slow seafloor spreading. The southeastern and southwestern border of the Arabian plateau with Africa is the diverging oceanic boundary, covered by the Gulf of Aden and the Red Sea, respectively. The plate is bounded by the Bitlis Suture and the Zagros fold belt and subduction zone to the north and north-east, and the Gulf of Aden spreading centre and Owen Fracture Zone to the south and southeast (modified after *Stern and Johnson, 2010*). The Red Sea was formed by extensional rupturing of the Precambrian lithosphere beginning in the Late Oligocene. The sea floor spreading began about 5 Ma in the southern Red Sea (*Roeser, 1975*), and the transition from continental to oceanic rifting is occurring currently in the Central and Northern Red Sea (*Cochran and Martinez, 1988; Guennoc et al., 1990; Cochran et al., 1991*). This recent seismic activity indicates that some Cenozoic faults in the Red Sea coastal plain are seismically active. Together with the Gulf of Aqaba-Dead Sea transform fault, it forms the western boundary of the Arabian plate, which is moving in a north-east direction. The Dead Sea fault system is located along the northwestern

boundary of the plate. The fault is left lateral with a minor component of rotation that results in the development of pull-apart basins, such as the Dead Sea rift basin (*Garfunkel, 1981*).

## 2. Geologic and tectonic setting of the Zagros

The Zagros mountain belt results from the closure of the Neotethys oceanic domain and the collision of the northern margin of the Arabian platform with the microplates of central Iran, accreted to the southern margin of Eurasia during the Mesozoic (e.g. *Besse et al., 1998*). The Zagros orogenic belt is bounded to the northwest by the East Anatolian left-lateral strike-slip fault (EAF) and to the southeast by the Oman Line (OL) (*Falcon, 1969*), which is here considered to be a transform fault inherited from the opening of Neo-Tethys (*Alavi, 2004*).

The fold and thrust belt on the Arabian Plate is a result of deformation of the Zagros Orogenic Belt (ZOB) passive margin sediments that have been caused by continental collision (*Alavi, 1994; Ghasemi and Talbot, 2006; Horton et al., 2008; Allahyari et al., 2010; Saccani et al., 2013*).

The Zagros were traditionally classified by distinctive lithological units and structural styles into four NW trending tectonometamorphic and magmatic belts (Fig. 1). The Zagros Fold-and-Thrust Belt (ZFTB) continental collision zone is one of the youngest and most seismically active zones on Earth (*Palano et al., 2018*). The Zagros Folded Thrust Belt (ZFTB) is divided into: The High Zagros Thrust Belt (Zagros Imbricate Zone); the Zagros Simply Folded Belt; the Zagros Foredeep; the Zagros Coastal Plain; and the Mesopotamian-Persian Gulf foreland basin (*James and Wynd, 1965; Khadivi, 2010*). The ZFTB is affected by frequent earthquakes of magnitude generally smaller than 7 concentrated at a depth of 8–15 km in the upper crystalline crust beneath the sedimentary sequence (*Paul et al., 2006; Talebian and Jackson 2004; Tatar et al., 2004*). The presence of negative isostatic anomaly near the Zagros main thrust (*Snyder and Barazangi, 1986*) and seismic evidence with focal depths greater than 50 kms in the ISC and USGS prove subduction of the Arabian plate beneath central Iran (*Nowroozi, 1971*).

*Berberian (1995)* described tectonic developments of this region as a platform phase in the Paleozoic, rifting in the Permian and Triassic, forming in-

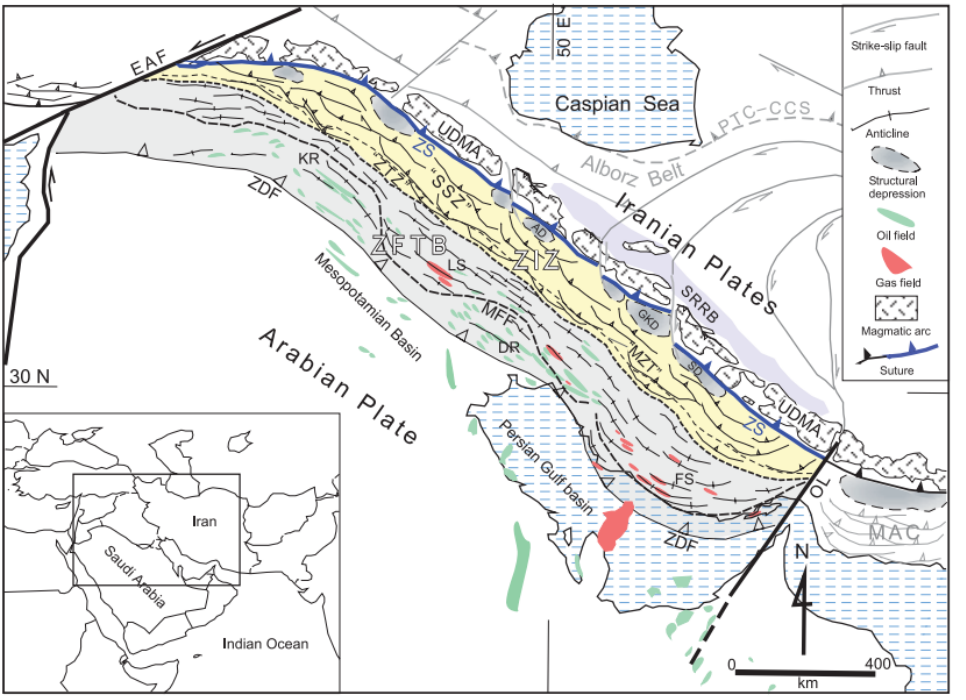


Fig. 1. Subdivisions of the Zagros orogenic belt. Abbreviations: AD – Arak depression; DR – Dezful recess; EAF – East Anatolian Fault; FS – Fars salient; GKD – Gav Khooni depression; KR – Karkuk recess; LS – Lorestan salient; MAC – Makran accretionary complex; MFF – "Mountain front flexure"; "MZT" – "Main Zagros Thrust"; OL – Oman Line; PTC-CCS – Paleo-Tethyan continent-continent collisional suture; SD – Sirjan depression; SRRB – Saveh-Rafsanjan retroforeland basin; "SSZ" – Sanandaj-Sirjan zone; "ZTZ" – Zagros thrust zone; UDMA – Urumieh – Dokhtar magmatic assemblage; ZDF – Zagros deformational front; ZFTB – Zagros fold-thrust belt; ZIZ – Zagros imbricate zone; ZS – Zagros suture. Hydrocarbon fields of the region, oil in green and gas in red, are shown (*Alavi, 2007*).

active continental margins (with seafloor spreading to the north-east) in the Jurassic and Early Cretaceous, subduction to the northeast and ophiolite and radiolite deposition in the late Cretaceous, and finally the continental-continental collision and shortening during the Neogene.

Today, their effects appear on or near the surface of the Earth as thrust faults. It can be said that the Zagros basement is about 25 to 50 km thickness (*Giese et al., 1984*).

Based on *Dehghani and Makris (1984)*, under the main Zagros fault (high Zagros), gravity anomalies reach to a minimum (−230 mgal), and in this area, the Iranian crust thickness 50 to 55 kilometers has the highest thickness, which is attributed to the compressive process associated with the opening of the Red Sea.

## 3. Geologic and tectonic setting of the Red Sea

The Red Sea, an enclosed body of water that lies between 30° N and 12° 30′ N, is about 1,932 km long and 280 km in width (*Morcos, 1970*). The narrow southern Strait of Bab-al-Mandab (29 km in width) is the boundary between the Red Sea and the Gulf of Aden. The Red Sea is one of the youngest oceanic zones on earth and was created by slow seafloor spreading. Together with the Gulf of Aqaba-Dead Sea transform fault, it forms the western boundary of the Arabian plate, which is moving in a north-easterly direction. The plate is bounded by the Bitlis Suture and the Zagros fold belt and subduction zone to the north and north-east, and the Gulf of Aden spreading centre and Owen Fracture Zone to the south and southeast (*Rasul and Stewart, 2015*) (Fig. 2 modified after *Stern and Johnson, 2010*).

According to *Swartz and Arden (1960)*, with the onset of Pliocene, marine sediments were deposited in the Red Sea due to the influx of water from the Indian Ocean into the Red Sea, meanwhile due to the uplift of the Suez Canal, the connection between the Mediterranean Sea and the Red Sea has been severed. The Red Sea Rift System is one of the world's largest active rift systems, which comprises a variety of rifting stages starting from initial faulting and advancing through several stages of continental rifting. It began about 30 million years ago, separating the western edge of the Arabian Plate from Africa (*Camp and Roobol, 1992*).

*Sultan et al. (1993)* have indicated that the Arabian and Nubian sections of the shield have remained as rigid plates during the Red Sea rifting, and the site of the present Red Sea has probably a zone of structural weakness in the late Precambrian, with the breakup and rifting controlled by pre-existing fault systems (*Makris and Rihm, 1991; Bosworth et al., 2005*). A bathymetric and topographic map prepared from various sources is presented in Fig. 3. The sea is connected to the Arabian Sea and Indian Ocean via the Gulf of Aden in the south through the narrow Strait of Bab-al-

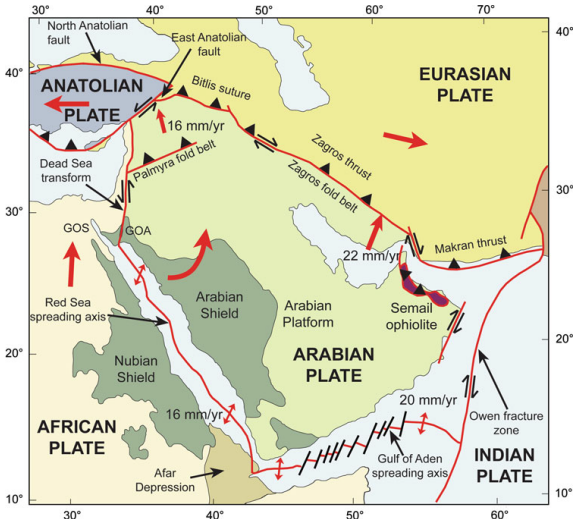


Fig. 2. Main tectonic features of the Arabian Peninsula and surrounding areas (modified after *Stern and Johnson, 2010*).

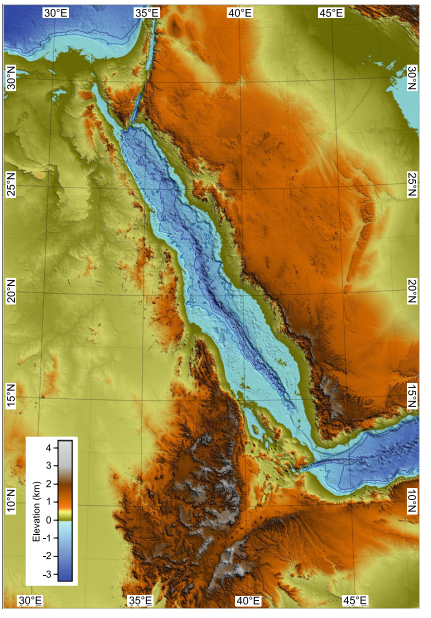


Fig. 3. Topography and bathymetric map. Bathymetric contours are at 500 m interval (Courtesy Marco Ligi).

Mandab, which has a minimum with of only 30 km, where the main channel is about 310 m deep and 25 km wide at Perim Island (*Morcos, 1970*).

Subduction Zone, and the Zagros Fold-Thrust Belt up to the East Anatolian Fault in the northwest. To the southeast, the Owen and Murray Fracture Zones separate the Arabian Plate from the Indian Plate (*El-Hussain et al., 2018*) (Fig. 4). The Red Sea has been opening since the Arabian plate broke away from the African plate about 24 million years ago (*Bosworth et al., 2005*). The rifting began with continental stretching and thinning and later progressed to sea-floor spreading. The rate of opening increases from about 7 mm/year in the northern Red Sea to roughly 16 mm/year in the south (*ArRajehi et al., 2010; Reilinger et al., 2015*). The present velocity of

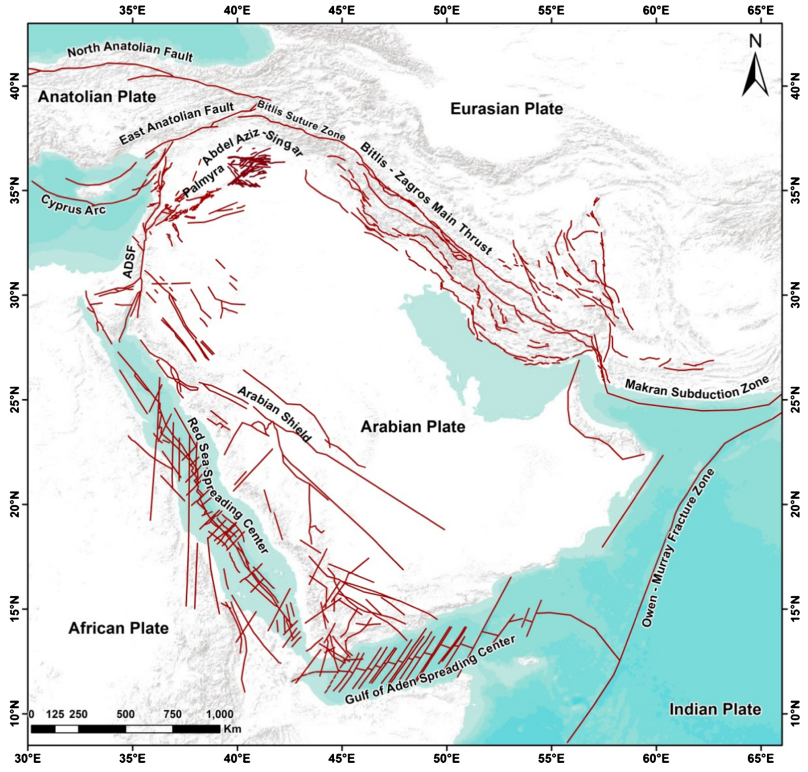


Fig. 4. Tectonic elements of the Arabian Plate (*Deif et al., 2017*). ADSF = Aqaba-Dead Sea Fault, compiled from *Johnson (1998), Brew (2001), Brew et al. (2001), Gullen et al. (2002), Hessami et al. (2003), Bosworth et al. (2005),* and *Gomez et al. (2007).* Brown lines indicate the faults.

Arabia with respect to Eurasia increases from west to east along the Persian Gulf from 18 to 25 mm/year, oriented about N 10° E (*Madahizadeh et al., 2016; Sella et al., 2002: Walpersdorf et al., 2006*).

## 4. Seismicity and Seismotectonic of Zagros

The convergence between the Arabian plate in the southwest and Eurasia in the northeast led to the complete closure of the Neo-Tethys Ocean and the formation of the Zagros continental collision zone (*Jackson and McKenzie, 1984*).

The Zagros is the most seismically active region in Iranian plateau. More than 50% of Iranian earthquakes, recorded by global seismic networks, have occurred in the Zagros Range (*Mirzaei, 1997*). Most of the earthquakes located in the Zagros Simply Folded Belt have the reverse mechanism and occur at depths of less than 20 km. Their rupture has also rarely reached the surface, which can be due to the presence of salt layers in the sedimentary cover (*Jackson and Fitch, 1981; Talebian and Jackson, 2004*). Earthquake focal mechanism solutions demonstrate shortening and thickening through major thrust faults, responsible for deformation in the Zagros (e.g., *Mostafazadeh et al., 2000: Talebian and Jackson 2004*). Although the seismicity is intensive in the Zagros, the contribution of seismic moments released by the earthquakes to the overall convergence is relatively low (*Jackson and McKenzie, 1988; Vernant et al., 2004*). A great number of earthquakes in highly seismic region of Zagros, occur on hidden faults. There is considerable uncertainty about their extent, geometry and the mechanism. most of Zagros seismicity is associated with the strike-slip faults rather than the thrust faults (e.g. *Tatar et al., 2004*). *Talebian and Jackson (2004)* and *Yamini-Fard et al. (2006)* are a few examples for doing investigations on Zagros seismotectonic province implicating the recent seismic activity within this area (*Nemati, 2015*).

## 5. Seismicity and seismotectonics of the Red Sea

Previous seismological studies in the Red Sea region have indicated the presence of a rather moderate-low shallow seismicity. The concentration of

seismicity and active volcanism along the axial trough has long been mentioned to show the present-day continuous rifting (*Drake and Girdler, 1964; Fairhead and Girdler, 1970, 1972*).

*El-Isa and Al-Shanti (1989)* concluded that the central distribution of historical and instrumental data and their characteristics illustrate a general correlation with regional geology and tectonics. Their studies have shown that ∼60% of all energy released from instrumental earthquakes has been released from concentrated earthquakes in the spreading zone. These three sequences occurred at the intersection of three major structural trends, the Gulf of Aqaba–Dead Sea Rift, the Gulf of Suez, and the main Red Sea rift. The Red Sea is divided into three distinct zones; each zone represents different stages of development (*Cochran and Martinez, 1988*). The most recent earthquake sequences occurred in 1969, 1972, and 2001. The 1969 Shadwan sequence, characterized by a maximum magnitude mb 6.0 and Ms 6.8, occurred in the north near Shadwan. The largest event of moment magnitude (Mw) 7.1 took place on 22 November 1995 at the Gulf of Aqaba, causing structural damage to buildings in several cities along the gulf coast (*Al-Tarazi, 2000*).

Most of the seismicity in this area is of earthquake swarm and is related to subsurface volcanic activities. Fig. 5 shows the locations of instrumental earthquakes in and around the Arabian Peninsula up to 2015 for earthquakes with magnitude above Mw = 3.5. Most of earthquake epicenters are concentrated along the plate boundary, in addition to scattered seismic activity within the Arabian Shield.

It is found that 88 earthquakes occurred in the study area during the period 627–1955. These include only two M = 7, three 6.8, and two 6.6 earthquakes, the remaining are of M ≤ 6.4. Most of these have occurred in the form of sequences and swarms and many are volcanic related (*El-Isa, 2015*). Since April 14, 2009, and more than three months in sequence, an earthquake swarm has occurred in Lunayyir in Saudi Arabia sheild, along ∼50 kilometers of the Red Sea coast.

Most investigators have pointed out that the seismicity of the northern Red Sea is lower than that of the southern part (e.g., *Pedone et al., 1992; Al-Amri, 1995a,b; Daggett et al., 1986*); others, however, have referred to an apparent lower seismicity in the northern part, e.g., *El-Isa and Al-Shanti (1989)*.

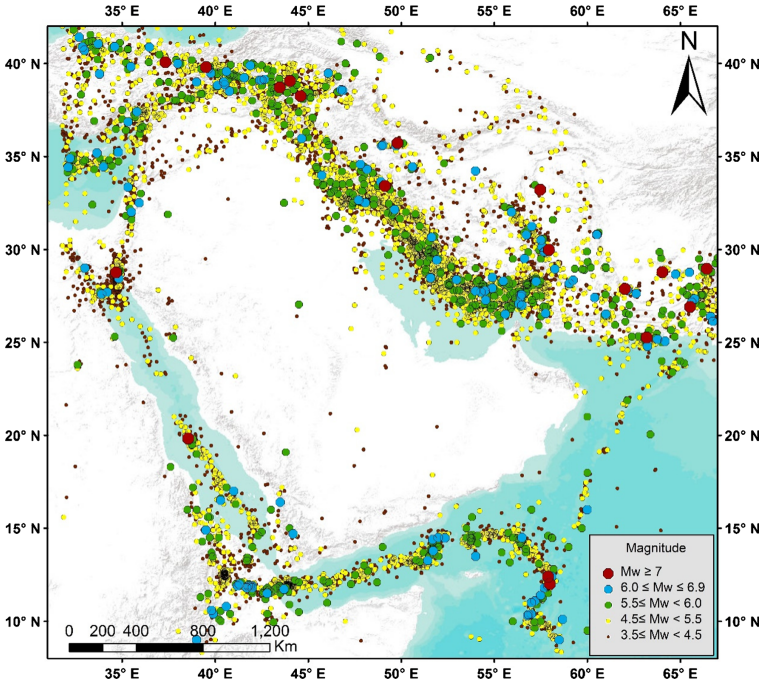


Fig. 5. Instrumental recorded earthquakes of the Arabian Plate from 1900 to 2015 (*Deif et al., 2017*).

## 6. Research Method

In this study, IRSC, ISC, USGS / NEIC and CMT data were used to prepare earthquake catalogues. The data period used is 1900 to 2019. Variables investigated in this study include time, location, frequency, focal mechanism, and depth of earthquakes. The software used is Matlab, GMT and Isola. Figs. 6–7 show the seismicity map of the two study areas.

### 6.1. Depth of earthquakes in two areas of Zagros and Red Sea

The decrease of the compressive force in Zagros shortens this zone along the northeast-southwest. This shortening at the surface shows the folding of the sediments and the upper part of the crystalline crust displays reversed faults. According to *Engdahl et al. (2006)* and *Maggi et al. (2000)*, the focal depth of most of the earthquakes in the Zagros region occurred at a depth

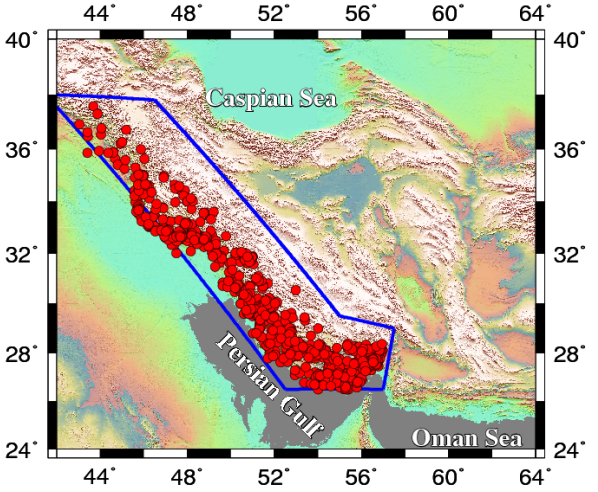


Fig. 6. Seismicity map for earthquakes with a magnitude greater than 5 in the Zagros region (1900 to 2019).

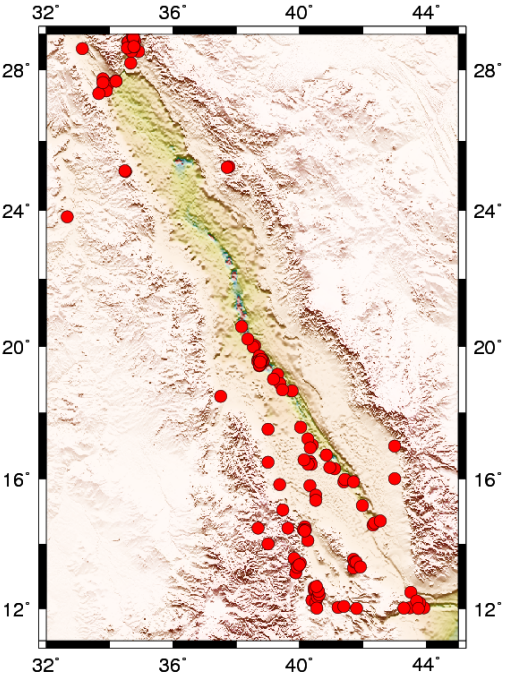


Fig. 7. Seismicity map for earthquakes with a magnitude greater than 5 in the Red Sea region (1900 to 2019).

range of about 10–15 km. In their review of waveform-modelled depths in the Zagros, *Talebian and Jackson (2004)* found no earthquakes deeper than 20 km anywhere except near the Oman Line in the extreme SE Zagros. The mean depth of events indicates the accumulation of earthquakes in the upper part of the basement under sedimentary cover. Earthquake depth distribution in the Zagros region based on *Engdahl et al. (2006)* is shown in Fig. 8.

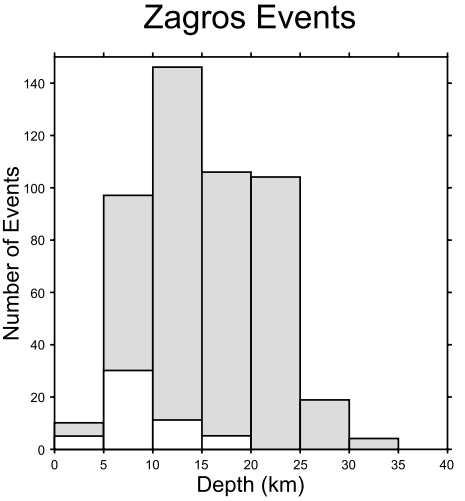


Fig. 8. Earthquake depth distribution in the Zagros region (depths determined by waveform modelling are not shaded) (*Engdahl et al., 2006*).

In this study, the frequency of the Zagros earthquakes is much higher (approximately 5.5 times) that of the Red Sea. The maximum depth of earthquakes in Zagros is greater than the Red Sea, indicating that the Zagros Crust is thicker than the Red Sea, which may be due to different tectonic features. Depth of diagrams of the Zagros and the Red Sea earthquakes in this study are shown in Figs. 9–10.

### 6.2. Removing dependent events from the used ISC Catalogue

In order to assess the seismicity parameters, we eliminated the dependent events (i.e. the aftershocks), which are associated with large fluctuations of seismic activity in space and time. For this purpose the catalogues were declustered using *Gardner and Knopoff (1974)*'s method.

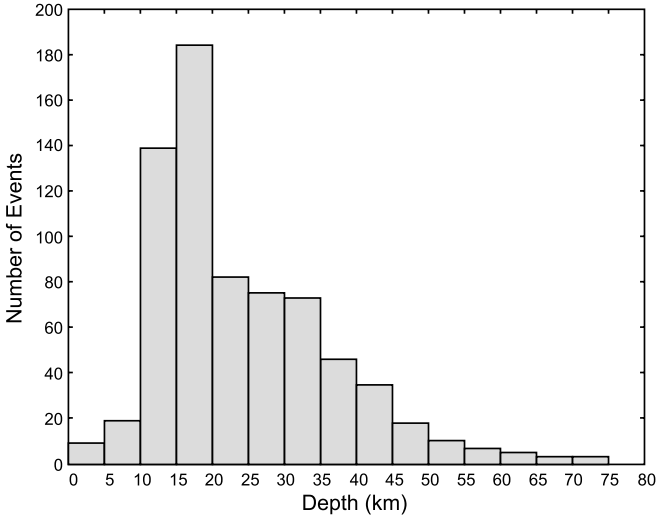


Fig. 9. Depth diagram of the Zagros earthquakes (from 1900 to 2019).

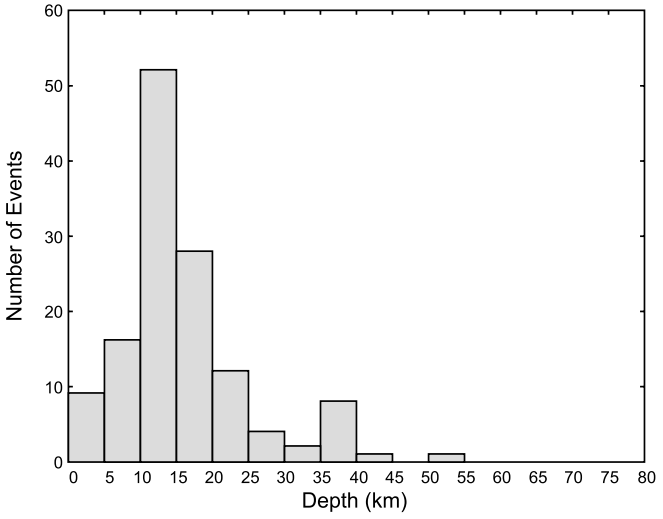


Fig. 10. Depth diagram of the Red Sea earthquakes from (from 1900 to 2019).

In this method, the intervals between events in time and space are used as the criteria for filtering data, which is defined by the magnitude of the main earthquake. In other words, in order to remove dependent events in a series of earthquakes (including main shock and dependent earthquakes

the nearest earthquakes (in terms of time intervals and position) that are commensurate with the magnitudes of the major earthquakes are known as dependent data and are filtered. In the present study, foreshocks and aftershocks were removed from the catalogue using ZMAP software (*Wiemer, 2001*). The number of earthquakes in the initial catalogue was 842 earthquakes with Mw $\geq 5$, which decreased to 454 after the declustering process (i.e. $\sim 46\%$ of events were filtered from the raw catalogue). In this study, the regional dataset of the International Seismological Centre (ISC) is applied. This catalogue is available at `http://www.isc.ac.uk/`. Time window and location of removed aftershocks and foreshocks using ZMAP software according to *Gardner and Knopoff (1974)*'s method is shown in Fig. 11.

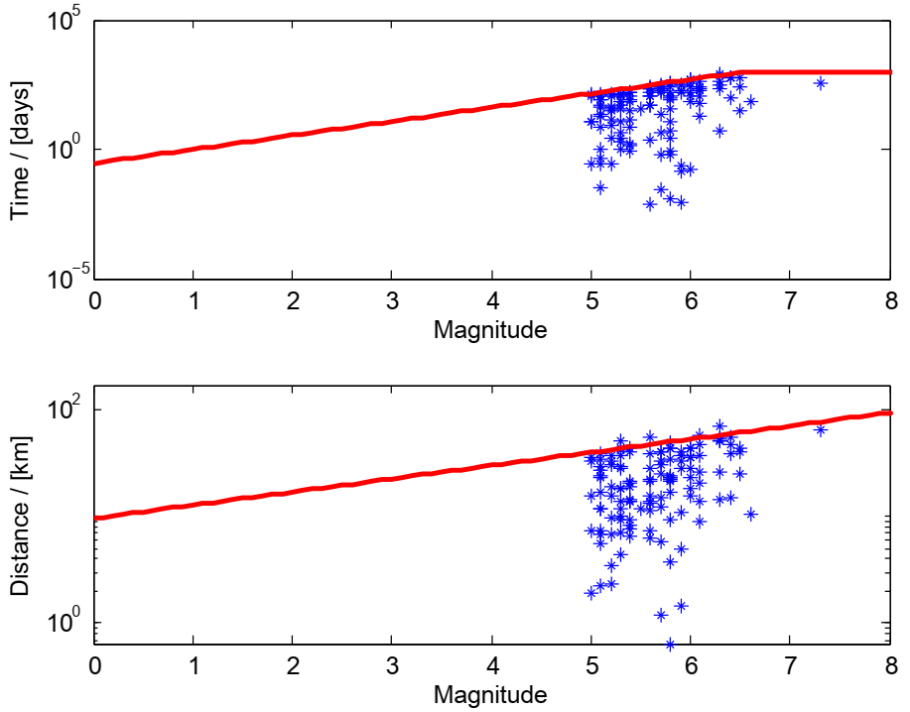


Fig. 11. Time window (top) and location (bottom) of removed aftershocks and foreshocks using ZMAP software. Aftershocks identification windows in time and space domains (red lines in upper and lower panels, respectively) according to *Gardner and Knopoff (1974)*'s method, as implemented in ZMAP 6.0. Stars show the data within 126 revealed clusters of earthquakes.

### 6.3. Estimation of seismicity parameters of Zagros and Read Sea

The Gutenberg-Richter relation (*Gutenberg and Richter, 1944*) is one of the well known empirical relations in seismology. It presents the frequency of occurrence of earthquakes as a function of magnitude (Eq. 1):

$$\log_{10} N = a - bM\,, \tag{1}$$

where $N$ is the cumulative number of earthquakes with magnitude greater than $M$, $a$-value and $b$-value are constants to be determined. The $a$-value is related to the seismic activity and $b$ value is the slope of frequency-magnitude distribution and reveals the ratio of number of smaller to larger earthquakes (*Gutenberg and Richter, 1954; Ashtari Jafari, 2008*).

In order to estimate the seismicity parameters of the two studied areas, the maximum likelihood method (*Aki, 1965*) was used, as implemented in software package ZMAP 6.0 (*Wiemer, 2001*).

#### 6.3.1. Seismicity coefficients for the studied regions

The values obtained for $a$ and $b$ parameters are presented in Table 1. Figs. 12–13 show the results for the Zagros and the Red Sea seismicity, respectively. The results indicate that the $b$-value for the two regions is approximately the same. As the ratio of small to large earthquakes is almost the same, however, the total number of earthquakes in Zagros is much higher and a value also confirms this claim.

Table 1. The values of Gutenberg-Richter parameters for Zagros and Red Sea regions.

| Region | a | b | Mc |
|---|---|---|---|
| **Zagros** | 8.49 | $1.19 \pm 0.06$ | 5.0 |
| **Red Sea** | 7.27 | $1.11 \pm 0.2$ | 5.2 |

### 6.4. Earthquakes focal mechanism estimation for the two studied regions

Examination of the focal mechanism obtained from the CMT references indicates that most of the earthquakes in the Zagros zone are of the reverse type and for the Red Sea are of the normal type, which Figs. 14–15 illustrate this well. In these figures, three different colors of yellow (up to 20km),

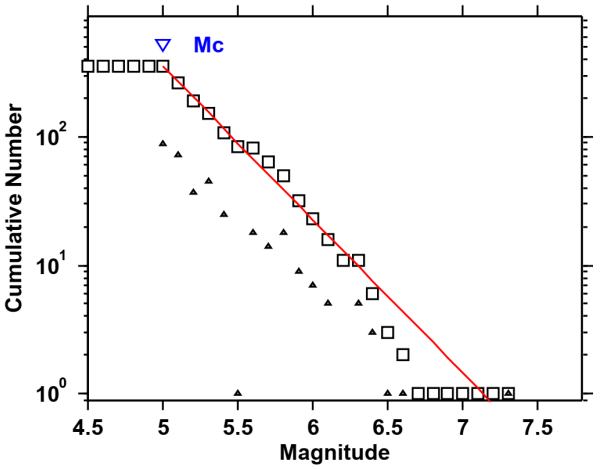


Fig. 12. Magnitude-frequency (Gutenberg-Richter) distribution for instrumental earthquakes in the Zagros region.

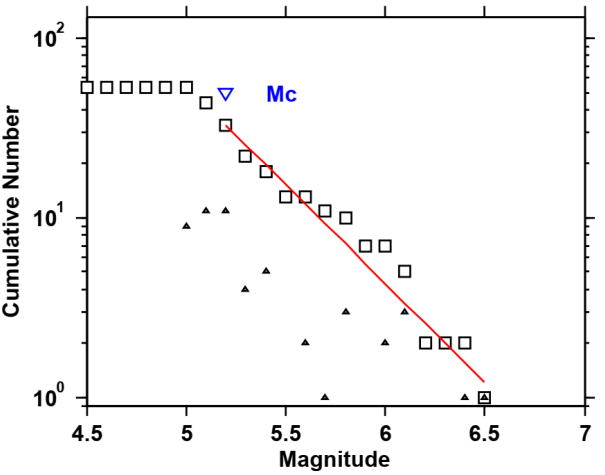


Fig. 13. Magnitude-frequency (Gutenberg-Richter) distribution for instrumental earthquakes in the Red Sea region.

blue (up to 40 km), and red (greater than 40 km) are used to separate the focal depths of the earthquakes, respectively. The Zagros and Red Sea earthquakes occur to depths of about 20 km (marked in yellow). In the Zagros region, there are more red and blue focal mechanism ones. As mentioned

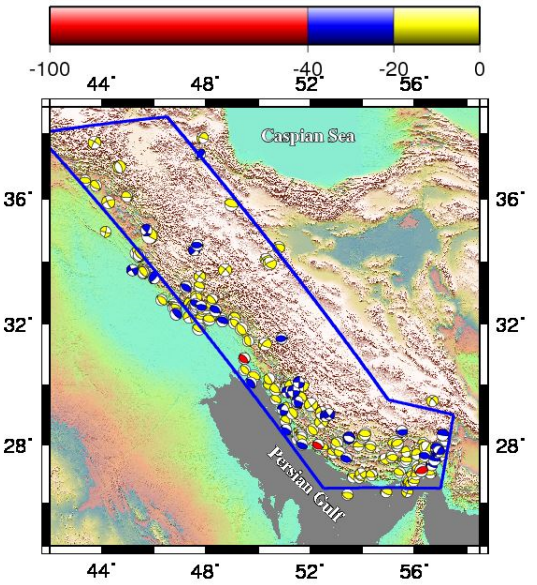


Fig. 14. Focal mechanism of earthquakes larger than magnitude 5 in the Zagros region (ranging from 1900 to 2019).

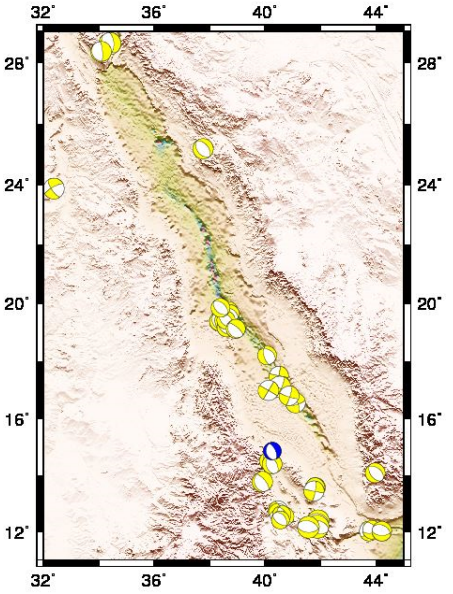


Fig. 15. Focal mechanism of earthquakes larger than magnitude 5 in the Zagros region (ranging from 1900 to 2019).

earlier, the depth of the earthquakes in the Zagros area is greater than that of the Red sea region. That is, earthquakes occur with high frequency but with relatively low magnitudes.

Waveform modelling using Isola software by *Zahradnik et al. (2005)* has been extended to local and regional intervals using full-function Green's function calculation with discrete wave number method (*Bouchon, 1981*). For a number of earthquakes whose focal mechanism was not present in the above catalogue, the focal mechanisms of these earthquakes have been obtained by modelling waveforms using Isola software (*Zahradnik et al., 2005*) and shown in Table 2.

Table 2. Focal mechanism of five earthquakes larger than 5 obtained with Isola software.

| YY/MM/DD | H/M/S | LAT | LON | $M_L$ | D | S1 | D1 | R1 | S2 | D2 | R2 | M0 | P | | T | | |
|---|---|---|---|---|---|---|---|---|---|---|---|---|---|---|---|---|---|
| | | | | | | | | | | | | | Azimuth (deg) | Plunge (deg) | Azimuth (deg) | Plunge (deg) | |
| 08/09/26 | 15/52/24 | 27.62 | 56.43 | 5.1 | 31 | 51 | 75 | 168 | 143 | 79 | 14 | 1.846E+16 | 277 | 3 | 7 | 19 |  |
| 09/10/04 | 21/50/49 | 31.82 | 49.5 | 5.1 | 15 | 131 | 80 | 78 | 0 | 14 | 138 | 3.916E+16 | 230 | 35 | 27 | 54 |  |
| 10/01/16 | 20/23/38 | 32.55 | 48.40 | 5 | 18 | 112 | 47 | 92 | 289 | 42 | 87 | 1.987E+16 | 201 | 3 | 56 | 88 |  |
| 10/05/14 | 18/49/56 | 29.41 | 51.46 | 5.3 | 15 | 20 | 29 | 158 | 129 | 79 | 62 | 1.813E+16 | 241 | 30 | 10 | 49 |  |
| 13/05/23 | 22/44/56 | 27.22 | 53.58 | 5.1 | 18 | 322 | 35 | −70 | 119 | 56 | −103 | 1.769E+16 | 351 | 75 | 218 | 11 |  |

YY/MM/DD: Year/Month/Day, H/M/S: Hour,Minute,Second, LAT(° E): Latitude, LON (° N): Longitude, $M_L$: Local Magnitude, D (km): Depth, S1 (deg): Strike1, D1 (deg): Deep1, R1 (deg): Rake1, S2 (deg): Strike2, D2 (deg): Deep2, R2 (deg): Rake2, M0 (N.m): seismic moment, P: Pression axis, T: Tension axis

## 7. Conclusions

The Red Sea and Zagros are both seismically active areas of the world. The Red Sea earthquakes are a type of sea-floor spreading and its earthquakes occur at depths corresponded to an oceanic crust, while the Zagros earthquakes are caused by the collision of two continental crusts. The present study compares seismicity and tectonic features of these areas by analyzing seismicity data. The Gutenberg Richter relationship shows that the $a$-value in the Zagros is 8.49 and in the Red Sea is 7.27, that is the Zagros seis-

micity rate is about 5.5 times higher than the Red Sea. However, their $b$-value does not differ much from each other and it means that there is no difference in the ratio of large to small earthquakes in these two areas. On the one hand, there is a relative difference between the focal depths of the events in these two regions; the highest frequency of the Zagros earthquakes is approximately 15–20 km in depth and is approximately 10–15 km for the Red Sea. The mechanism of the Zagros earthquakes is due to the pressure of the Arabian plate moving northeastward, in the form of reverse faulting or thrust fault with high dip. It is seen along the faults of the region. Most of the Zagros faults are oriented perpendicular to the compression direction (convergence) of the Arabian plate. Unlike the Zagros, the main mechanism of earthquakes in the northern part of the Red Sea is normal and its southern part includes strike-slip component. Geodynamic studies also show that convergence rates are high in the Zagros region and it seems that due to this high velocity there is no opportunity for stress accumulation and large earthquakes in this area. That is, earthquakes occur with high frequency but with relatively low magnitudes.

## References

Aki K., 1965: Maximum likelihood estimate of $b$ in the formula $\log N = a - bM$ and its confidence limits. Bull. Earthq Res. Inst. Univ. Tokyo, **43**, 237–239.

Al-Amri A. M., 1995a: Preliminary seismic hazard assessment of southern Red Sea region. Eur. Earthq. Eng., 3, 33–38.

Al-Amri A. M., 1995b: Recent seismic activity in the northern Red Sea. J. Geodyn., **20**, 3, 243–253, doi: 10.1016/0264-3707(95)00007-V.

Alavi M., 1994: Tectonics of the Zagros orogenic belt of Iran: new data and interpretations. Tectonophysics, **229**, 3-4, 211–238, doi: 10.1016/0040-1951(94)90030-2.

Alavi M., 2004: Regional stratigraphy of the Zagros fold-thrust belt of Iran and its proforeland evolution. Am. J. Sci., **304**, 1, 1–20, doi: 10.2475/ajs.304.1.1.

Alavi M., 2007: Structures of the Zagros fold-thrust belt in Iran. Am. J. Sci., **307**, 9, 1064–1095, doi: 10.2475/09.2007.02.

Allahyari K., Saccani E., Pourmoafi M., Beccaluva L., Masoudi F., 2010: Petrology of mantle peridotites and intrusive mafic rocks from the Kermanshah ophiolitic complex (Zagros belt, Iran):implications for the geodynamic evolution of the neo-Tethyan oceanic branch between Arabia and Iran. Ofioliti, **35**, 2, 71–90.

Al-Tarazi E., 2000: The Major Gulf of the Aqaba Earthquake, 22 November 1995 – Maximum Intensity Distribution. Nat. Hazards, **22**, 1, 17–27, doi: 10.1023/A:1008109810031.

ArRajehi A., McClusky S., Reilinger R., Daoud M., Alchalbi A., Ergintav S., Gomez F., Sholan J., Bou-Rabee F., Ogubazghi G., Haileab B., Fisseha S., Asfaw L., Mahmoud S., Rayan A., Bendik R., Kogan L., 2010: Geodetic constraints on present-day motion of the Arabian Plate: Implications for Red Sea and Gulf of Aden rifting. Tectonics, **29**, 3, TC3011, doi: 10.1029/2009TC002482.

Ashtari Jafari M., 2008: The distribution of b-value in different seismic provinces of Iran. The 14th World Conference on Earthquake Engineering, Beijing, China, doi: 10.13140/RG.2.1.4514.3523.

Berberian M., 1995: Master "blind" thrust faults hidden under the Zagros folds: active basement tectonics and surface morphotectonics. Tectonophysics, **241**, 3-4, 193–224, doi: 10.1016/0040-1951(94)00185-C.

Besse J., Torcq F., Gallet Y., Ricou L. E., Krystyn L., Saidi A., 1998: Late Permian to late Triassic paleomagnetic data from Iran: constraints on the migration of the Iranian block through the Tethyn ocean and initial destruction of Pangaea. Geophys. J. Int., **135**, 1, 77–92, doi: 10.1046/j.1365-246X.1998.00603.x.

Bosworth W., Huchon P., McClay K., 2005: The Red Sea and Gulf of Aden basins. J. Afr. Earth Sci., **43**, 1, 334–378, doi: 10.1016/j.jafrearsci.2005.07.020.

Bouchon M., 1981: A simple method to calculate Green's functions for elastic layered media. Bull. Seismol. Soc. Am., **71**, 4, 959–971.

Brew G. E., 2001: Tectonic evolution of Syria interpreted from integrated geophysical and geological analysis. PhD thesis, Cornell Univ., USA.

Brew G., Barazangi M., Al-Maleh A., Sawaf T., 2001: Tectonic and geologic evolution of Syria. GeoArabia **6**, 4, 573–616.

Camp V. E., Roobol M. J., 1992: Upwelling asthenosphere beneath western Arabia and its regional implications. J. Geophys. Res., **97**, B11, 15255–15271, doi: 10.1029/92JB00943.

Cochran J. R., Martinez F., 1988: Evidence from the northern Red Sea on the transition from continental to oceanic rifting. Tectonophysics, **153**, 1-4, 25–53, doi: 10.1016/0040-1951(88)90006-6.

Cochran J., Gaulier J. M., LePichon X., 1991: Crustal structure and the mechanism of extension in the Northern Red Sea: constraints from gravity anomalies. Tectonics, **10**, 5, 1018–1037, doi: 10.1029/91TC00926.

Daggett P., Morgan P., Boulos F., Hennin S., El-Sherif A., El-Sayed A., Basta N., Melek Y., 1986: Seismicity and active tectonics of the Egyptian Red Sea margin and the northern Red Sea. Tectonophysics, **125**, 4, 313–324, doi: 10.1016/0040-1951(86)90168-X.

Dehghani G. A., Makris J., 1984: The gravity field and crustal structure of Iran. Neues Jahrb. Geol. Paläontol. Abh., **168**, 2-3, 215–229, doi: 10.1127/njgpa/168/1984/215.

Deif A., Al-Shijbi Y., El-Hussain I., Ezzelarab M., Mohamed A. M. E., 2017: Compiling an earthquake catalogue for the Arabian Plate, Western Asia. Journal of Asian Earth Sciences, **147**, 1, 345–357, doi: 10.1016/j.jseaes.2017.07.033.

DeMets C., Gordon R. G., Argus D. F., Stein S., 1994: Effect of recent revisions to the geomagnetic reversal time scale on estimates of current plate motions. Geophys. Res. Lett., **21**, 20, 2191–2194, doi: 10.1029/94GL02118.

Drake C. L., Girdler R. W., 1964: A geophysical study of the Red Sea. Geophys. J. Roy. Astron. Soc., **8**, 5, 473–495, doi: 10.1111/j.1365-246X.1964.tb06303.x.

El-Hussain I., Al-Shijbi Y., Deif A., Mohamed A. M. E., Ezzelarab M., 2018: Developing a seismic source model for the Arabian Plate. Arab. J. Geosci., **11**, 15, 435, doi: 10.1007/s12517-018-3797-7.

El-Isa Z. H., Al Shanti A., 1989: Seismicity and tectonics of the Red Sea and western Arabia. Geophys. J. Int., **97**, 3, 449–457, doi: 10.1111/j.1365-246X.1989.tb00515.x.

El-Isa Z. H., 2015: Seismicity and seismotectonics of the Red Sea Region, Arab. J. Geosci., **8**, 10, 8505–8525, doi: 10.1007/s12517-015-1819-2.

Engdahl E. R., Jackson J. A., Myers A. C., Bergman E. A., Priestley K., 2006: Relocation and assessment of seismicity in the Iran region. Geophys. J. Int., **167**, 2, 761–778, doi: 10.1111/j.1365-246X.2006.03127.x.

Fairhead J. D., Girdler R. W., 1970: The seismicity of the Red Sea, Gulf of Aden and Afar triangle. Philos. Trans. Royal Soc. London, Ser. A, **267**, 1181, 49–74.

Fairhead J. D., Girdler R. W., 1972: The seismicity of East African rift system. Tectonophysics, **15**, 1-2, 115–122, doi: 10.1016/0040-1951(72)90056-X.

Falcon N. L., 1969: Problems of the relationship between surface structure and deep displacements illustrated by Zagros range. In: Kent P. E., Satterthwaite G. E., Spencer A. M. (Eds.): Time and Place in Orogeny. Geol. Soc., London, Spec. Publ., **3**, 9–22, doi: 10.1144/GSL.SP.1969.003.01.02.

Gardner J. K., Knopoff L., 1974: Is the sequence of earthquakes in Southern California, with aftershocks removed, Poissonian? Bull. Seism. Soc. Am., **64**, 5, 1363–1367.

Garfunkel Z., 1981: Internal structure of the Dead Sea leaky transform (rift) in relation to plate kinematics. Tectonophysics, **80**, 1-4, 81–108, doi: 10.1016/0040-1951(81)90143-8.

Ghasemi A., Talbot C. J., 2006: A new tectonic scenario for the Sanandaj-Sirjan Zone (Iran). J. Asian Earth Sci., **26**, 6, 683–693, doi: 10.1016/j.jseaes.2005.01.003.

Giese P., Makris J., Akashe B., Röwer P., Letz H., Mostaanpour M., 1984: The crustal structure in Southern Iran derived from seismic explosion data. Neues Jahrb. Geol. Paläontol. Abh., **168**, 2-3, 230–243, doi: 10.1127/njgpa/168/1984/230.

Gomez F., Karam G., Khawlie M., McClusky S., Vernant P., Reilinger R., Jaafar R., Tabet C., Khair K., Barazangi M., 2007: Global Positioning System measurements of strain accumulation and slip transfer through the restraining bend along the Dead Sea fault system in Lebanon. Geophys. J. Int., **168**, 3, 1021–1028, doi: 10.1111/j.1365-246X.2006.03328.x.

Guennoc P., Pautot G., Leqentrec M. F., Coutelle A., 1990: Structure of an early oceanic rift in the northern Red-Sea. Oceanol. Acta, **13**, 2, 145–157.

Güllen L., Pinar A., Kalafat D., Özel N., Horasan G., Yilmazer M., Işikara A., 2002: Surface fault breaks, aftershock distribution, and rupture process of the 17 August 1999, Izmit earthquakes. Bull. Seismol. Soc. Am., **92**, 1, 230–244, doi: 10.1785/0120000815.

Gutenberg B., Richter C. F., 1944: Frequency of earthquakes in California. Bull. Seismol. Soc. Am., **34**, 4, 185–188.

Gutenberg B., Richter C. F., 1954: Seismicity of the Earth and Associated Phenomena. Princeton University Press, Princeton, N.J., USA.

Hessami K., Jamali F., Tabassi H., 2003: Major active faults in Iran. Ministry of Science, research and technology, International Institute of Earthquake Engineering and Seismology (IIEES), Tehran, Iran, 1:2,500,000 scale map.

Hatzfeld D., Tatar M., Priestley K., Ghafory-Ashtiany M., 2003: Seismological constraints on the crustal structure beneath the Zagros Mountain belt (Iran). Geophys. J. Int., **155**, 2, 403–410, doi: 10.1046/j.1365-246X.2003.02045.x.

Head S. M., 1987: Red Sea fisheries – Chapter 17. In: Edwards A. J., Head S. M. (Eds.): Red Sea, Key Environment Series. Pergamon Press, Oxford, 363–382, doi: 10.1016/B978-0-08-028873-4.50022-0.

Horton B. K., Hassanzadeh J., Stockli D. F., Axen G. J., Gillis R. J., Guest B., Amini A., Fakhari M. D., Zamanzadeh S. M., Grove M., 2008: Detrital zircon provenance of Neoproterozoic to Cenozoic deposits in Iran: implications for chronostratigraphy and collisional tectonics. Tectonophysics, **451**, 1-4, 97–122, doi: 10.1016/j.tecto.2007.11.063.

Jackson J. A., Fitch T. J., 1981: Basement faulting and the focal depth of the larger earthquakes in the Zagros mountains (Iran). Geophys. J. Roy. Astron. Soc., **64**, 3, 561–586, doi: 10.1111/j.1365-246X.1981.tb02685.x.

Jackson J. A., McKenzie D. P., 1984: Active tectonics of the Alpine-Himalayan belt between Western Turkey and Pakistan. Geophys. J. Roy. Astron. Soc., **77**, 1, 185–264, doi: 10.1111/j.1365-246X.1984.tb01931.x.

Jackson J. A., McKenzie D. P., 1988: The relationship between plate motions and seismic moment tensors, and the rates of active deformation in the Mediteranian and the Middle East. Geophys. J. Roy. Astron. Soc., **93**, 1, 45–73, doi: 10.1111/j.1365-246X.1988.tb01387.x.

James G. A., Wynd J. G., 1965: Stratigraphic Nomenclature of Iranian Oil Consortium Agreement Area. AAPG Bull., **49**, 12, 2182–2245.

Johnson P. R., 1998: Tectonic map of Saudi Arabia and adjacent areas. Deputy Ministry for Mineral Resources, USGS TR-98-3, Saudi Arabia.

Khadivi Sh., 2010: Tectonic evolution and growth of the Zagros Mountain Belt (Fars, Iran): constraints from magnetostratigraphy, sedimentology and low-temperature thermochronometry. Earth Sciences. PhD thesis, Université Pierre et Marie Curie – Paris VI.

Madahizadeh R., Mostafazadeh M., Ashkpour-Motlagh Sh., 2016: Earthquake Potential in the Zagros region (Iran). Acta Geophys., De Gruyter, **64**, 5, 1462–1494, doi: 10.1515/acgeo-2016-0080.

Maggi A., Jackson J. A., Priestley K., Baker C., 2000: A re-assessment of focal depth distributions in southern Iran, the Tien Shan and northern India: do earthquakes really occur in the continental mantle? Geophys. J. Int., **143**, 3, 629–661, doi: 10.1046/j.1365--246x.2000.00254.x.

Makris J., Rihm R., 1991: Shear-controlled evolution of the Red Sea: pull apart model. Tectonophysics, **198**, 2-4, 441–466, doi: 10.1016/0040-1951(91)90166-P.

McQuarrie N., Stock J. M., Verdel C., Wernicke B. P., 2003: Cenozoic evolution of the Neotethys and implications for the causes of plate motions, Geophys. Res. Lett., **30**, 2036, doi: 10.1029/2003GL017992.

Mirzaei N., 1997: Seismic zoning of Iran. Dissertation, Institute of Geophysics. State Seismological Bureau, Beijng, People's Republic of China, 134 p.

Mirzaei N., Gao M., Chen Y. T., 1998: Seismic source regionalization for seismic zoning of Iran: major seismotectonic provinces. J. Earthq. Pred. Res., **7**, 4, 465–495.

Morcos S. A., 1970: Physical and chemical oceanography of the Red Sea. Oceanogr. Mar. Biol. Ann. Rev., **8**, 73–202.

Mostafazadeh M., Alptekin O., Oncel A. O., 2000: Body waveform modeling of five moderately earthquakes in the Zagros fold thrust belt. JSEE (J. Seis. Earthq. Eng.). **2**, 3, 1–10.

Nemati M., 2015: Aftershocks investigation of 2010 Dec. and 2011 Jan. Rigan earthquakes in the southern Kerman province, SE Iran. J. Tethys (Iran), **3**, 2, 96–113.

Nowroozi A. A., 1971: Seismo-tectonics of the Persian plateau, eastern Turkey, Caucasus and Hindu-Kush regions. Bull. Seismol. Soc. Am., **61**, 2, 317–341.

Palano M., Imprescia P., Agnon A., Gresta S., 2018: An improved evaluation of the seismic/geodetic deformation-rate ratio for the Zagros Fold-and-Thrust collisional belt. Geophys. J. Int., **213**, 1, 194–209, doi: 10.1093/gji/ggx524.

Paul A., Kaviani A., Hatzfeld D., Vergne J., Mokhtari M., 2006: Seismological evidence for crustal scale thrusting in the Zagros mountain belt (Iran). Geophys. J. Int., **166**, 1, 227–237, doi: 10.1111/j.1365-246X.2006.02920.x.

Paul A., Hatzfeld D., Kaviani A., Tatar M., Péquegnat C., 2010: Seismic imaging of the lithospheric structure of the Zagros mountain belt (Iran). Geol. Soc., London, Spec. Pub., **330**, 5–18, doi: 10.1144/SP330.2.

Pedone R., Lombardo P., Diamntidis D., 1992: Seismotectonic regionalization of the Red Sea Area and its application to seismic risk analysis. Nat. Hazards, **5**, 3, 233–247, doi: 10.1007/BF00125229.

Rasul N. M. A., Stewart I. C. F., 2015: The Red Sea – The Formation, Morphology, Oceanography and Environment of a Young Ocean Basin. Springer Earth System Sciences.

Reilinger R., McClusky S., ArRajehi A., 2015: Geodetic constraints on the geodynamic evolution of the Red Sea. In: Rasul N. M. A., Stewart I. C. F. (Eds.): The Red Sea – The Formation, Morphology, Oceanography and Environment of a Young Ocean Basin. pp. 135–149, Springer Earth System Sciences, Springer, Berlin, Heidelberg, doi: 10.1007/978-3-662-45201-1_7.

Roeser H. A., 1975: A detailed magnetic survey of the southern Red Sea. Geol. Jahrb., **D13**, 131–153.

Saccani E., Allahyari K., Beccaluva L., Bianchini G., 2013: Geochemistry and petrology of the Kermanshah ophiolites (Iran): Implication for the interaction between passive rifting, oceanic accretion, and OIB-type components in the Southern Neo-Tethys Ocean. Gondwana Res., **24**, 1, 392–411, doi: 10.1016/j.gr.2012.10.009.

Sella G. F., Dixon T. H., Mao A., 2002: REVEL: A model for recent plate velocities from space geodesy. J. Geophys. Res., **107**, B4, 2081, doi: 10.1029/2000JB000033.

Smith G., McNeill L., Henstock I. J., Bull J., 2012: The structure and fault activity of the Makran accretionary prism. J. Geophys. Res., Solid Earth, **117**, B07407, doi: 10.1029/2012JB009312.

Snyder D. B., Barazangi M., 1986: Deep crustal structure and flexure of the Arabian Plate beneath the Zagros collisional mountain belt as inferred from gravity observations. Tectonics, **5**, 3, 361–373, doi: 10.1029/TC005i003p00361.

Stern R. J., Johnson P. R., 2010: Continental lithosphere of the Arabian Plate: a geologic, petrologic, and geophysical synthesis. Earth Sci. Rev., **101**, 1-2, 29–67, doi: 10.1016/j.earscirev.2010.01.002.

Stöcklin J., 1974: Possible Ancient Continental Margin in Iran. In: Burk C. A., Drake C. L. (Eds.): The Geology of Continental Margins. Springer, New York, 873–887, doi: 10.1007/978-3-662-01141-6_64.

Sultan M., Becker R., Arvidson R. E., Shore P., Stern R. J., El Alfy Z., Attia R. I., 1993: New constraints on Red Sea rifting from correlations of Arabian and Nubian Neoproterozoic outcrops. Tectonics, **12**, 6, 1303–1319, doi: 10.1029/93TC00819.

Swartz D. H., Arden D. D., 1960: Geologic history of the Red Sea area. AAPG Bull., **44**, 1621–1637.

Talebian M., Jackson J., 2004: A reappraisal of earthquake focal mechanisms and active shortening in the Zagros Mountains of Iran. Geophys. J. Int., **156**, 3, 506–526, doi: 10.1111/j.1365-246X.2004.02092.x.

Tatar M., Hatzfeld D., Martinod J., Walpersdorf A., Ghafori-Ashtiany M., Chéry J., 2002: The present-day deformation of the central Zagros from GPS measurements. Geophys. Res. Lett., **29**, 19, 33-1–33-4, doi: 10.1029/2002GL015427.

Tatar M., Hatzfeld D., Ghafori-Ashtiany M., 2004: Tectonics of the central Zagros (Iran) deduced from microearthquakes seismicity. Geophys. J. Int., **156**, 2, 255–266, doi: 10.1111/j.1365-246X.2003.02145.x.

Vernant Ph., Nilforoushan F., Hatzfeld D., Abbassi M. R., Vigny C., Masson F., Nankali H., Martinod J., Ashtiani A., Bayer R., Tavakoli F., Chéry J., 2004: Present-day crustal deformation and plate kinematics in the Middle East constrained by GPS measurements in Iran and northern Oman. Geophys. J. Int., **157**, 1, 381–398, doi: 10.1111/j.1365-246X.2004.02222.x.

Walpersdorf A., Hatzfeld D., Nankal, H., Tavakol F., Nilforoushan F., Tatar M., Vernant P., Chéry J., Masson F., 2006: Difference in the GPS deformation pattern of North and Central Zagros (Iran). Geophys. J. Int., **167**, 3, 1077–1088, doi: 10.1111/j.1365-246X.2006.03147.x.

Wiemer S., 2001: A software package to analyze seismicity: ZMAP. Seismol. Res. Lett., **72**, 3, 373–382, doi: 10.1785/gssrl.72.3.373.

Yamini-Fard F., Hatzfeld D., Tatar M., Mokhtari M., 2006: Microseismicity at the intersection between the Kazerun fault and the Main Recent Fault (Zagros-Iran). Geophys. J. Int., **166**, 1, 186–196, doi: 10.1111/j.1365-246X.2006.02891.x.

Zahradnik J., Serpetsidaki A., Sokos E., Tselentis G. A., 2005: Iterative deconvolution of regional waveforms and double-event interpretation of the 2003 Lefkada earthquake, Greece. Bull. Seismol. Soc. Am., **95**, 1, 159–172, doi: 10.1785/0120040035.